

Compact microscope system for biomedical applications

Thesis by
Jinho Kim

In Partial Fulfillment of the Requirements for
the degree of
Doctor of Philosophy

The Caltech logo, featuring the word "Caltech" in a bold, orange, sans-serif font, centered within a light orange rectangular background.

CALIFORNIA INSTITUTE OF TECHNOLOGY
Pasadena, California

2017
(Defended May 15, 2017)

© 2017

Jinho Kim
All Rights Reserved

ACKNOWLEDGEMENTS

All of achievements I made at Caltech would not be possible without the help of others I have worked with. First of all, I would like to express sincere appreciation to Professor Changhui Yang about his thoughtful guidance on the research. His advice always led me to consider problems from different perspectives and helped me to find solutions eventually. I also want to thank him for giving me enough chance to design and organize optical systems by myself. I have learned a lot about the system level design during the process, and I actually enjoyed the whole process of engineering work.

I was lucky enough to work with brilliant collaborators from in and outside of Caltech in every project. Professor Ana Rodriguez from New York University taught me about parasitology and biological sample treatment in ePetri project. I had asked her a lot of different types of sample preparation and she was always willing to helping me on my request. Professor Henry A. Lester, Dr. Beverley M. Henley, and Charlene H. Kim helped me to prepare primary mouse ventral midbrain neurons for the EmSight project. I have learned a lot about neuro-biology and *in vitro* cell culture work from them. Dr. Han Xu and Dr. Dana Nojima from Amgen helped me to bring out the idea of high throughput parallel imaging system, and they also gave me lots of practical ideas about the 96Eyes project. I really appreciate all of the inputs from the collaborators.

Caltech Biophotonics lab has provided me the best working environment I can ever imagine. I was really happy to work with smart and friendly lab members at the Biophotonics lab. I would like thank them for their help: Seung Ah Lee, Jaehee Jung, Chao Han, Jiantao Huangfu, Daifa Wang, Roarke Horstmeyer, Xiaoze Ou, Mooseok Jang, Shin Usuki, Donghun Ryu, Hao Deng, Yidong Tan, Edward Zhou, Haowen Ruan, Atsushi Shibukawa, Albert Chung, Josh Brake, Michelle Cua, Helen Lu, and Jian Xu. And I want to express special appreciation to Antony Chan and Daniel Martin who are upgrading the imaging system I have built here in Caltech. And our lab manager, Ms. Anne Sullivan, has been my best supporter during my stay at Caltech. I appreciate all of the assistance she has given to me so far.

Finally, my deep and sincere gratitude to my family for their unparalleled love, help, advice, and support. I am forever indebted to my parents for giving me the opportunities that

have made me who I am. I cannot thank my wife enough for always staying here with me and encouraging me whenever I had hard time. And my beloved daughter, Jiyun, her existence itself gives me more energy in my life. I appreciate all of them again. I am so happy to have a chance to live a life with this wonderful family.

ABSTRACT

Demands for an imaging system which has high space-bandwidth product (SBP) are increasing in modern biomedical research as the amount of information to be dealt with is increasing. However, conventional microscopy has a limited SBP of about 10 mega pixels, and as such if a user wants an image in high resolution, the field of view (FOV) of the image is reduced, or if a wide FOV is necessary, the user needs to give up the resolution of image. A common way of overcoming this SBP limit in the conventional microscopy is to use mechanical moving stages and scan through wide sample area, however, it is time consuming to image large area using a high numerical aperture (NA) objective lens. This thesis presents compact imaging systems based on Fourier ptychographic microscopy for biomedical applications which are able to increase SBP without having any mechanical moving parts: one imaging system for an incubator embedded imaging system to be used in *in-vitro* cell culture monitoring, and the other for a high throughput 96 well plate imaging system for fast drug screening.

TABLE OF CONTENTS

Acknowledgements.....	iii
Abstract	v
Table of Contents.....	vi
List of Illustrations	viii
List of Tables	x
Chapter 1: Introduction to optical microscope systems.....	11
1.1 Principle of optical image formation	11
1.2 Modern microscopy systems.....	14
1.2.1 Kohler illumination	15
1.2.2 Photo detectors	17
1.2.3 Objective lens	19
1.2.3.1 Resolution.....	20
1.2.3.2 Field of View.....	22
1.2.3.3 Depth of Field.....	23
1.3 Aberration.....	23
1.3.1 Chromatic aberration.....	23
1.3.2 Achromatic aberration.....	25
1.3.2.1 Tilt.....	25
1.3.2.2 Defocus.....	25
1.3.2.3 Astigmatism.....	25
1.3.2.4 Coma.....	27
1.3.2.5 Spherical aberration.....	27
1.3.2.6 Strehl ratio	27
1.4 Imaging modes	27
1.4.1 Bright field intensity imaging	27
1.4.2 Zernike phase contrast imaging	29
1.4.3 Differential interference contrast imaging.....	30
1.4.4 Fluorescence imaging.....	31
Chapter 2: Fourier ptychographic microscopy	33
2.1 FPM image acquisition process	33
2.2 FPM image reconstruction process.....	38
2.3 Image space-bandwidth product improvement	42
2.4 Digital image refocusing	43
2.5 Computational aberration correction	44
Chapter 3: EmSight: Incubator embedded cell culture imaging system.....	46
3.1 Introduction	46
3.2 System configuration.....	48
3.3 LED matrix and EmSight positional calibration	51
3.4 System characterization.....	54
3.5 Live cell culture imaging.....	66

3.6 Dual channel fluorescence imaging	67
3.7 Discussion and conclusion	71
Chapter 4: 96Eyes: High throughput 96 well plate imaging system for fast drug screening	73
4.1 Introduction	73
4.2 System configuration.....	76
4.2.1 Imaging sensor board	77
4.2.2 Injection molding polymer objective lens	80
4.2.3 LED matrix operation for FPM illumination.....	81
4.3 System characterization.....	85
4.3.1 Image resolution of 96Eyes.....	86
4.3.2 Digital image refocusing of 96Eyes.....	91
4.3.3 Fluorescence imaging of 96Eyes	94
4.3.4 Comparison between 96Eyes and commercial well plate imaging systems	99
4.4 Discussion and conclusion	99
Bibliography	102

LIST OF ILLUSTRATIONS

<i>Number</i>	<i>Page</i>
1.1 Optical imaging system diagram	12
1.2 Finite corrected and infinity corrected imaging system	13
1.3 Configuration of modern optical microscope.....	15
1.4 Microscope illumination path. Kohler illumination	16
1.5 Microscope imaging path.....	17
1.6 Microscope Objective lens.....	18
1.7 Systems with annular pupil	21
1.8 Chromatic aberration.....	24
1.9 Bright field imaging modes.....	28
1.10 Fluorescence imaging.....	31
2.1 FPM image acquisition process	34
2.2 FPM illumination methods.....	36
2.3 Phase retrieval algorithm.....	38
2.4 FPM image reconstruction process.....	40
2.5 FPM image resolution improvement	42
2.6 FPM digital image refocusing.....	43
3.1 System configuration and imaging method of the EmSight	49
3.2 LED position calibration	52
3.3 Effect of LED position misalignment.....	53
3.4 Raw image resolution of EmSight	54
3.5 FPM reconstructed image resolution of EmSight	55
3.6 Multi-modal imaging of EmSight.....	56
3.7 Digital refocusing of the EmSight	57
3.8 Digital image refocusing example	60
3.9 Large FOV imaging of the EmSight.....	61
3.10 Time-lapse imaging of the mouse midbrain culture.....	63

3.11 6-well plate imaging of the mouse ventral midbrain culture	64
3.12 Time-lapse imaging of the dividing cells	67
3.13 EmSight with dual channel fluorescence imaging	68
3.14 FPM imaging of dual channel fluorescence EmSight.....	69
3.15 Dual channel fluorescence imaging of dual channel fluorescence EmSight	70
4.1 96Eyes system configuration	74
4.2 Imaging sensor board operation.....	75
4.3 Cooling of imaging sensor system.....	78
4.4 Injection molding polymer objective lens	79
4.5 CODE V ray tracing simulation result.....	81
4.6 LED matrix operation for FPM illumination.....	82
4.7 FPM image acquisition process	83
4.8 FPM resolution test of 96Eyes	84
4.9 FPM intensity imaging test of 96Eyes.....	85
4.10 FPM phase imaging test of 96Eyes	87
4.11 96 well plate bottom height distribution.....	88
4.12 Digital refocusing of 96Eyes.....	89
4.13 Digital refocusing of HeLa sample in 96 well plate.....	93
4.14 96Eyes fluorescence imaging	94
4.15 96Eyes fluorescence imaging test using 2 μ m fluorescence beads ...	95
4.16 96Eyes fluorescence imaging test using GFP HeLa cell lines.....	96
4.17 Bright field image comparison between 96Eyes and Operetta.....	97
4.18 Fluorescence image comparison between 96Eyes and Operetta	98

LIST OF TABLES

<i>Number</i>	<i>Page</i>
1.1 Microscope tube length and objective thread size Mercury	19
1.2 PSF and resolution of systems with rectangular and hexagonal pupil	22
1.3 Zernike aberrations.....	26
1.4 Wavelength for maximum absorption and emission.....	32
4.1 Dispersion of the materials used in the objective lens	80
4.2 Fluorescence imaging throughput comparison.....	101
4.3 Phase imaging throughput comparison.....	101

INTRODUCTION TO OPTICAL MICROSCOPE SYSTEMS

An optical microscope is a fundamental instrument for inspection and examination of minuscule samples in biological and medical research. The main reason that the optical microscope has gained such popularity in a wide range of applications is that it is able to convert small, closely located samples, which are not discernable to our naked eyes, into clearly separated entities in large detectable sizes without ambiguity. Since its first invention in the 17th century, there have been several different approaches for better magnification and resolving power. However, their working principles share a common background in the sense that they are utilizing light as a medium for sample information transfer.

As an introduction to this thesis, we will explain the basic working principle of the modern optical microscope in this chapter. The ray properties of light in image formation and the configuration of modern microscopes are briefly described. Following this, several different modes of optical microscopy are introduced at the end of the chapter.

1.1 Principle of optical image formation

An optical imaging system uses light as a probe for detecting target samples in interest. Among many reasons, the most fundamental motive for why people have tried to use light for inspection systems is that we gather most of our detailed information through visible image data. Figure 1.1 shows a block diagram of a general optical imaging system. Known or unknown light (L) is illuminated onto a sample (S) of interest. The illumination light interacts with the sample and results in a new, modified light, which enters the imaging system for further modification. The imaging system uses the information from the input light in order to generate a useful image (I) as required. The main problem is that no optical imaging system can generate exactly the same image information as the sample due to the wave nature of light and noise in the system. As a result, an imaging system generates an

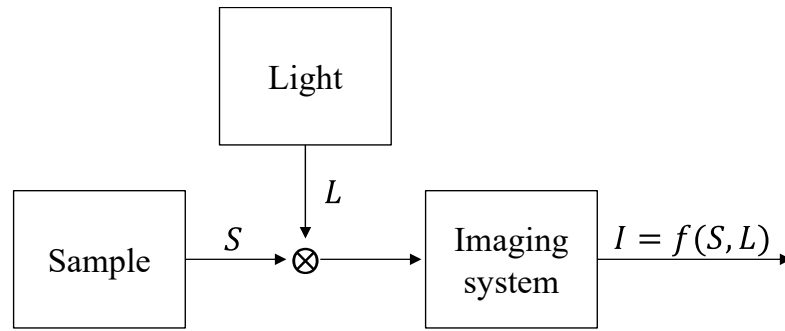


Figure 1.1: Optical imaging system diagram

approximate image of the sample information, and a user gauges the actual sample information based on the measured image information and the specifications of the imaging system in use.

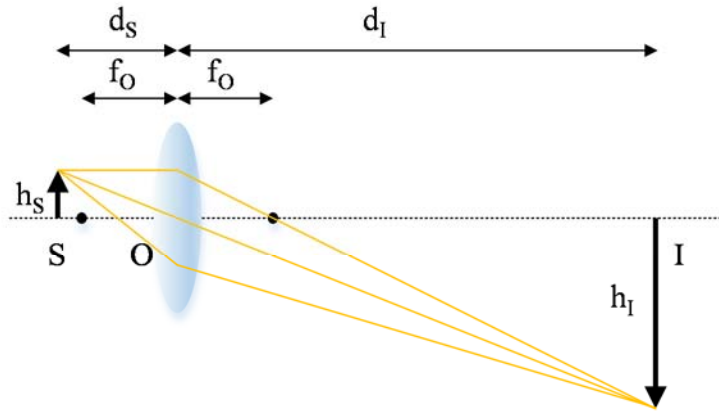
Light travels in an imaging system by obeying Fermat's principle [1]:

Light rays travel along the path of least time.

Because light has a different speed when it travels in different materials (by the ratio of refractive index), the light ray changes its direction by Fermat's principle when it encounters a new material. The lens is an optical part which utilizes this property of ray propagation to focus light rays that are parallel to the optical axis into a point, after traveling a designed focal length. Any lens component shown in this thesis can be described as a singlet lens or can be composed of multiple lens elements inside. In the case of a lens with multiple elements, we can replace the position and the focal length of a single lens with the principal plane and the effective focal length of a multi-element lens, respectively. In a finite corrected imaging system, a single objective lens, which is designed to correct optical aberrations at a fixed tube length, is used for image formation, as shown in Figure 1.2(a). By similarity of triangles in rays, the size of a sample (S) is magnified (or demagnified) by Equation (1.1):

$$M \equiv \frac{h_I}{h_S} = -\frac{d_I}{d_S}. \quad (1.1)$$

(a) Finite corrected system



(b) Infinity corrected system

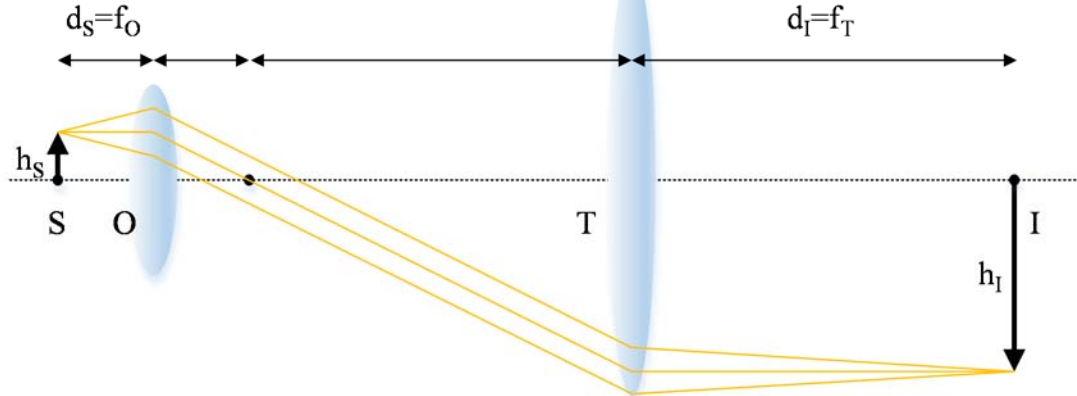


Figure 1.2: Finite corrected and infinity corrected imaging system. S: sample, O: objective lens, T: tube lens, I: image, d_s : sample distance, d_I : image distance, f_o : objective focal length, f_T : tube lens focal length, h_s : sample height, h_I : image height.

This type of configuration has an advantage in system complexity because only one lens is required in order to generate an image of the sample. However, it has a limited degree of freedom in the sample location for the best image formation, because the sample position (d_s) and objective focal length (f_o) are also coupled with the image's position (d_I) by the Gaussian Lens formula [2]:

$$\frac{1}{f} = \frac{1}{d_s} + \frac{1}{d_I}. \quad (1.2)$$

As a result, once an objective lens is used in the imaging system with a fixed tube length, we can only get the designed magnification of the image from just one possible position of sample. Furthermore, every optical component in the imaging system needs to be considered when designing the objective lens, because any additional parts in the imaging system between the objective lens and imaging plane would affect the system's aberration correction.

Infinity corrected imaging systems are another type of imaging system (Figure 1.2 (b)). Aberration of the infinity corrected objective lens is best corrected when the sample is located at the focal plane of the objective. As a result, light rays become parallel after passing through the objective lens, which makes an image of the sample positioned at infinity from the lens. An additional lens (tube lens) is used in the system in order to focus the image location to a closer distance. One of the advantages of an infinity corrected system is that the distance between the objective lens and the tube lens is flexible. In Figure 1.2 (b), the distance between the two lenses is set as the summation of the focal lengths of each, in a configuration known as the 4f imaging system. However, the separation between the lenses can be any distance as long as any rays passing through the objective lens can be collected by tube lens without loss. Along with the freedom of choosing the distance between the two lenses, this imaging system allows the user to modify it with less aberrations than the finite corrected system when inserting extra optical parts between the objective and the tube lens because all the rays are parallel in this region. Unlike finite corrected systems, the magnification of an infinity corrected system is only determined by the optical properties of the lenses in use, which is easily derived from the Figure 1.2(b) using the similarity of triangles in rays:

$$M \equiv \frac{h_I}{h_S} = -\frac{f_T}{f_O}. \quad (1.3)$$

1.2 Modern microscopy systems

Most modern microscopy systems are configured as infinity corrected systems in order to image with different modes according to different applications. In Figure 1.3, a typical configuration of the modern optical microscope is shown. The objective lens and tube lens constitute an infinity corrected imaging system, and an imaging sensor is located at the focal

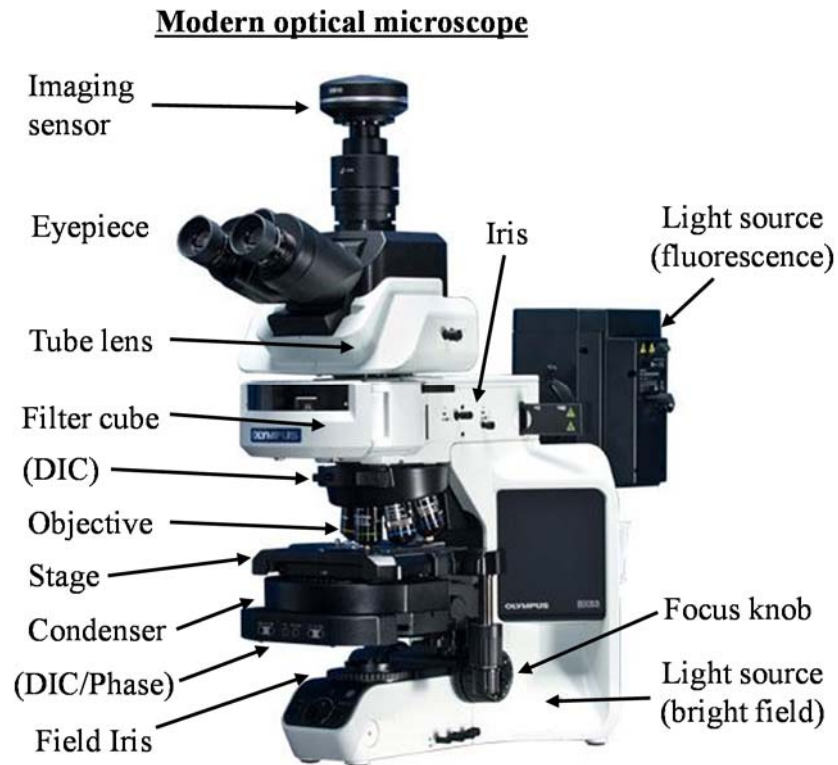


Figure 1.3: Configuration of modern optical microscope.

plane of the tube lens. The sample is usually loaded on the X-Y stage and the focus knob moves the sample stage or the objective lens nosepiece in order to focus the sample. There are two light sources installed in the microscope for sample illumination. One light source is used for transmission bright field imaging, and a more powerful light source is usually used for epi-fluorescence excitation. Additional filter cubes, phase rings, prisms, and polarizers are used for the specific imaging modes, such as fluorescence imaging, Zernike phase contrast imaging, and differential interference contrast (DIC) imaging.

1.2.1 Kohler illumination

Kohler illumination is one of the most widely used illumination methods in modern microscopy. In Kohler illumination, the light source plane and the sample plane are in Fourier transform relation, and as such each point source in the light source contributes equally through the whole area of sample illumination. As a result, the illumination on the sample plane is uniform regardless of intensity variation in the light source. Kohler illumination also

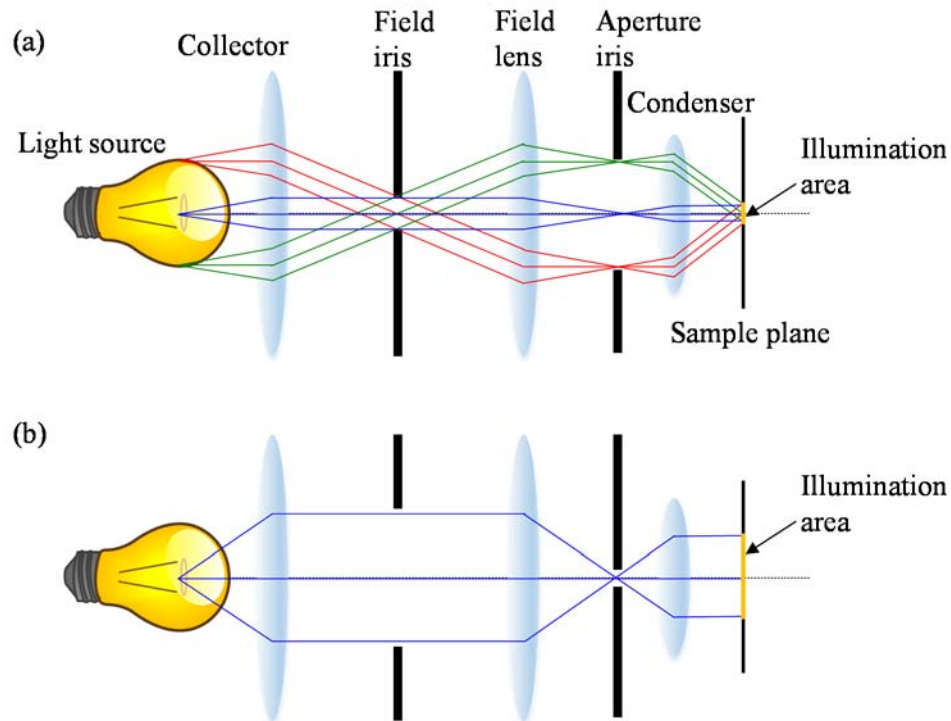


Figure 1.4: Microscope illumination path. Kohler illumination. (a) Small field and wide angle illumination. (b) Large field and direct illumination.

gives us easy control of the illumination. By positioning one iris (field iris) on the sample conjugate plane and the other iris (aperture iris) on the source conjugate plane, we can control the size of illumination and the angle of illumination independently of each other. Two opposite types of illumination methods are shown in Figure 1.4 as examples. A field iris determines the size of illumination, and an aperture iris determines how many source points contribute to the illumination on the sample and controls the maximum angle of illumination as a result. When the field iris is small and the aperture iris is large (Figure 1.4(a)), the illumination area on the sample plane is small but the illumination is made from multiple angled illumination sources, thus generating an incoherent illumination scheme. On the contrary, when the field iris is large and the aperture iris is small (Figure 1.4(b)), the light source illuminates a large area on the sample plane. However, the small aperture blocks light from most of the source points and passes light only from a small point source which generates a spatially coherent direct planar illumination.

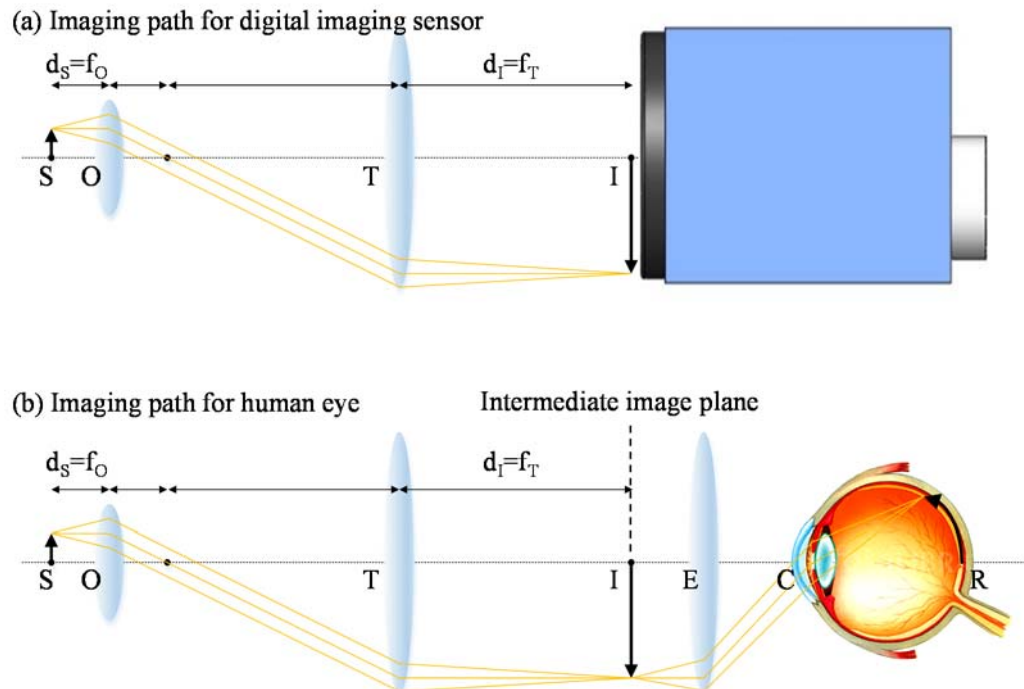


Figure 1.5: Microscope imaging path. (a) Imaging path for digital imaging sensor. (b) Imaging path for human eye. E: eyepiece, C: cornea, R: retina.

1.2.2 Photo detectors

In modern microscopy, there are two light paths for image detection: one for image recording using digital photodiodes, and the other for direct inspection with the human eye. For imaging recording purposes, 2D (dimensional) digital imaging sensors or single point detectors for scanning microscopes are currently in use. In this thesis, we focus on the 2D digital imaging sensors. A photodiode is a device which converts photons into electrons. As a result, if we position a 2D array of photodiodes on the image plane of an imaging system, as shown in Figure 1.5 (a), we can measure the amount of photons (intensity of light field) arriving at each location of the photodiode. Complementary Metal Oxide Semiconductor (CMOS) imaging sensors and Charge Coupled Device (CCD) imaging sensors are the two most commonly used digital imaging sensors. CMOS and CCD imaging sensors are similar in a sense that they both use photodiodes as a photo detection unit, however, they are different in their method of data transfer. CMOS imaging sensors amplify the generated photo-

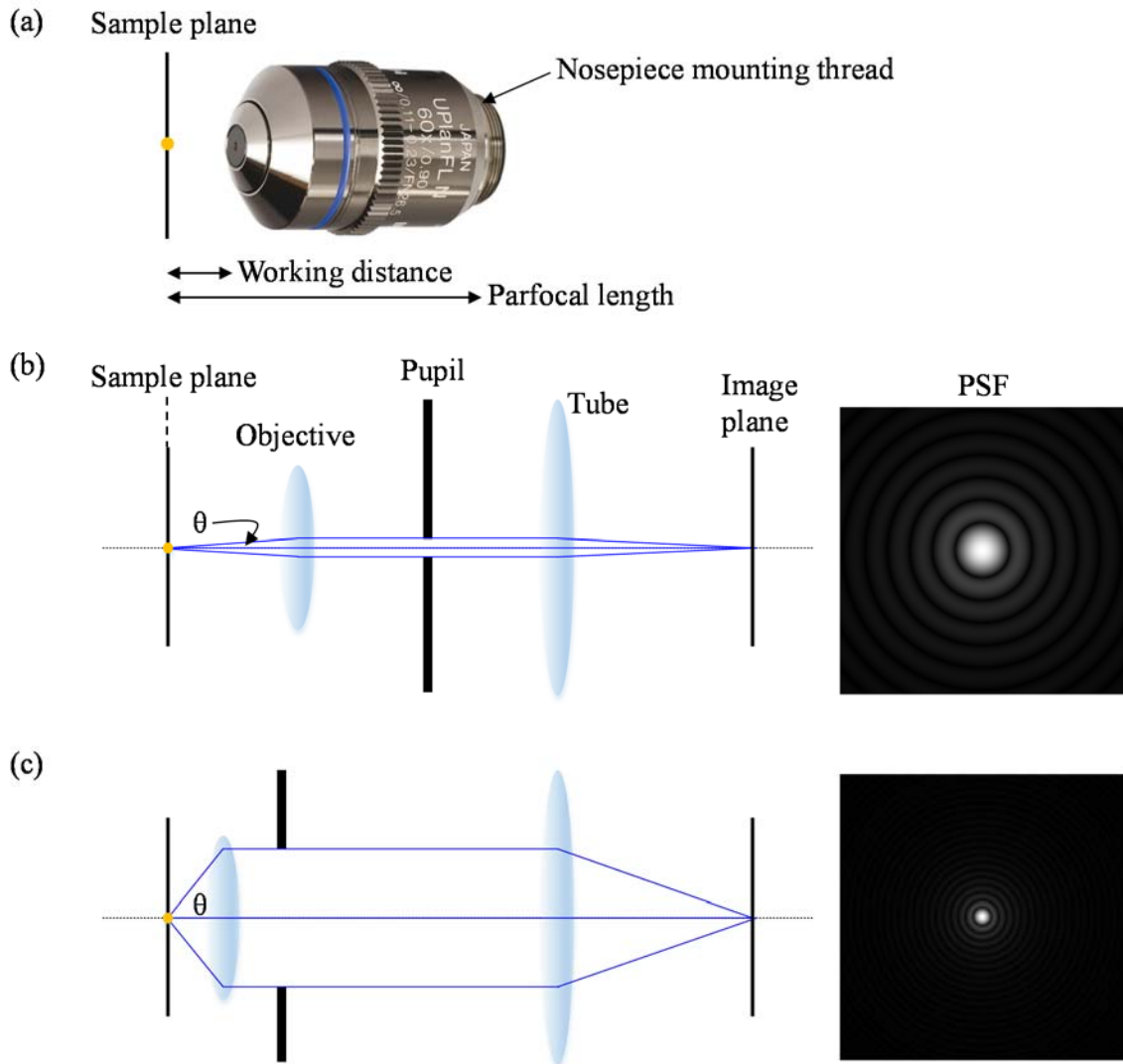


Figure 1.6: Microscope Objective lens. (a) Objective lens and terminology. (b) Imaging of a point source using a small NA objective lens. (c) Imaging of a point source using a large NA objective lens.

electrons directly at the position of the photodiode and transfer the voltage as an output. However, CCD imaging sensors transfer the generated electrons as an output and amplify them at the final stage of the sensor. Due to this difference, CMOS sensors have relatively small pixel sizes and a fast readout speed, however, they will usually have more noise related with voltage readout. On the contrary, CCD sensors have less noise, but have relatively large pixel sizes and slower speeds.

Table 1.1: Microscope tube length and objective thread size.

Company	Tube length [mm]	Thread size
Leica	200	M25
Nikon	200	M25 / M34
Olympus	180	RMS
Zeiss	165	M27 / M34

For the direct inspection of the generated image, we can direct the imaging path to our eyes. Unlike the digital imaging sensor, the human eye has its own light refracting parts (such as the cornea, aqueous humor, and lens), so an additional lens (eyepiece) is necessary in order to relay the image from the intermediate image plane to a plane which the human eye can focus into an image in its most relaxed state (usually 25 cm from the eye). Because our eyes demagnify the image by about 10 times when the sample is about 25 cm away (following Equation (1.1)), eyepieces usually have a 10X magnification in order to compensate this.

1.2.3 Objective lens

The objective lens is one of the most critical parts in a microscope system, which affects the quality of the image in many aspects. In order to give information on the objective's design specifications, the magnification of the objective, the numerical aperture (NA), the aberration correction type, the field number (FN), and the amount of coverglass thickness correction are usually listed on the label of the objective lens. Because most objective lenses are composed of several lens elements for aberration correction, it is not easy to focus the sample using the effective focal length of the objective lens. For the practical usage of the objective lens, many lens makers provide additional information such as the working distance and parfocal length as shown in Figure 1.6 (a). Because objective lenses from each lens maker are designed to be working with the microscope frame produced by the same companies, careful attention is required when using objective lenses with a microscope frame of different company. First, due to the difference in tube length, the magnification of the

image may be different in different microscope frames by following Equation (1.3). Additionally, the aberration correction of some objective lenses are designed together with the tube lens, so the image quality could be affected when it is used with other tube lenses. In table 1.1, microscope tube lengths and objective lens thread sizes of commonly used microscopes are listed.

1.2.3.1 Resolution

There are several definitions about image resolution, and one of the most popular definition is the Rayleigh criterion of two point sources. As described by the Rayleigh criterion [3], two nearby point sources are resolved when the peak intensity of the second point source image is located at the first minimum intensity of the first point source image. In order to use the Rayleigh criterion for image resolution, we need to know the characteristics of the image generated by the imaging system from a point source. The point spread function (PSF) is the irradiation distribution in the image plane from a point source. Using Fraunhofer diffraction theory [3], the PSF for a circular pupil has the shape in Equation (1.4):

$$I(r) = \left[\frac{2J_1(\pi r)}{\pi r} \right]^2, \quad (1.4)$$

where J_1 is the first order Bessel function of the first kind, and $r \equiv \rho D / \lambda f$, where ρ is distance in polar coordinates, D is the diameter of the pupil, and λ is the wavelength of light. The first zero of the above intensity distribution occurs at $r=1.22$ as shown in Figure 1.7 (b), which leads to the famous Rayleigh resolution criterion as shown in Equation (1.5):

$$Resolution = 1.22 \frac{\lambda}{D/f} \cong 0.61 \frac{\lambda}{NA}, \quad (1.5)$$

where NA is the numerical aperture of the objective lens defined as $NA = n \cdot \sin \theta$, where n is the refractive index of the material between the sample and the objective lens, and θ is the half angle of the objective aperture as shown in Figure 1.6 (b-c). As a result, an objective lens with a small NA and a small pupil size makes a large central lobe in the PSF, which means a low resolution in the resulting image (Figure 1.6 (b)). On the contrary, we need small PSF central lobe in order to get high resolution image, which requires a large NA objective lens (Figure 1.6 (c)).

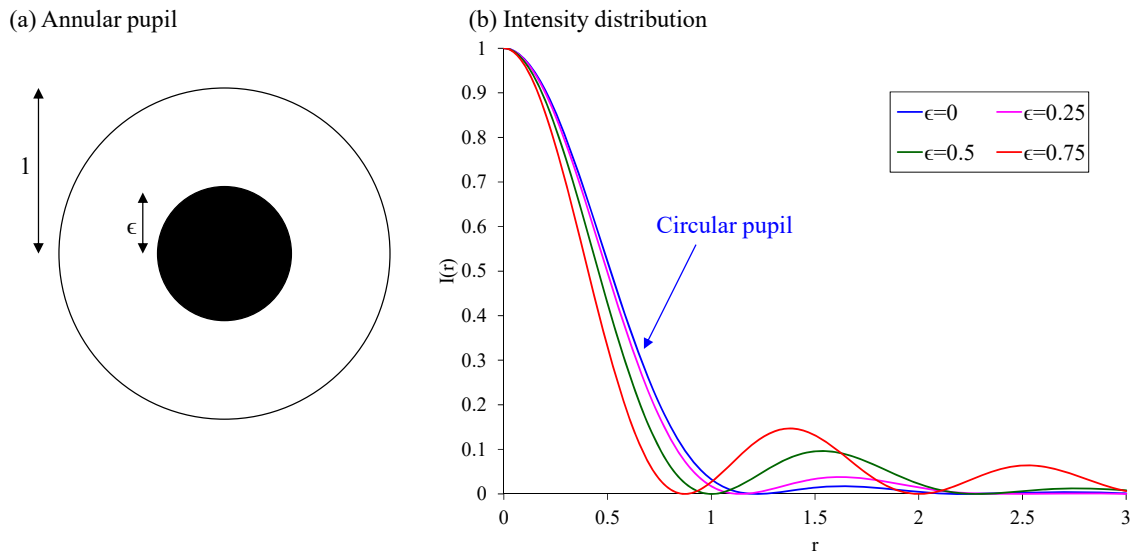


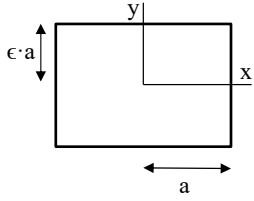
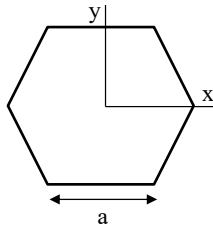
Figure 1.7: Systems with annular pupil. (a) Diagram of annular pupil. (b) Intensity distribution of PSF in systems with circular and annular pupil.

Because the shape of the pupil is directly related with the PSF and image resolution, there has been large effort on the engineering of pupil function. It is called “apodization” [3]. One of the basic approaches in apodization is to make a central light block on the pupil, making an annular pupil as shown in Figure 1.7 (a). The PSF for an annular pupil [4] has the form of Equation (1.6) and the intensity distribution of the PSF by variation of the obscuration ratio ϵ is shown in Figure 1.7 (b).

$$I(r) = \frac{1}{(1-\epsilon^2)^2} \left[\frac{2J_1(\pi r)}{\pi r} - \epsilon^2 \frac{2J_1(\pi \epsilon r)}{\pi \epsilon r} \right]^2. \quad (1.6)$$

There are two distinct changes in the PSF when the obscuration ratio ϵ increases. The first minimum intensity occurs at shorter distance from the peak intensity location, which reduces the smallest resolvable feature of the system. However, the intensity in the second maximum peak increases when ϵ increases, which generates ringing noises in the final image and reduces the quality of the imaging system. For the rectangular pupil and the hexagonal pupil, the PSF and resolution are listed in the Table 1.2 for reference [4].

Table 1.2: PSF and resolution of systems with rectangular and hexagonal pupil.

Pupil	Diagram	PSF	Resolution
Rectangular		$I(x, y) = \left(\frac{\sin \pi x}{\pi x} \right)^2 \left(\frac{\sin \pi \epsilon y}{\pi \epsilon y} \right)^2$	<i>x direction:</i> $0.5 \frac{\lambda}{a/f}$
			<i>y direction:</i> $0.5 \frac{\lambda}{\epsilon a/f}$
Hexagonal		$I(x, y) = \frac{4}{27} \left(\frac{4}{\pi^2 x(x^2 - 3y^2)} \right)^2 \times \left\{ \sqrt{3}x \left[\cos \frac{\pi x}{2} \cos \frac{\sqrt{3}\pi y}{2} - \cos \pi x \right] - 3y \sin \frac{\pi x}{2} \sin \frac{\sqrt{3}\pi y}{2} \right\}^2$	<i>x direction:</i> $0.665 \frac{\lambda}{a/f}$
			<i>y direction:</i> $0.675 \frac{\lambda}{a/f}$

Because the image is detected by photodetectors in the imaging system, the final system resolution is determined from both the diffraction limited optical resolution and the pixel size of the photo detector as in Equation (1.7):

$$\text{System resolution} = \max \left\{ \text{optical resolution}, \frac{1}{M} (2 \times \text{pixel size}) \right\}. \quad (1.7)$$

When the system resolution is determined by the size of the PSF central peak, the system is called “diffraction limited”. Otherwise, the system is called a “pixel limited” system.

1.2.3.2 Field of View

The field of view (FOV) of an imaging system is the area on the sample plane which a microscope can form an image simultaneously on the intermediate image plane. This is characterized by the field number (FN) of the objective lens which indicates the diameter of the imaging field on the intermediate image plane (back focal plane of the tube lens). As a result, it is desired to make the size of an imaging sensor on the intermediate image plane

larger than the FN of the objective lens. The system FOV is determined by comparing the size of the imaging sensor and the FN of the objective lens as in Equation (1.8):

$$\text{System FOV} = \frac{1}{M} \min\{\text{Imaging sensor size}, FN\}. \quad (1.8)$$

1.2.3.3 Depth of Field

The depth of field (DOF) is the axial distance from the sample focal plane which simultaneously makes a focused image in the intermediate image plane. As a result, it is related with the axial resolution of an imaging system and is defined as in Equation (1.9) using the wave nature of light [3]:

$$\text{DOF} = \frac{\lambda \cdot n}{NA^2}. \quad (1.9)$$

Because the DOF has inverse square relation with the NA, it becomes more difficult to focus a sample using a high NA objective lens. In other words, a low NA objective lens has poorer axial resolution and needs additional methods for 3D sectioning of the sample.

1.3 Aberration

All the above discussion on image formation using an optical imaging system is based on several approximations about wave and ray properties of light propagation. The actual position, size, and shape of the generated image are slightly different from the theory. The deviation of the actual image from the theoretical approximation is called “aberration” of the system [5, 6]. There are many different sources of aberration in an imaging system. Material property, design parameters, and fabrication tolerance of optical elements all affect the way light propagates and become common sources of aberration. Even in the perfectly fabricated optical elements as defined by theoretical design, the theory itself contains several approximations, such as the paraxial approximation and thin lens approximation. It is best if the imaging system corrects the inherent aberration using systematic design; however, it is impractical to design an optical system which corrects aberrations with regard to all possible imaging applications. As a result, it is important to know how much and what types of aberration exists in the imaging system and what is the source of the aberration.

1.3.1 Chromatic aberration

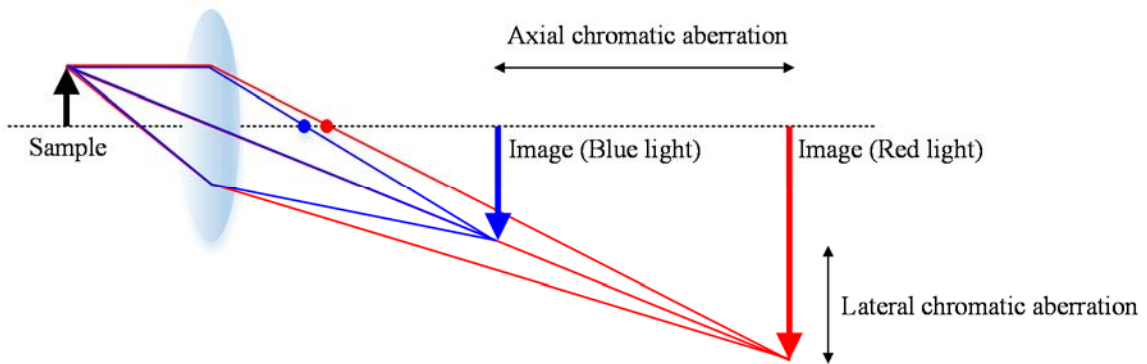


Figure 1.8: Chromatic aberration.

Chromatic aberration arises due to the dispersive nature of light in the refractive optical elements when polychromatic light is in use [2]. Refractive index is a material property which determines how light rays refract when it encounters a new material by following Fermat's principle. The main source of chromatic aberration is dependent on the differences in refractive index of the wavelengths that make up the polychromatic light. By the lens maker's law [2] of Equation (1.10), the focal length of a lens changes by the wavelength of light, which results in chromatic aberration in the imaging system.

$$\frac{1}{f} = (n(\lambda) - 1) \left(\frac{1}{R_1} - \frac{1}{R_2} \right), \quad (1.10)$$

where $n(\lambda)$ is the refractive index which is a function of wavelength λ , and R_1 and R_2 are the radius of curvature of the two sides of the lens. Because different colored lights have different focal lengths from the same lens, they make different images due to the chromatic aberration as shown in Figure 1.8. The effect of chromatic aberration on the image is twofold. The images from different colors have different image planes in the axial direction, and cannot be focused simultaneously when the DOF of the system is small. This is called the "axial chromatic aberration." Not only is this the result of the aberration, but the images from different colors have different spatial magnification, which generates two different sized images with different colors. This is called the "lateral chromatic aberration".

At least two different materials of different dispersive power are necessary in order to correct chromatic aberrations. The most common index for material dispersive power is the Abbe number as in Equation (1.11):

$$V_d = \frac{n_d - 1}{n_F - n_C}, \quad (1.11)$$

where d, F, and C are the Fraunhofer lines for wavelengths 587.6 nm, 486.1 nm, and 656.3 nm, respectively. The lower the Abbe number, the greater the dispersive power. By how many Fraunhofer lines are corrected in chromatic aberration, the commercial objective lenses are designated as achromatic, semi-apochromatic, and apochromatic lenses in increasing order of corrective ability.

1.3.2 Achromatic aberration

When a monochromatic light source is used in the imaging system, there exists other types of aberrations other than chromatic aberrations. For an imaging system which has a circular pupil, the possible aberrations of an imaging system that is rotationally symmetric about its optical axis have the shape of phase variation on the pupil function. There are several different expressions on the phase pupil function, and it is commonly expanded in terms of Zernike circle polynomials. Each Zernike orders are called Zernike aberrations. In Table 1.3, the first 15 terms of Zernike aberrations are listed along with their phase map and PSF.

1.3.2.1 Tilt

When there is any phase gradient on the pupil function into a certain direction, it is called tilt aberration. Because the tile aberration shifts the PSF function without modifying its shape, the final image also shifts the same ratio while maintaining the quality of the image.

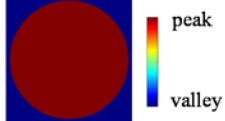
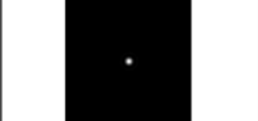
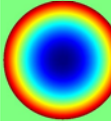
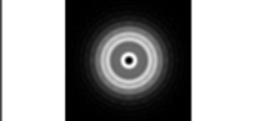
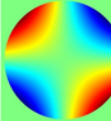
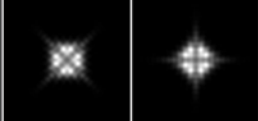
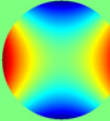
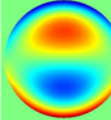
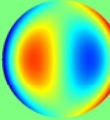
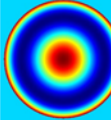
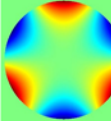
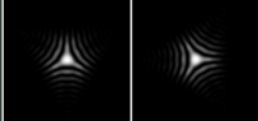
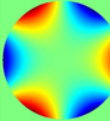
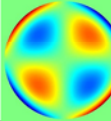
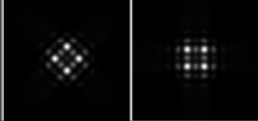
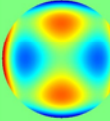
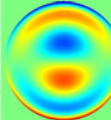
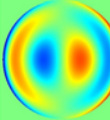
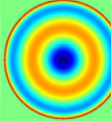
1.3.2.2 Defocus

When the image is observed at a different plane rather than the actual image plane, or when one of the imaging elements of the system is displaced along its optical axis, defocus aberration arises. Because the center intensity of the PSF is darker than the surrounding intensity, it generates a blurry image rather than a focused image.

1.3.2.3 Astigmatism

Astigmatism and coma aberrations are typical off axis achromatic aberrations. Astigmatism is made when meridional rays and sagittal rays from an off-axis sample are not

Table 1.3: Zernike aberrations.

Aberration	Zernike order	Zernike orthogonal circle polynomial	Pupil function	PSF
Piston	Z_0^0	1		
Tilt	Z_1^{-1}	$\rho \sin \theta$		
	Z_1^1	$\rho \cos \theta$		
Defocus	Z_2^0	$2\rho^2 - 1$		
Primary Astigmatism	Z_2^{-2}	$\rho^2 \sin 2\theta$		
	Z_2^2	$\rho^2 \cos 2\theta$		
Primary Coma	Z_3^{-1}	$(3\rho^3 - 2\rho) \sin \theta$		
	Z_3^1	$(3\rho^3 - 2\rho) \cos \theta$		
Primary Spherical aberration	Z_4^0	$6\rho^4 - 6\rho^2 + 1$		
Elliptical coma	Z_3^{-3}	$\rho^3 \sin 3\theta$		
	Z_3^3	$\rho^3 \cos 3\theta$		
Secondary Astigmatism	Z_4^{-2}	$(4\rho^4 - 3\rho^2) \sin 2\theta$		
	Z_4^2	$(4\rho^4 - 3\rho^2) \cos 2\theta$		
Secondary Coma	Z_5^{-1}	$(10\rho^5 - 12\rho^3 + 3\rho) \sin \theta$		
	Z_5^1	$(10\rho^5 - 12\rho^3 + 3\rho) \cos \theta$		
Secondary Spherical aberration	Z_6^0	$20\rho^6 - 30\rho^4 + 12\rho^2 - 1$		

converged into the same focal point. Due to the difference in focal lengths of both rays, the

intensity (energy) along both rays is weaker than in other directions, which result in the elongation of an image in certain directions symmetrically.

1.3.2.4 Coma

Coma aberration is created when the principal rays and marginal rays of an off-axis sample are not coincident at the image plane. As its name suggests, its PSF looks like a coma. Due to the asymmetry of the PSF, the image affected by coma aberration smears into a certain direction.

1.3.2.5 Spherical aberration

Spherical aberration is an aberration related with the shape of an optical element. If the curvature of an optical element is not parabolic, not all of parallel rays coincide at a focal point. Due to the strong secondary rings in the PSF, an image suffering from spherical aberration has ringing noises around the boundary.

1.3.2.6 Strehl ratio

As seen in Table 1.3, the energy in PSF from aberrated systems are not concentrated like that from aberration-free systems, but spread into nearby areas. As a result, the energy of sample would also be spread into nearby areas when an image is generated from the aberrated system, which would reduce the quality of the image. The Strehl ratio is a commonly used index for aberration status of an imaging system [6]. For a given total power in the pupil, the value of the central irradiance for an aberrated pupil relative to its value for an unaberrated pupil is called the Strehl ratio of the imaging system. When the Strehl ratio is larger than 0.8, the system is called “diffraction limited,” otherwise it is called “aberration limited.”

1.4 Imaging modes

Modern microscopes have multiple imaging modes which are suitable for specific applications. In this section, we describe the basic imaging principles of typical imaging modes.

1.4.1 Bright field intensity imaging

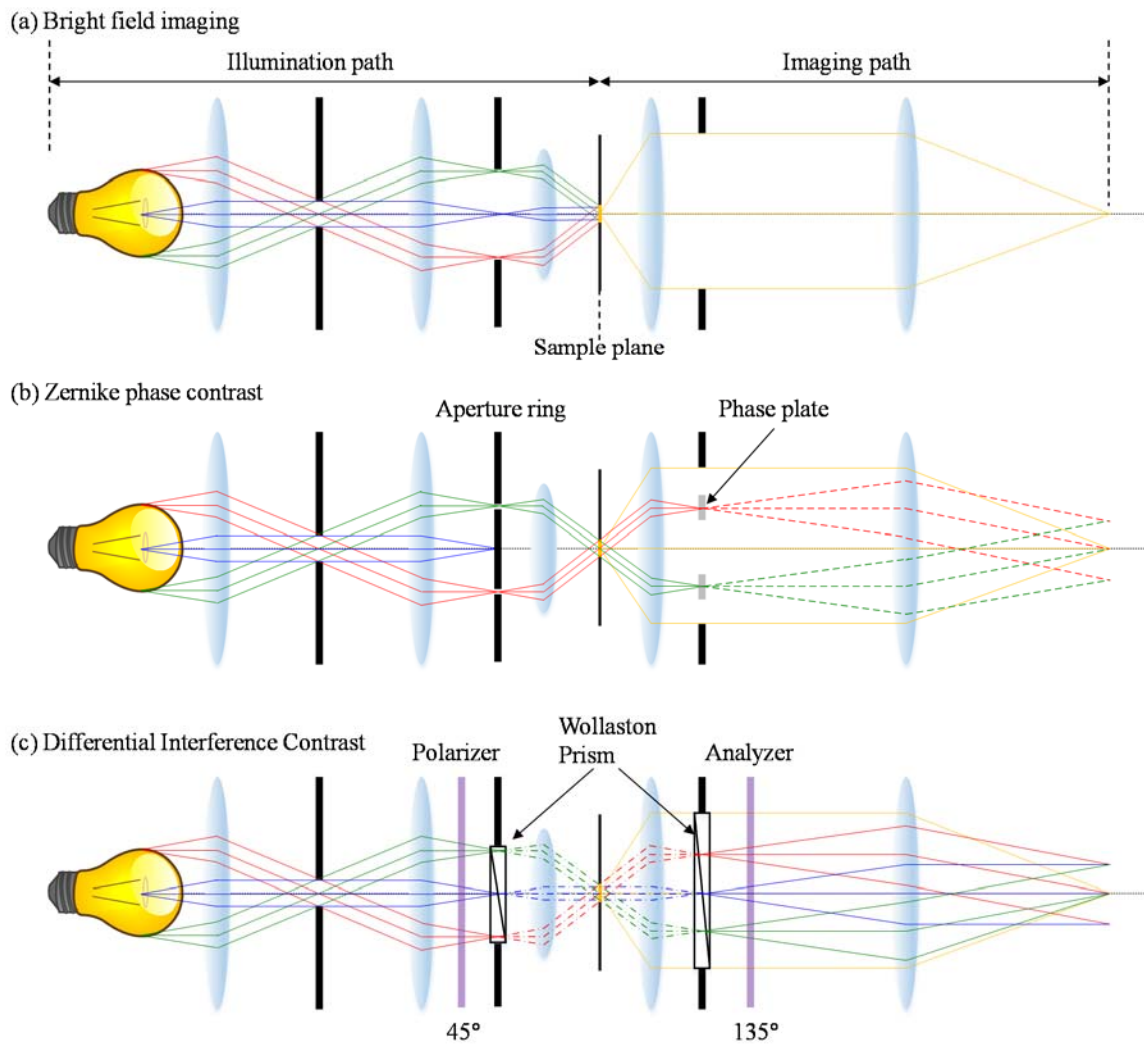


Figure 1.9: Bright field imaging modes. (a) Bright field intensity imaging. (b) Zernike phase contrast imaging. (c) Differential Interference contrast imaging.

The most fundamental imaging mode is the bright field intensity imaging as shown in Figure 1.9 (a). In conventional Kohler illumination, the sample is illuminated by incoherent multiple light sources, and as such, the intensity of the sample information is transferred into the image. When the sample, described by $s(\vec{x}) = a(\vec{x}) \cdot e^{i\phi(\vec{x})}$, where $a(\vec{x})$ and $\phi(\vec{x})$ are real valued functions, is illuminated by incoherent light sources, the image is formed by Equation (1.12) following Fourier optics [7]:

$$i(\vec{x}) = \mathcal{F}^{-1} \left\{ \mathcal{F} \left\{ |s(\vec{x})|^2 \right\} \cdot OTF \right\}$$

$$= \mathcal{F}^{-1} \left\{ \mathcal{F} \left\{ |a(\vec{x})|^2 \right\} \cdot OTF \right\} = |a(\vec{x})|^2 \otimes PSF, \quad (1.12)$$

where \mathcal{F} and \mathcal{F}^{-1} are the Fourier transform and inverse Fourier transform, respectively, OTF is the optical transfer function which has a Fourier transform relation with the PSF, and \otimes is the convolution integral operator. In bright field imaging, the image is the result of the convolution integral of the sample intensity distribution and the point spread function of the imaging system.

1.4.2 Zernike phase contrast imaging

When the sample is transparent, such as most biological samples are, then the bright field intensity image does not give us much detail about the sample because it only uses intensity (light absorption) information of the sample it is imaging. For those transparent samples, imaging the phase of the sample gives much more useful information about the sample's details. In 1935, Zernike invented a method to record the phase changes introduced by the sample using a photodetector, and it is called Zernike phase contrast, or just phase contrast, microscopy [3]. The basic working principle of Zernike phase contrast imaging is shown in Figure 1.9 (b). In phase contrast microscopy, an aperture ring is positioned at the location of the aperture iris of the condenser lens. Due to this aperture ring, only certain angles of illumination are made on the sample, which constitute zeroth order diffraction directions. Along with the aperture ring, a special objective lens also contains a phase plate inside at the back focal plane of the objective lens. The phase plate also has a ring shape and matches the size of the ring with the size of the aperture ring, making phase changes only to the zeroth order diffraction from the sample. Let's assume the sample is perfectly transparent and only has phase changes like those described by $s(\vec{x}) = e^{i\phi(\vec{x})}$. We can expand $s(\vec{x})$ into a Fourier series,

$$s(\vec{x}) = \sum_{m=-\infty}^{\infty} c_m e^{\frac{2\pi i \cdot m \vec{x}}{d}}, \quad (1.13)$$

where c_m is the coefficient of the m th order diffraction, and d is the fundamental period of $\phi(\vec{x})$. Let's assume that the phase variation of the sample is small, such that the magnitude of $\phi(\vec{x})$ is small compared to unity. Then $s(\vec{x})$ can be approximated as,

$$s(\vec{x}) \cong 1 + i\phi(\vec{x}). \quad (1.14)$$

Comparing Equation (1.13) and (1.14),

$$c_0 = 1, c_{-m} = -c_m^* (m \neq 0). \quad (1.15)$$

In phase contrast imaging, the phase plate inside the objective lens makes a one-quarter phase delay only onto the zeroth order diffraction. As a result, the diffraction coefficients change after passing through the phase plate like Equation (1.16):

$$c'_0 = c_0 e^{i\frac{\pi}{2}} = i, c'_m = c_m (m \neq 0). \quad (1.16)$$

The resultant image on the photo detector is described by Equation (1.17):

$$i(\vec{x}) = |i + i\phi(\vec{x})|^2 \cong 1 + 2\phi(\vec{x}). \quad (1.17)$$

Unlike the image Equation (1.12) produced by bright field intensity imaging, the phase changes introduced by the sample are transformed into changes in intensity of the image, which are recorded using a general photodetector. Zernike phase contrast imaging is a useful mode in imaging transparent biological samples; however, if the sample is thick and phase variation is not small compared to unity, noise related with additional phase terms are added into the final image.

1.4.3 Differential interference contrast imaging

Differential interference contrast (DIC) imaging is another commonly used phase imaging modality. DIC utilizes the polarization of light in order to gauge the phase gradient on the sample. The configuration of DIC is shown in Figure 1.9 (c). Birefringence of the Wollaston prism, which is located in the aperture iris plane of the condenser, separates a plane of linearly polarized light rays into two spatially separated, orthogonally polarized rays (o-ray: ordinary ray, and e-ray: extraordinary ray). If there is any phase difference in the sample within this small separation of the two rays, the o-ray advances or retards the e-ray in phase by the amount of the phase difference by passing the sample plane. Another Wollaston prism inside the objective lens combines these two rays again into one light ray. Because the analyzer direction is 90° rotated to the polarizer, destructive wave interference between the o-ray and e-ray occurs when passing through the analyzer. Unlike Zernike phase contrast imaging, the phase gradient of the sample is transformed into changes in intensity

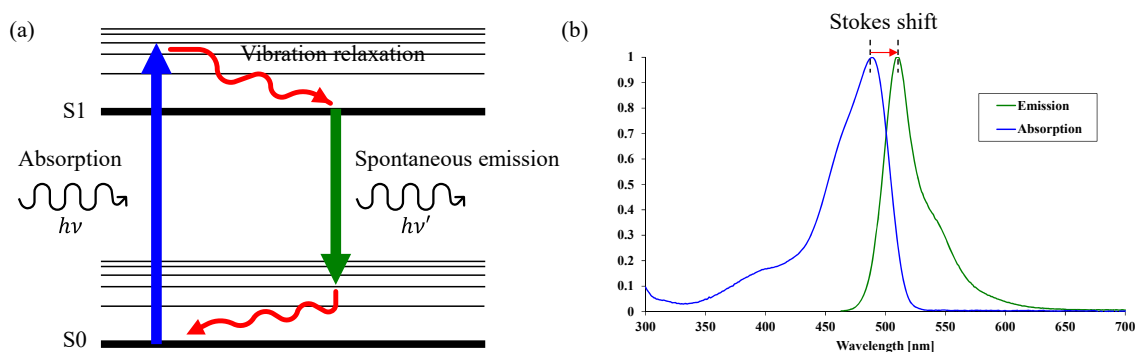


Figure 1.10: Fluorescence imaging. (a) Fluorescence imaging principle. (b) Absorption and emission spectra for GFP.

of the image in DIC imaging. Because DIC utilizes birefringence as its working principle, it is not compatible with birefringent samples.

1.4.4 Fluorescence imaging

Fluorescence imaging is another frequently used imaging modality in modern microscopy. Fluorescence imaging utilizes light-matter interaction in fluorescing molecules (fluorophores). By quantum mechanics, there are several energy states in which molecules can reside. When molecules in the ground electronic state (S0) are illuminated by a light source of frequency (ν), part of the photons in the light source are absorbed by the molecules and excite them into higher energy states. Because there exist vibrational states and rotational states near these electronic states, light from certain bands of the spectrum can be absorbed by fluorophores. Naturally, it is called the absorption spectrum of a fluorophore. Once a molecule is excited, it quickly loses energy by vibrational relaxation and goes to the closest electronic state (S1). Due to the statistical nature of electron distribution, the excited molecule emits a photon of frequency (ν'), and returns back to ground state (S0). Because this light emission process is spontaneous, there is no relation between the emitted lights and they are incoherent of each other. Due to the energy loss during vibrational relaxation, the frequency of the emitted photon is always lower than the frequency of the absorbed photon ($\nu > \nu'$). This energy loss process is called “Stokes shift.” The Jablonski energy diagram of the fluorescence imaging process, as well as the absorption and emission spectra of green fluorescence protein (GFP), is shown in Figure 1.10. More detailed information on the

Table 1.4: Wavelength for maximum absorption and emission.

Fluorophore	Absorption [nm]	Emission [nm]
DAPI	359	491
Alexa 350	343	440
CFP	436	477
FITC	495	519
Alexa 488	499	520
GFP	489	511
TRITC	550	573
YFP	514	527
Texas Red	589	610
mCherry	587	610
Alexa 594	594	618

absorption and emission spectrum, excitation/emission filter, and dichroic beam splitter of fluorophores can be found at [8]. In Table 1.4, wavelengths for maximum absorption and emission of commonly used fluorophores are listed for reference.

FOURIER PTYCHOGRAPHIC MICROSCOPY

Fourier ptychographic microscopy (FPM) is a recently developed computational microscopy method which can improve the space-bandwidth product (SBP) of an imaging system by effectively increasing the resolution of a captured image using computational reconstruction algorithms [9]. FPM borrows ideas from conventional ptychography and the synthetic aperture. The word ptychography is a compound word of Greek words *ptyche* which means “to fold” and *graphein* which means “to write.” As a whole, ptychography means a method of mathematically folding two functions together using convolution. Historically, it was first used by a German physicist Walter Hoppe to describe coherent diffractive imaging (CDI), a conventional ptychographic microscope [10]. Conventional ptychography captures multiple diffraction images from different parts of a sample using a coherent light source. Because each diffraction pattern is obtained from a region which overlaps with other parts of the sample, there is a large degree of redundancy in the captured data which is used to retrieve the phase information from the diffractive intensity measurements. On the other hand, Fourier ptychography captures multiple images from the same part of a sample using different illumination sources. Here, the overlap is made on the Fourier spectrum of the captured images. In this chapter, the working principle and imaging process of FPM will be explained.

2.1 FPM image acquisition process

FPM image acquisition is basically the same as the normal bright field imaging process except FPM utilizes coherent illumination for imaging. In Figure 2.1, the image acquisition process of FPM is shown. In the case of incoherent imaging, the intensity information of the sample is used for final image generation. However, the electromagnetic field information of the sample is used in coherent imaging during the imaging process. When a direct plane wave is incident on the sample, the complex valued electromagnetic field information $s(x, y) = |s(x, y)|e^{i\angle s(x, y)}$ is Fourier transformed ($S(k_x, k_y) = \mathcal{F}\{s(x, y)\}$) when it passes

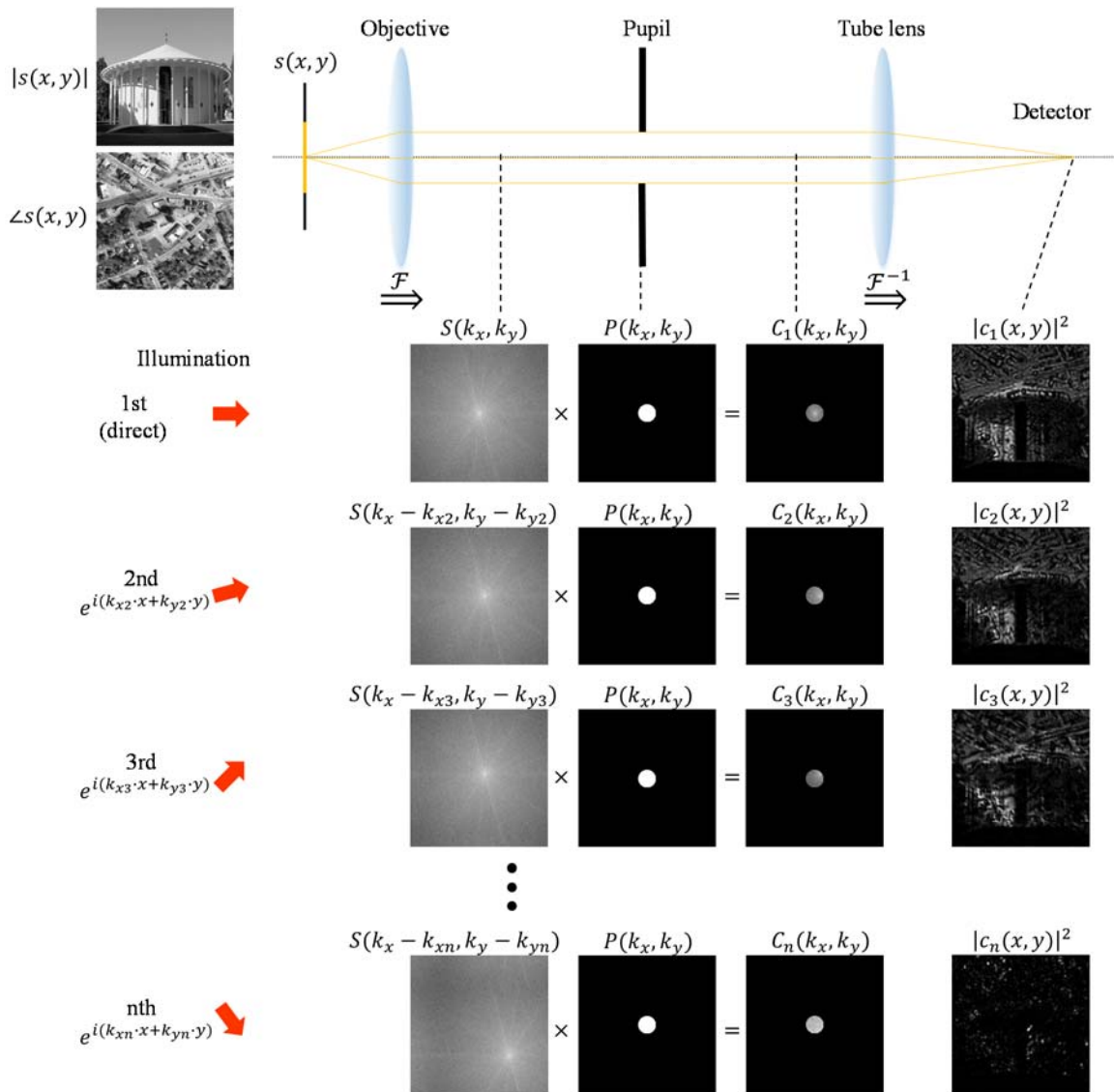


Figure 2.1: FPM image acquisition process.

through the objective lens as theorized by Fourier optics [7]. On the back focal plane of the objective lens, there exists an aperture pupil $P(k_x, k_y)$ which limits the maximum allowed spatial frequency through the imaging system. After being filtered by the aperture pupil ($C(k_x, k_y) = S(k_x, k_y) \times P(k_x, k_y)$), the resultant spectrum is inverse Fourier transformed again ($c(x, y) = \mathcal{F}^{-1}\{C(k_x, k_y)\}$) when passing through the tube lens, before being

captured by a photodetector ($i(x, y) = |c(x, y)|^2$). This process is summarized in Equation (2.1).

$$\begin{aligned} i(x, y) &= |\mathcal{F}^{-1}\{S(k_x, k_y) \cdot P(k_x, k_y)\}|^2 \\ &= |\mathcal{F}^{-1}\{\mathcal{F}\{s(x, y)\} \cdot P(k_x, k_y)\}|^2. \end{aligned} \quad (2.1)$$

In an aberration-free imaging system, the pupil function P has a shape of top hat function in amplitude and does not have variation in phase. The pupil function of aberration-free imaging system can be described as Equation (2.2):

$$P(k_x, k_y) = \begin{cases} 1, & \text{if } (k_x^2 + k_y^2) \leq k_c^2 \\ 0, & \text{if } (k_x^2 + k_y^2) > k_c^2 \end{cases}, \quad (2.2)$$

where k_c is the cutoff spatial frequency of the pupil function which determines the maximum allowed amount of information through the aperture and is defined as $k_c \equiv 2\pi \frac{NA}{\lambda}$. In the case of direct planar illumination, because the pupil function transfers only low spatial frequency terms from sample information, the captured image is basically a low pass spatially filtered version of the sample.

In Fourier ptychography, we make minor movements of the sample spatial spectrum $S(k_x, k_y)$ and capture multiple images from different spectral locations of the sample. Because the movements are made in the spatial frequency domain of the captured images, the sample position of the illumination does not change, but the direction of coherent illumination on the sample changes. If we illuminate the sample from \vec{k}_j direction, the illumination wave adds an additional phase gradient through the direction on the sample plane as Equation (2.3):

$$e^{i\vec{k}_j \cdot \vec{x}} = e^{i(k_{xj}x + k_{yj}y)}. \quad (2.3)$$

If the sample is thin under the 1st Born approximation [11], the extra phase gradient directly applies into the sample field information and propagates through the imaging system together with the sample information as Equation (2.4):

$$i_j(x, y) = |\mathcal{F}^{-1}\{\mathcal{F}\{s(x, y) \cdot e^{i(k_{xj}x + k_{yj}y)}\} \cdot P(k_x, k_y)\}|^2$$

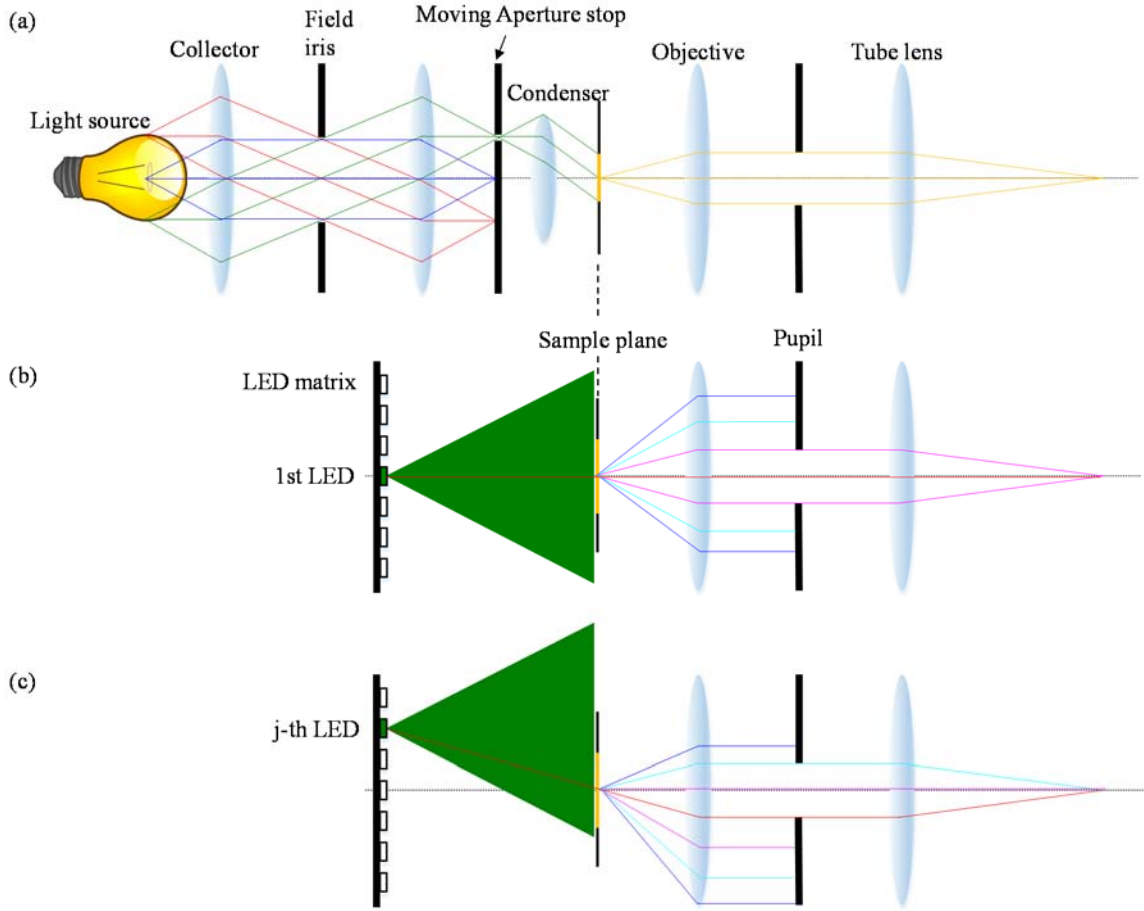


Figure 2.2: FPM illumination methods. (a) Aperture stop control. (b and c) LED matrix. (b) An LED on optic axis operation for direct illumination. (c) An LED on off-axis operation for oblique illumination.

$$= |\mathcal{F}^{-1}\{S(k_x - k_{xj}, k_y - k_{yj}) \cdot P(k_x, k_y)\}|^2. \quad (2.4)$$

As we can see from Equation (2.4), the sample spectrum information S shifts in the spatial frequency domain by the amount of the illumination angle by following the Fourier transform shift property. Because the pupil function is always the same regardless of the illumination angle, the aperture pupil eventually filters out different parts of the spatial spectrum of the sample field information by changing the direction of illumination. During the FPM image acquisition process, the multiple intensity images from a sample are captured from different

illumination conditions, and they all have different spatial spectral information about the sample which will be used later during the image reconstruction process.

In order to make varying angled coherent light illuminations, a single light source can be modulated to change its light direction, or multiple light sources are used to illuminate the sample from different source positions. A simple method of changing the illumination angle from a single light source is shown in Figure 2.2 (a). In Kohler illumination, the angle of illumination is controlled by the aperture iris of a condenser lens. If we replace the aperture iris with a moving aperture stop or spatial light modulator (SLM), we can control the location of the passing light beam and modulate the angle of illumination. This type of illumination method can be easily adapted into a conventional microscope because it only requires the aperture replacement. However, a very intense light source is necessary because only a small portion of light can pass through the small aperture for coherency of illumination. Also the maximum illumination angle is limited by the numerical aperture and aberration of the condenser lens. As a result, it is difficult to make large angled illumination conditions.

The most widely used illumination method for Fourier ptychography is using a light emitting diode (LED) matrix and turning on each LED at a time to make different illumination angles as shown in Figure 2.2 (b-c). This type of illumination method has many advantages. First, it is easy to use because there is no lens element related with this illumination method and only the LED matrix is necessary for the varied angle illumination. Second, the LED device is small enough to generate spatially coherent illumination on the sample plane, and at the same time strong enough to create sample scattering signal which is detectable to typical imaging sensors. Furthermore, the LED matrix has an additional advantage in designing compact imaging systems because each LED device can be shared with multiple imaging systems. However, the illumination from a small sized light source makes slightly different incident angles on different location on the sample plane especially when the FOV of the imaging system is large. Furthermore, due to the finite size of each LED device, the area of which the illumination is coherent is limited by coherent length of the light source on sample plane. From the Van Cittert-Zernike theorem [12], a light source of finite size of w becomes coherent within a coherent length determined by Equation (2.5):

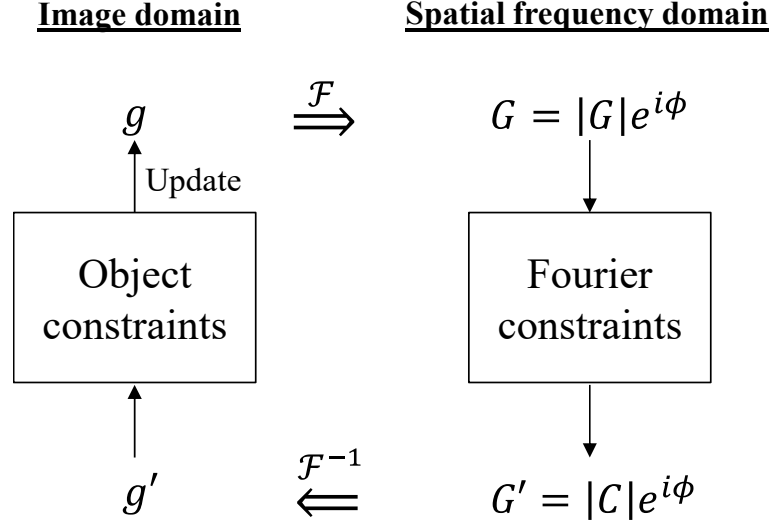


Figure 2.3: Phase retrieval algorithm.

$$L_c = \frac{\lambda z}{w}, \quad (2.5)$$

where L_c is the coherent length, λ is the wavelength of the light source, and z is the distance of the sample plane from the light source. For the FPM imaging system which covers a wide FOV, it is required to split the whole FOV into small image segments which are under the coherent illumination condition during the reconstruction process.

2.2 FPM image reconstruction process

The main goal of the FPM image reconstruction process is to reconstruct the complex-valued sample spectral information using multiple intensity-only captured images. The problem of reconstructing complex information from intensity measurements has been discussed as a “phase retrieval” problem [13, 14]. The general diagram of the phase retrieval algorithm is shown in Figure 2.3. The iterative phase retrieval algorithm utilizes Fourier transform relationships between the image plane and the spatial frequency plane. On the spatial frequency domain, the measured diffractive intensity information is used as Fourier constraints. And on the image domain, object constraints, such as non-negativity or

translationally diversity information, are used for image updating for every iteration. As the iteration goes on, both constraints impose boundaries on the possible phase distribution, which converges into a final phase retrieval result. There are several different phase retrieval methods based on how to update the input of next iteration ($g_{k+1}(\vec{x})$) from the output of current iteration ($g'_k(\vec{x})$). Some of the most frequently used algorithms are listed in Equation (2.6).

$$\begin{aligned}
 \text{Gerchberg – Saxton algorithm: } g_{k+1}(\vec{x}) &= \begin{cases} g'_k(\vec{x}), & x \notin \gamma \\ g_k(\vec{x}), & x \in \gamma \end{cases} \\
 \text{Input – Output algorithm: } g_{k+1}(\vec{x}) &= \begin{cases} g_k(\vec{x}), & x \notin \gamma \\ g_k(\vec{x}) - \beta \cdot g'_k(\vec{x}), & x \in \gamma \end{cases} \\
 \text{Output – Output algorithm: } g_{k+1}(\vec{x}) &= \begin{cases} g'_k(\vec{x}), & x \notin \gamma \\ g'_k(\vec{x}) - \beta \cdot g'_k(\vec{x}), & x \in \gamma \end{cases} \\
 \text{Hybrid Input – Output algorithm: } g_{k+1}(\vec{x}) &= \begin{cases} g'_k(\vec{x}), & x \notin \gamma \\ g_k(\vec{x}) - \beta \cdot g'_k(\vec{x}), & x \in \gamma \end{cases} \quad (2.6)
 \end{aligned}$$

where β is a constant, and γ is the set of points at which $g'_k(\vec{x})$ violates the object constraints. Each algorithm has different convergence speed and reconstruction error ratio depending on the type of experiments. For those who are interested in the details about the algorithms, a comparison between algorithms is given in [13].

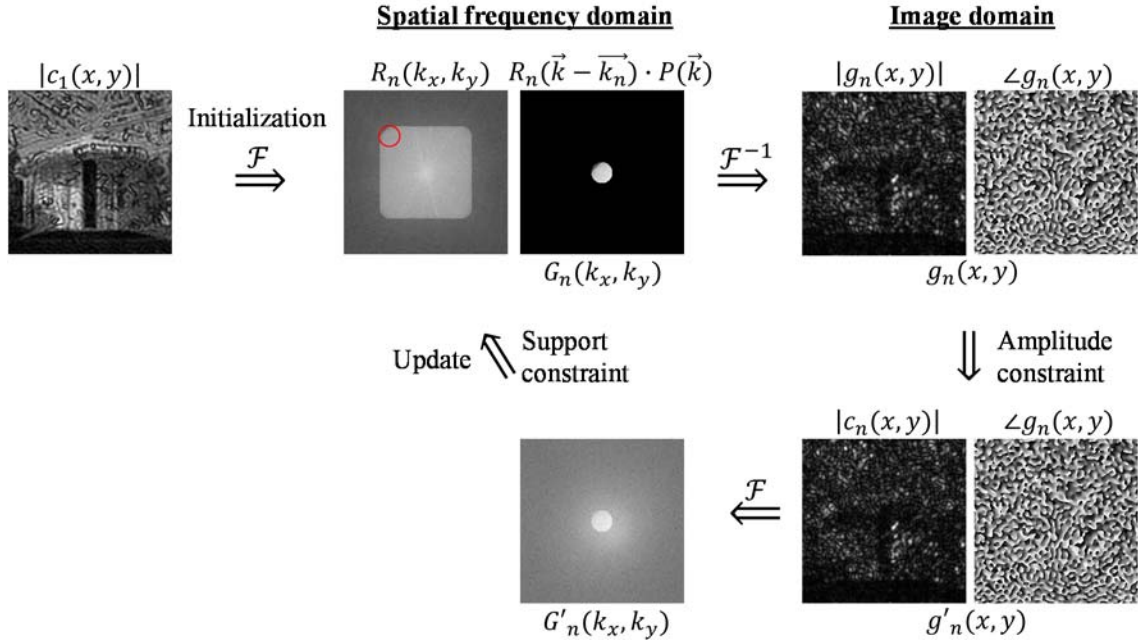


Figure 2.4: FPM image reconstruction process.

The FPM image reconstruction process is fundamentally similar to the above phase retrieval algorithm except that the role of the image domain and the spatial frequency domain is exchanged by each other. In FPM, every intensity measurement is done at the image domain, the measurement amplitude constraint is on the image domain rather than the spatial frequency domain. As initialization, an up sampled version of the directly illuminated captured image (or any types of initial guess such as constant intensity image) is Fourier transformed into the spatial frequency domain and generates an initial reconstruction spectrum $R_0(\vec{k})$. For each captured image, the reconstruction spectrum $R_j(\vec{k})$ is shifted and filtered by the pupil function using *a priori* knowledge of the amount of shift of sample spectrum $S(\vec{k})$ under the capture condition. The filtered spectrum is inverse Fourier transformed back to the image domain generating an estimated image $g_j(\vec{x})$ from the illumination condition. Using the captured image $c_j(\vec{x})$, only the amplitude of $g_j(\vec{x})$ is replaced with the amplitude of the captured image $c_j(\vec{x})$ maintaining the phase of $g_j(\vec{x})$. The resultant image $g'_j(\vec{x})$ is now Fourier transformed into the spatial frequency domain $G'_j(\vec{k})$

and the reconstruction spectrum $R_j(\vec{k})$ is updated using $G'_j(\vec{k})$ and becomes an input for the next reconstruction process of the next captured image. This entire iteration process is repeated for every capture conditions and repeated a few more loops until the reconstruction spectrum $R_n(\vec{k})$ converges into a final reconstruction result $R(\vec{k})$. This FPM reconstruction process is illustrated in Figure 2.4. As in the conventional phase retrieval algorithm, the updating method in FPM can also be varied as shown in Equation (2.7):

$$\text{Gerchberg – Saxton algorithm: } R_{n+1}(\vec{k}) = \begin{cases} G'_n(\vec{k}), & P(\vec{k} + \vec{k}_n) \neq 0 \\ R_n(\vec{k}), & P(\vec{k} + \vec{k}_n) = 0 \end{cases}$$

$$\text{Input – Output algorithm: } R_{n+1}(\vec{k}) = \begin{cases} R_n(\vec{k}), & P(\vec{k} + \vec{k}_n) \neq 0 \\ R_n(\vec{k}) - \beta \cdot G'_n(\vec{k}), & P(\vec{k} + \vec{k}_n) = 0 \end{cases}$$

$$\text{Output – Output algorithm: } R_{n+1}(\vec{k}) = \begin{cases} G'_n(\vec{k}), & P(\vec{k} + \vec{k}_n) \neq 0 \\ G'_n(\vec{k}) - \beta \cdot G'_n(\vec{k}), & P(\vec{k} + \vec{k}_n) = 0 \end{cases}$$

$$\text{Hybrid Input – Output algorithm: } R_{n+1}(\vec{k}) = \begin{cases} G'_n(\vec{k}), & P(\vec{k} + \vec{k}_n) \neq 0 \\ R_n(\vec{k}) - \beta \cdot G'_n(\vec{k}), & P(\vec{k} + \vec{k}_n) = 0 \end{cases}$$

(2.7)

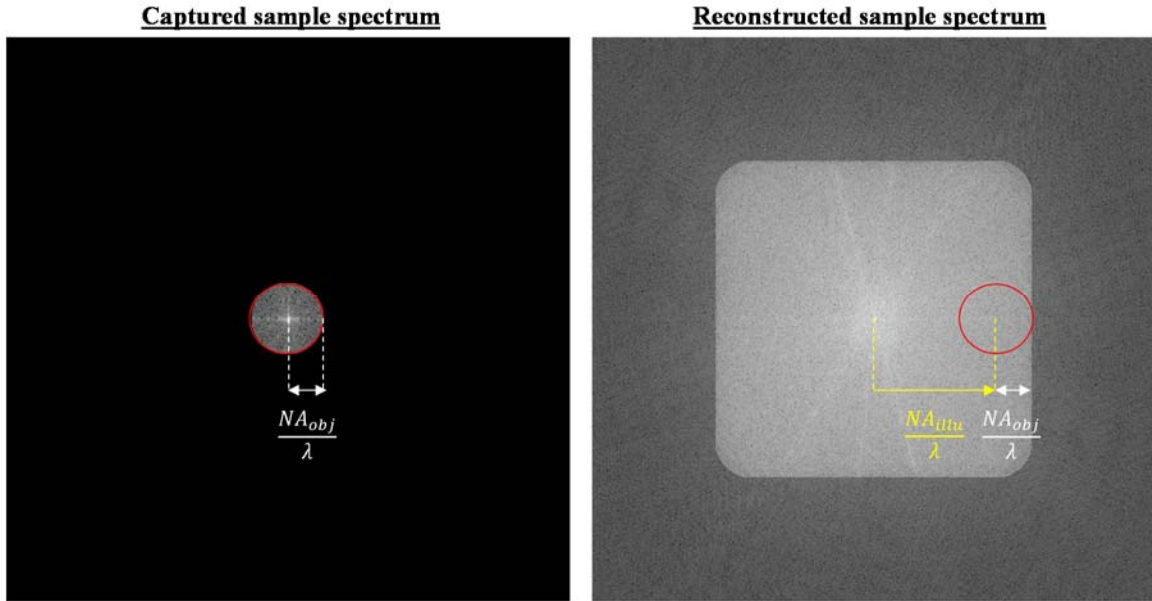
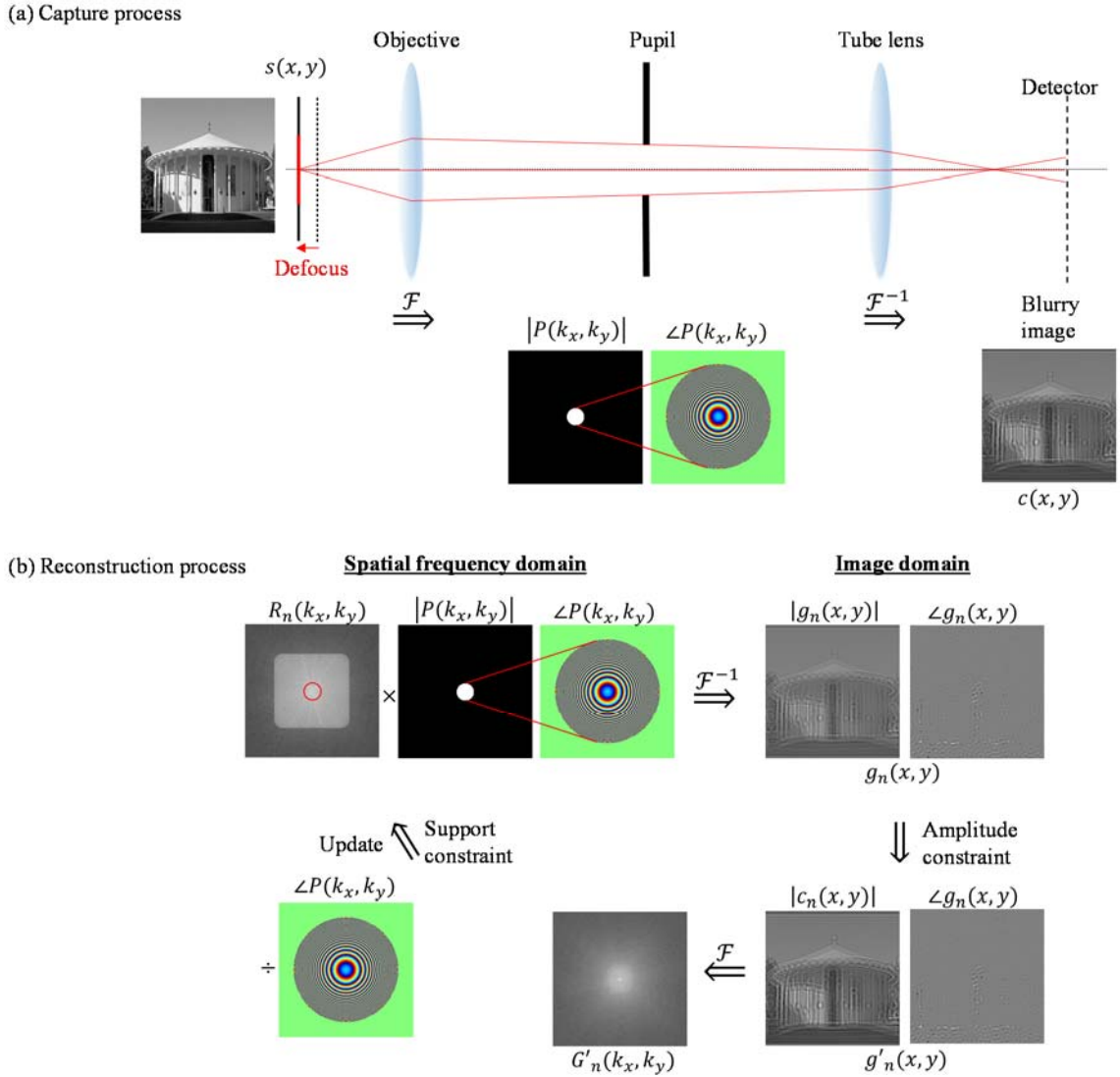


Figure 2.5: FPM image resolution improvement.

2.3 Image space-bandwidth product improvement

One of the most important advantages of Fourier ptychography is the ability to improve the resolution of wide FOV captured images without mechanically scanning the sample, which enables designing of an imaging system with large space-bandwidth product (SBP). SBP is a metric which indicates the number of resolvable pixels in the FOV of an imaging system. The maximum resolvable spatial frequency of a coherent imaging system is determined by the cutoff frequency k_c which is a function of the NA of an objective lens. As shown in Figure 2.5, the original sample spectrum is filtered by a pupil function of radius $\frac{NA_{obj}}{\lambda}$. As a result, the spectral information of higher spatial frequency than k_c is lost during the image acquisition process, resulting in a low resolution captured image. In FPM, the sample spectral information from different captured images is stitched together in the spatial frequency domain which increases the effective size of the aperture. Due to this increased effective pupil size, the system resolution of FPM also increases along with the improved system SBP. The effective numerical aperture of an FPM system is specified as Equation (2.8) [15]:



$$NA_{FPM} = NA_{obj} + NA_{illu}, \quad (2.8)$$

where NA_{FPM} is the system NA of FPM, NA_{obj} is the NA of objective lens, $NA_{illu} = n_{illu} \cdot \sin \theta_{max}$, where n_{illu} is the refractive index of material between sample and light source, and θ_{max} is the maximum illumination angle.

2.4 Digital image refocusing

The final result of the FPM image reconstruction process is a complex valued electromagnetic field information of sample $r(\vec{x})$, which is the inverse Fourier transform of $R(\vec{k})$, so it is possible to propagate the measured waves on the spatial frequency domain and digitally refocus a defocused captured image during the image reconstruction process. Let's say the sample is dislocated from the objective focal plane by z_d . Due to the defocus, there exists a quadratic phase gradient of $e^{i\sqrt{(\frac{2\pi}{\lambda})^2 - k_x^2 - k_y^2}z_d}$ on the pupil function and the recorded image on the detector becomes blurry as shown in Figure 2.6 (a). Because the captured raw images during the image acquisition process are experiencing the same defocus phase gradient, we can propagate the captured waves back to the focal plane by removing the same phase gradient from the captured spectrum as shown in Figure 2.6 (b). Digital image refocusing is a very useful tool for increasing DOF of imaging system especially in a system where tight focusing of sample is difficult to attain.

2.5 Computational aberration correction

As explained in Section 1.3, any imaging system cannot be free of aberration and therefore the pupil function has phase information which indicates the characteristics of optical elements in the imaging system. Because the aberration has a form of phase distribution on the pupil, we can computationally correct the aberration of the imaging system by applying an inverse phase map during the reconstruction process like the way we did in digital refocusing. Let's assume that the pupil has an aberration phase map of $\angle P(\vec{k})$. Because the recorded raw images contain an additional phase of $\angle P(\vec{k})$ in the spatial spectrum, we can computationally correct the system aberration by removing the additional phase term at the update process of image reconstruction. For example, the aberration correction can be done as Equation (2.9) for the case of Gerchberg-Saxton algorithm.

$$R_{n+1}(\vec{k}) = \begin{cases} G'_n(\vec{k})/e^{i\angle P(\vec{k})}, & P(\vec{k} + \vec{k}_n) \neq 0 \\ R_n(\vec{k}), & P(\vec{k} + \vec{k}_n) = 0 \end{cases}. \quad (2.9)$$

However, the aberration of an imaging system is usually an unknown parameter, and it needs to be characterized in order to be used in the reconstruction process. There are several methods to characterize the Zernike aberrations [16, 17]; however, it is time consuming to

characterize the spatially varying aberrations across the wide FOV of system. Furthermore, even though it has been characterized, it is highly sensitive to the minor changes in conditions between the sample and detector. As a result, it is desirable to computationally characterize the aberration phase map during the image reconstruction process on the fly.

Embedded pupil function recovery (EPRY) is an image reconstruction method which recovers both the sample spatial spectrum and the pupil function of the imaging system simultaneously [18]. Based on a gradient-descent-based update algorithm, EPRY makes a change in the updating process as shown in Equation (2.10).

EPRY spectrum update:

$$R_{n+1}(\vec{k}) = \begin{cases} R_n(\vec{k}) + \alpha \frac{P_n^*(\vec{k} + \vec{k}_n)}{|P_n(\vec{k} + \vec{k}_n)|_{max}^2} [G_n'(\vec{k} + \vec{k}_n) - G_n(\vec{k} + \vec{k}_n)], & P(\vec{k} + \vec{k}_n) \neq 0 \\ R_n(\vec{k}), & P(\vec{k} + \vec{k}_n) = 0 \end{cases}$$

EPRY pupil update:

$$P_{n+1}(\vec{k}) = P_n(\vec{k}) + \beta \frac{R_n^*(\vec{k} - \vec{k}_n)}{|S_n(\vec{k} - \vec{k}_n)|_{max}^2} [G_n'(\vec{k}) - G_n(\vec{k})], \quad (2.10)$$

where α and β are constants which adjust the step size of the update for spectrum and pupil function, respectively. Normally constant value $\alpha = \beta = 1$ is used for the update, and it has been reported that the reconstruction speed and image quality can be improved by gradually reducing the step size by the number of iteration increases [19].

EMSIGHT: INCUBATOR EMBEDDED CELL CULTURE IMAGING SYSTEM

Multi-day tracking of cells in culture systems can provide valuable information in bioscience experiments. In this chapter, we report the development of a cell culture imaging system, named EmSight, which incorporates multiple compact Fourier ptychographic microscopes with a standard multiwell imaging plate. The system is housed in an incubator and presently incorporates six microscopes. By using the same low magnification objective lenses as the objective and the tube lens, the EmSight is configured as a 1:1 imaging system, providing large field-of-view (FOV) imaging onto a low-cost CMOS imaging sensor. The EmSight improves the image resolution by capturing a series of images of the sample at varying illumination angles; the instrument reconstructs a higher-resolution image by using the iterative Fourier ptychographic algorithm. In addition to providing high-resolution brightfield and phase imaging, the EmSight is also capable of fluorescence imaging at the native resolution of the objectives. We characterized the system using a phase Siemens star target, and show four-fold improved coherent resolution (synthetic NA of 0.42) and a depth of field of 0.2 mm. To conduct live, long-term dopaminergic neuron imaging, we cultured ventral midbrain from mice driving eGFP from the tyrosine hydroxylase promoter. The EmSight system tracks movements of dopaminergic neurons over a 21 day period.

3.1 Introduction

Live cell imaging is widely used in various bioscience experiments for a better understanding of dynamic cellular behaviors such as migration [20], division [21, 22], differentiation [23], interaction with the environment [24], and organelle-level events [25]. In the most common way to perform live cell imaging, one builds a specialized incubation and imaging chamber onto a conventional microscope, and one images the cultured cells directly on the microscope stage [26]. Recent advances with this method include robotic well plate transport systems [27] to increase throughput and the implementation of

sufficiently compact and robust systems that can reside within an incubator [28]. Throughput of such systems is limited by the microscope itself. The number of resolvable pixels, characterized by the space-bandwidth product (SBP) [29], accessible through the microscope is limited at present (typically about 10 megapixels [30]). This constrains the rate of image acquisition or throughput that one can achieve.

Over the last few years, several new microscopy methods were developed with the purpose of overcoming the SBP limit of the conventional microscope. On-chip microscopes have demonstrated successful high resolution and large field-of-view (FOV) imaging of the cell cultures from within the incubator in the brightfield mode [31, 32] and the fluorescence mode [33]. However, the on-chip microscopes have an inherent problem: cells need to be grown on top of the imaging sensor. This is a marked departure from the conventional cell culture workflow and therefore the technology has not found major use. Other lensless imaging methods, such as digital in-line holography [34-36] and fiber-optic lensless imaging [37, 38], can work without this restriction, but they can provide high imaging SBP either in the brightfield mode or fluorescence mode, and they are not compatible with an in-vitro live cell imaging of well plate format.

Fourier ptychographic microscopy (FPM), another recently developed microscopy method, can overcome the SBP limit of conventional microscopes [9, 15, 18, 39-43]. The sample is illuminated by a series of LED sources in an array, thus providing a series of illumination directions. The images are combined in the spatial frequency domain using the Fourier ptychographic reconstruction algorithm, and a higher resolution image is rendered without sacrificing the FOV. Several aspects suggest that a FPM based cell culture imaging method would be an appropriate technology fit for high throughput cell culture imaging. First, by using low magnification objective lenses and improving the image resolution through FPM processing, we can obtain large FOV imaging of cell cultures at improved resolution. Second, the digital refocusing [9] capability associated with FPM processing can allow post-processing and correct defocus problems associated with cell culture imaging. This is a marked benefit, as the user can retain and analyze images that might be rejected with conventional imaging techniques. In addition, this

eliminates the need for mechanical auto-focusing solutions and simplifies the imaging system. Third, the imaging system would still be capable of collecting fluorescence images, albeit at the native resolution of the imaging system. Fourth, the configuration of the imaging system can be simple. A recent research study showed the possibility of building a compact Fourier ptychographic microscope using a cellphone lens, FPscope [44]. Fifth, we expect that a well-designed FPM-based system can be made cost-effectively and compactly to provide simultaneous imaging capability through multiple imaging units. This ability to perform parallel imaging can boost the effective system SBP by a factor equal to the number of parallel units.

This chapter reports an incubator embedded cell culture imaging system, termed EmSight, which employs the FPM for high resolution bright field imaging along with mid-resolution fluorescence imaging functionality. By configuring a 1:1 imaging system using two identical inexpensive objective lenses, the EmSight reduced the size of one imaging system to allow spacing on 30 mm centers, less than the spacing of a 6-well ANSI-standard plate. This allowed us to assign a compact Fourier ptychographic microscope to each well of a 6-well plate, removing the necessity of any mechanical movement for the well plate imaging.

In Section 3.2, we describe the system configuration of the EmSight and discuss its imaging principle. In Section 3.3, we explain the method we used for positioning and calibrating each EmSight inside an incubator to the LED matrix attached on the top shelf. In Section 3.4, we characterize the system using a phase Siemens star target and fluorescent microbeads, and report our culture imaging demonstration. In Section 3.5, we show experimental results from longitudinal live cell imaging experiments of dopaminergic and other neurons in mouse ventral midbrain cultures. And in Section 3.6, EmSight for dual channel fluorescence imaging is introduced. Finally, we summarize the results and discuss future directions and possible applications of the system.

3.2 System configuration

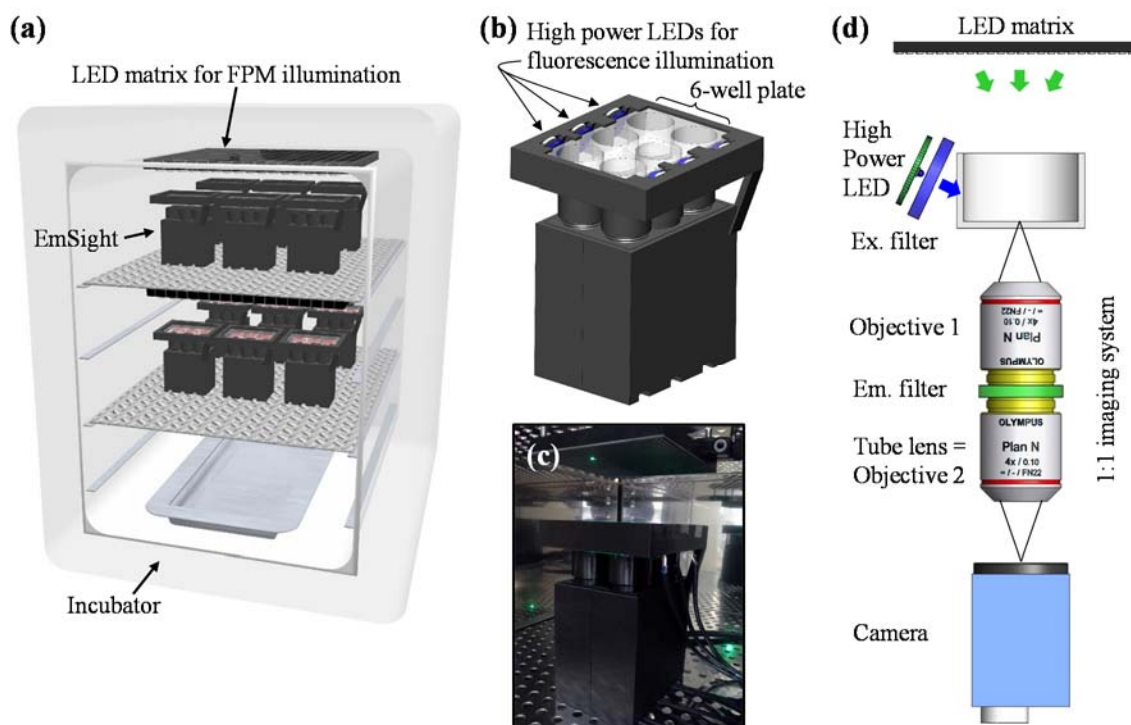


Figure 3.1: System configuration and imaging method of the EmSight. (a) Conceptual design of the EmSight system, attached to two adjacent shelves in an incubator. An LED matrix is attached to the bottom surface of the upper shelf for the FPM illumination, and EmSight modules are attached on the next shelf for the cell culture imaging. (b) The EmSight is designed for the 6-well plate format. Six units of the same 1:1 imaging system shown in (d) are built into an EmSight and a 6-well ANSI standard plate is loaded on top of the EmSight. Six high power LEDs and excitation filters are installed into the side of the plate holders, providing fluorescence illumination. (c) The EmSight prototype. The size of the EmSight is 125 mm (W) \times 133 mm (L) \times 170 mm(H) including a 6-well plate and a high power LED module. (d) EmSight uses the identical objective lenses for the objective and the tube lens, configuring a 1:1 imaging system. The LED matrix turns on one by one sequentially for the FPM illumination, and high power LEDs provide the fluorescence excitation.

EmSight is a compact imaging system designed for live-cell imaging within standard biological incubators, usually within a volume of 200 liters. Incubators have several horizontal shelves which can hold plates and flasks. The system utilizes two adjacent shelves, 250 mm apart. We attach the LED matrix (32 \times 32 LEDs, 4 mm pitch) for FPM

illumination to the bottom surface of the upper shelf, as shown in Figure 3.1 (a). With this configuration, each LED device in the matrix can be shared for FPM illumination by several imaging units, which reduces the effective footprint of the imaging unit, making more parallel experiments possible in the limited culture volume inside the incubator. This configuration also frees up the space between the well plate and the LED matrix, which gives us enough space for easy access to the well plate on the EmSight and eliminates the possibility of unnecessary light reflections from additional surfaces. As shown in Figure 3.1 (b), at present the EmSight is designed for live cell imaging in the 6-well plate format. Six identical imaging units are arranged in an EmSight body in order to image all wells in a 6-well plate which is loaded on top of the EmSight body. For the fluorescence illumination, high-power LEDs and excitation filters are at the horizontal edge of the plate, illuminating the imaged region directly from the side of the wells without blocking the light path from the LED matrix. In order to eliminate the possible background noise such as light reflection from surfaces and unexpected excitation of green LEDs in the LED matrix, the high power blue LEDs have openings only to the sample positions by blocking other straying light paths. The assembled EmSight prototype is shown in Figure 3.1 (c). The size of the EmSight is 125 mm (W) x 133 mm (L) x 170 mm (H). The casing is 3D printed using a Makerbot 3D printer.

The imaging unit inside the EmSight consists of a pair of the same objectives which are configured to perform 1:1 imaging in infinity corrected system. The configuration is shown in Figure 3.1 (d). We use Olympus 4X/NA0.1 objective lenses in our prototype. The EmSight system uses 5 MP CMOS cameras (Imaging Source, DMK 23UP031, Pixel size: 2.2 μm) as detectors and the sensor size is matched to the field size of the imaging system in order to maximize the system FOV which is defined as Equation (1.8). Furthermore, we match the raw resolution of the objective lens with the pixel size limited resolution from the camera in the 1:1 imaging system, which enables full usage of native NA of objective lens both in FPM imaging and fluorescence imaging. During operation, we capture 169 images of the sample per well, each with a different LED illumination angle, and stitch the data together in the spatial frequency domain using the Fourier ptychographic algorithm [9] to render a higher-

resolution brightfield image. For each well, we first determine an LED that is centered on the well by checking the brightness of images from different LED positions without samples. Then we calibrate the positional error between the LEDs and EmSight using the vignette image from the center LED. After calibration of the positional error, a sample well plate is loaded and 13×13 LEDs around each center LED are chosen for imaging each well sequentially. To perform fluorescence imaging, we insert an emission filter (540 nm/50 nm) between each objective and its tube lens, and illuminate the sample using a high power LED (center wavelength: 470 nm) and an excitation filter (475 nm/50 nm). These filter sets and high power LED can be changed accordingly for each fluorophore in use. By choosing the brightfield illumination wavelength to fall within the passband of the emission filter ($> 93\%$ transmission), we can collect both brightfield and fluorescence images without losing photons while the filters remain in place. Custom built Matlab scripts control the operation of LED matrix and high power LEDs, and synchronously capture images from the cameras. After a 6-well plate is loaded on the EmSight, the incubator is closed during the experiment and data from the camera is saved at the pre-specified time points into a desktop computer which is located outside of the incubator. Current prototype of EmSight uses 14 cables (2 for a LED matrix, 6 for high power LEDs, and 6 for cameras) for power and communication with a computer. The exposure time for bright field and fluorescence imaging depends on the sample in the experiment. In our neuron imaging experiment, we imaged each sample with three different exposure times (8 ms, 64 ms, and 500 ms) and combined them into a HDR (High Dynamic Range) raw image, and we captured fluorescence signal from the sample with 1 sec exposure time. The total imaging time for a single frame data set (3×169 raw FPM images + 1 fluorescence image) is 5 min, and an additional 1 min is required for transmitting and saving 700 MB of the raw data.

3.3 LED matrix and EmSight positional calibration

Fourier ptychographic algorithm requires accurate illumination direction information from different LEDs in order to stitch the raw images into correct locations in the spatial frequency domain. Because the main body of the EmSight is separated from the LED matrix, we need to calibrate the LED position relative to the sensor camera for the accurate

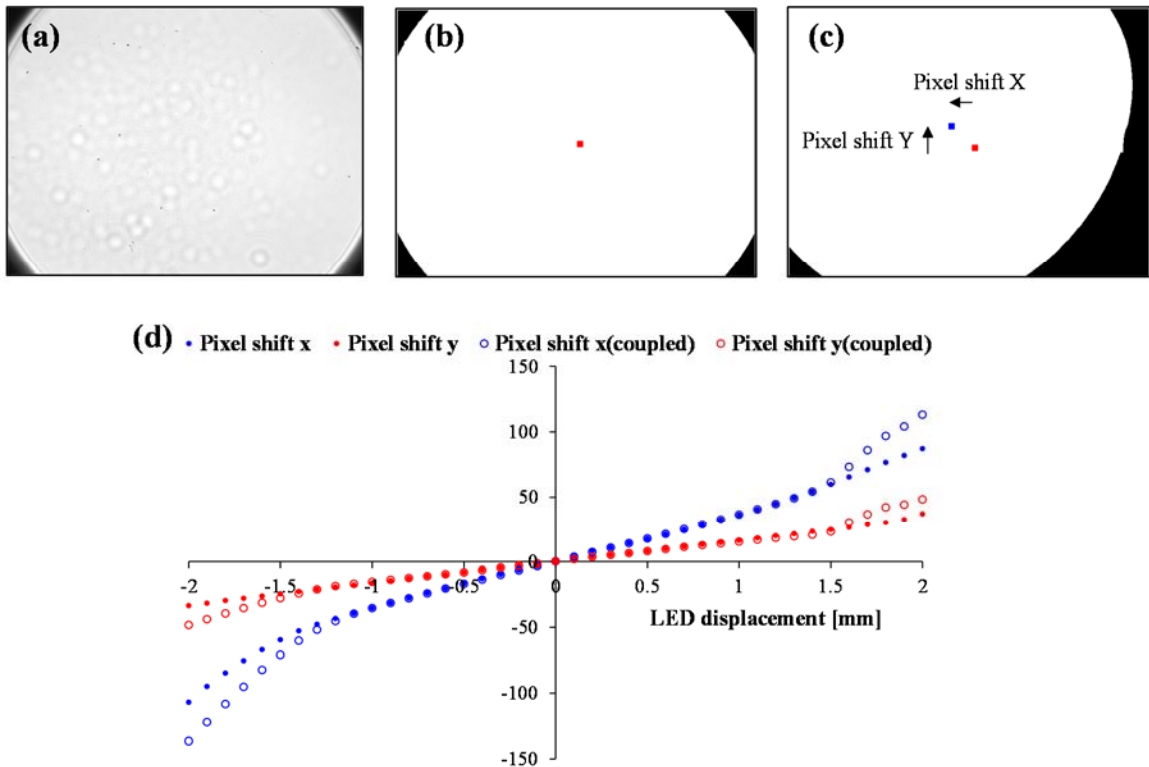


Figure 3.2: LED position calibration. (a) Vignette image from the center LED. (b) Black and White (BW) image of well aligned vignette image. Center of BW image (blue dot) is located at the center of imaging sensor (red dot) (c) Black and white image of misaligned vignette image. Center of vignette image (blue dot) is shifted from the center of imaging sensor (red dot) (d) Lookup table for the LED displacement to the center of imaging sensor.

reconstruction. We use a vignette image from the center LED illumination as shown in Figure 3.2 (a) for this purpose. In order to find the center of the vignette image, we convert the vignette image into a black and white (BW) image. When the LED position is well aligned with the camera, the center of BW image (blue dot) is located at the center of imaging sensor (red dot) as shown in Figure 3.2 (b). When there is a misalignment between the LED and the camera, the center of BW image (blue dot) is shifted from the center of the imaging sensor (red dot) as shown in Figure 3.2 (c). We use the shift of the center of vignette image as an indicator of LED displacement and make a lookup table by moving LED matrix relative to the camera as shown in Figure 3.2 (d). Blue closed circle is the

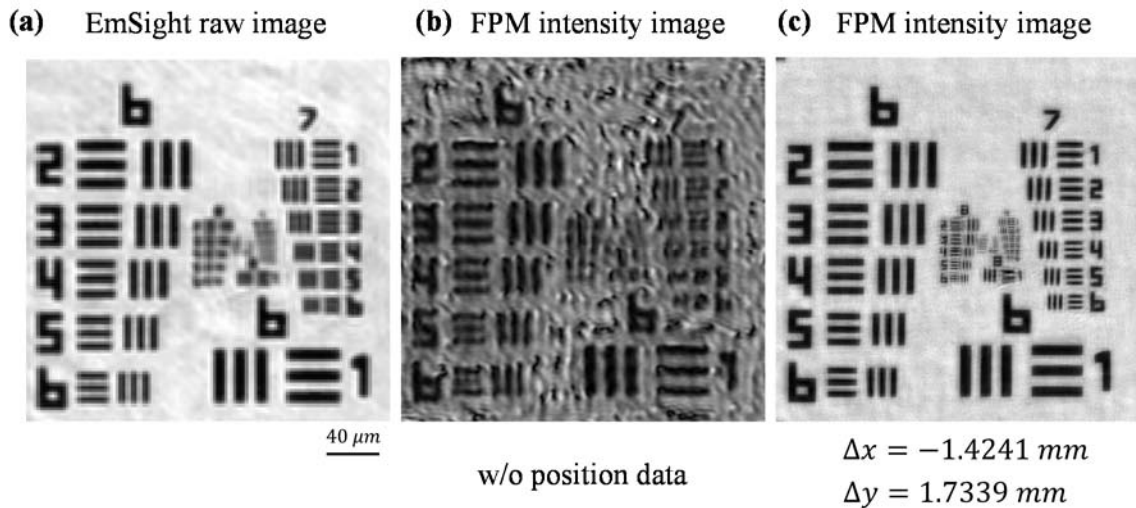


Figure 3.3: Effect of LED position misalignment. The LED matrix is displaced by $\Delta x = -1.28 \text{ mm}$ and $\Delta y = 1.79 \text{ mm}$. (a) Raw resolution image of the USAF resolution target. (b) FPM reconstruction intensity image without positional misalignment correction. (c) FPM reconstruction intensity image with positional misalignment correction. From the LED position calibration, the calculated misalignment from the lookup table ($\Delta x = -1.4241 \text{ mm}$ and $\Delta y = 1.7339 \text{ mm}$) is used when calculating angle of illumination for each image acquisition.

number of pixel shift when LED moved x direction, and red closed circle is the number of pixel shift when LED moved y direction. In order to consider the shift in both directions, the number of pixel shifts in x and y are measured as the LED is translated in diagonal direction (open circles). After loading an EmSight into the incubator, we measure the number of pixel shifts of the vignette in x and y directions and find the LED displacement using the lookup table. The curve of open circles in lookup table is used only when the both of the resultant displacement in x and y directions are more than 1 mm. In Figure 3.3, the FPM image reconstruction results with and without the positional error calibration are compared. For arbitrary misalignment, the LED matrix is displaced by $\Delta x = -1.28 \text{ mm}$ and $\Delta y = 1.79 \text{ mm}$ relative to the image sensor. The USAF resolution target is used as a sample on the misaligned system and raw images are captured from 169 different illumination directions. A raw image from direct illumination is shown in Figure 3.3 (a). The line segments from Group 7 and Element 3 (line pitch: $6.2 \mu\text{m}$) are resolved from the

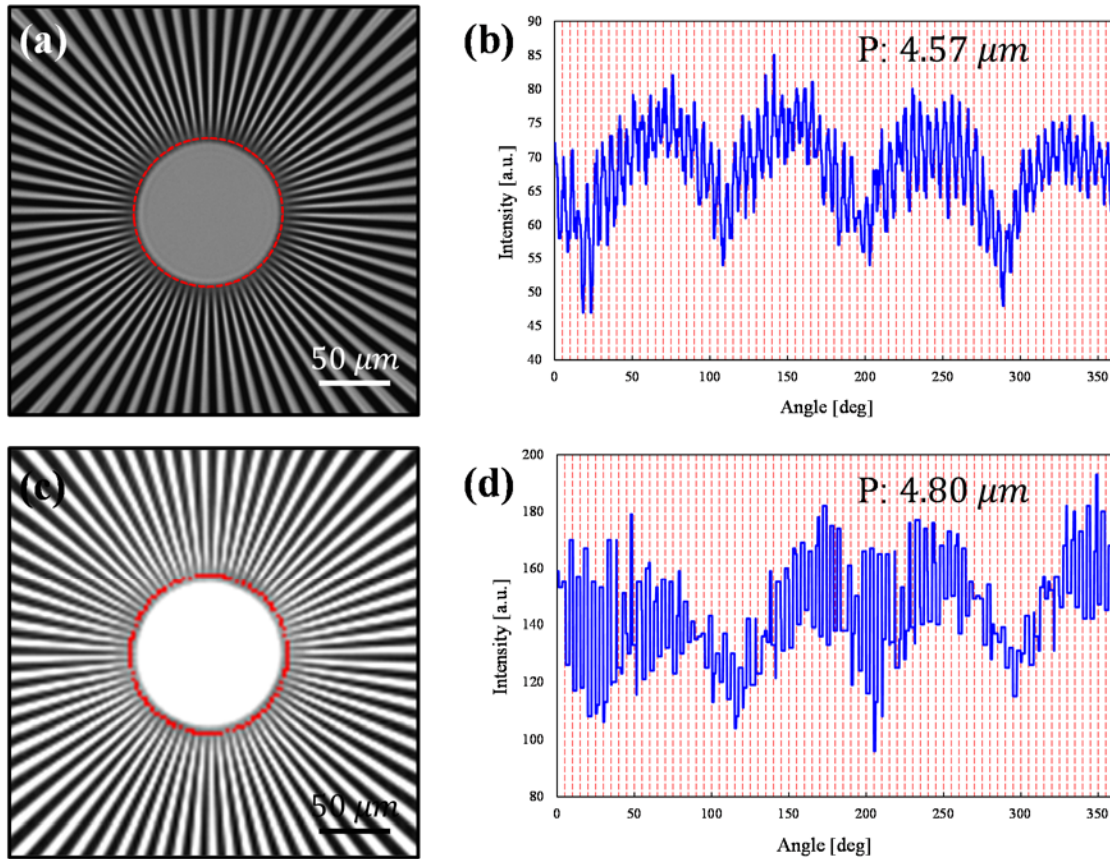


Figure 3.4: Raw image resolution of EmSight. Sample is Siemens star intensity target. (a) Conventional microscope image using a 4X/ NA0.1 objective lens. (b) Profile of the smallest resolved lines through a red line indicated in (a). (c) Raw image from EmSight. (d) Profile of the smallest resolved lines through a red line indicated in (c).

raw image. When wrong information about illumination angles is used without having positional error correction, the FPM reconstruction process is not successful and generates lots of noises in the image as shown in Figure 3.3 (b). On the other hand, when the positional error is calculated from the lookup table and applied into the FPM reconstruction process, all spectral information from different measurement are recombined correctly and smaller line segments from Group 9 and Element 3 (line pitch: $1.6 \mu m$) are resolved, indicating 4 times resolution improvement as shown in Figure 3.3 (c).

3.4 System characterization

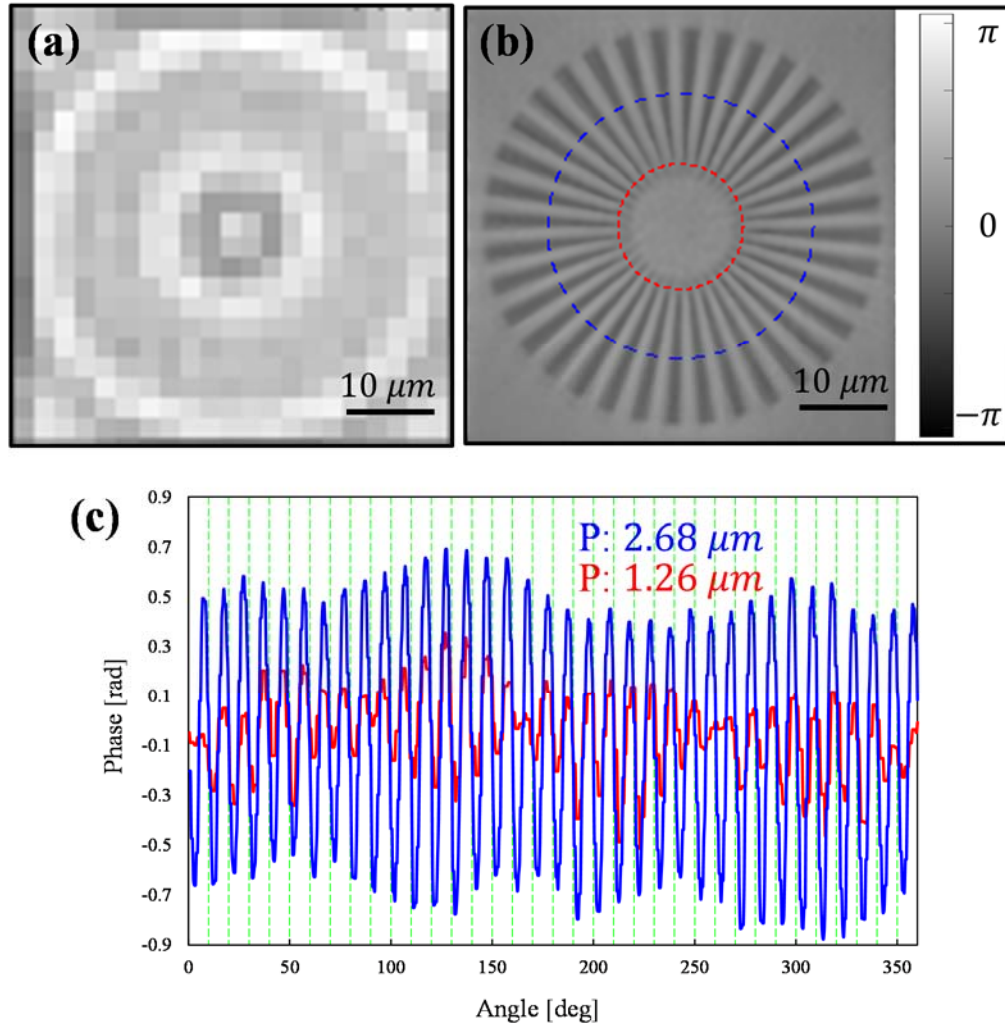


Figure 3.5: FPM reconstructed image resolution of EmSight. Sample is Siemens star phase target. (a) Raw image from EmSight. (b) FPM reconstructed phase image from EmSight. (c) Profile of the resolved lines through red (line pitch: $1.26\ \mu\text{m}$) and blue lines (line pitch: $2.68\ \mu\text{m}$) indicated in (b).

In order to characterize the resolution of the EmSight, we used Siemens star targets and fluorescence beads as samples following a new coherent imaging resolution standard described in [45]. Figure 3.4 (a) shows a microscope image of a Siemens star intensity target (Edmund optics, #58833, smallest periodicity: $4.37\ \mu\text{m}$) taken with a 4X/NA 0.1 objective with planar illumination, and Figure 3.4 (c) shows a raw image of the same sample from the EmSight with the center LED illumination. We define the resolution of

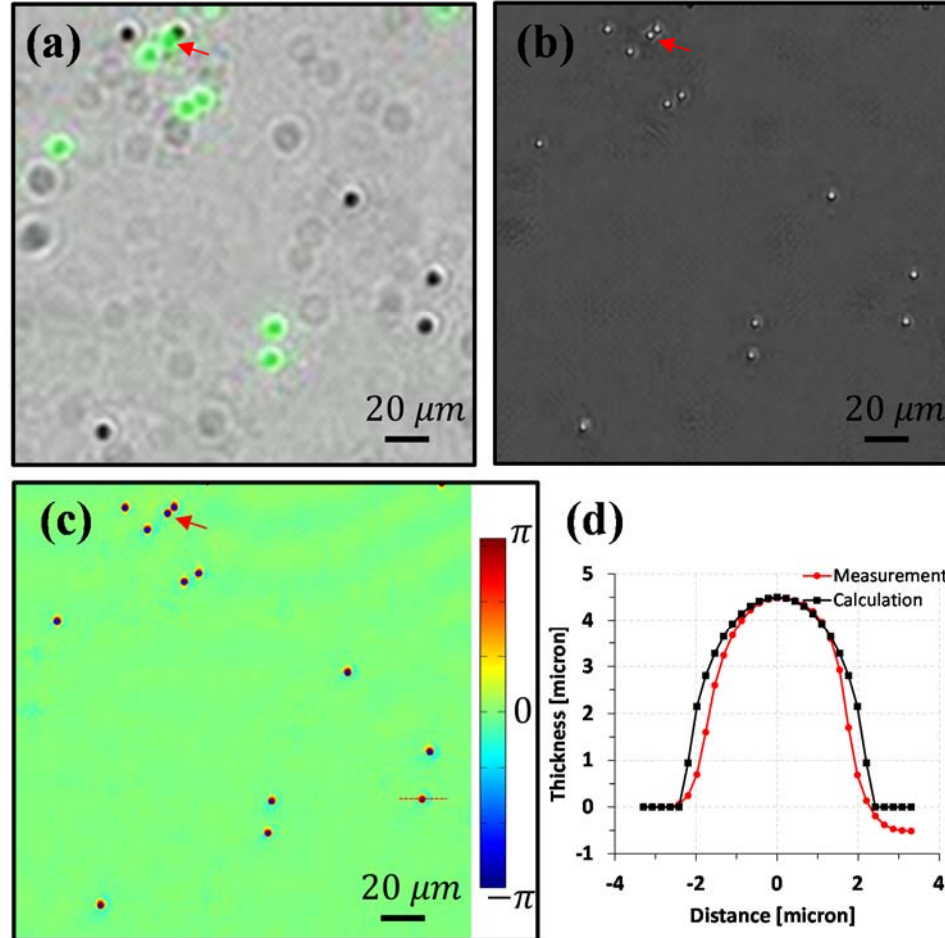


Figure 3.6: Multi-modal imaging of EmSight. Sample is mixture of $4.5\ \mu\text{m}$ green fluorescence beads and non-fluorescent beads. (a) Overlay image of the raw bright field image and the fluorescence image (Green color). (b) FPM reconstructed intensity image from EmSight. (c) FPM reconstructed phase image from EmSight. (d) Thickness profile of a bead, based on the reconstructed phase through a line indicated in (c).

the coherent imaging system as the smallest periodicity of unambiguously resolved for all spokes in the Siemens star target. Figure 3.4 (b) and (d) show the profile of amplitude values along a red line indicated in Figure 3.4 (a) and (b), respectively. The smallest resolvable periodicity of the objective lens is $4.57\ \mu\text{m}$ and the smallest resolvable periodicity of the EmSight native imaging capability (without applying FPM processing) is $4.80\ \mu\text{m}$, which indicates that the EmSight is almost fully using the NA provided by the

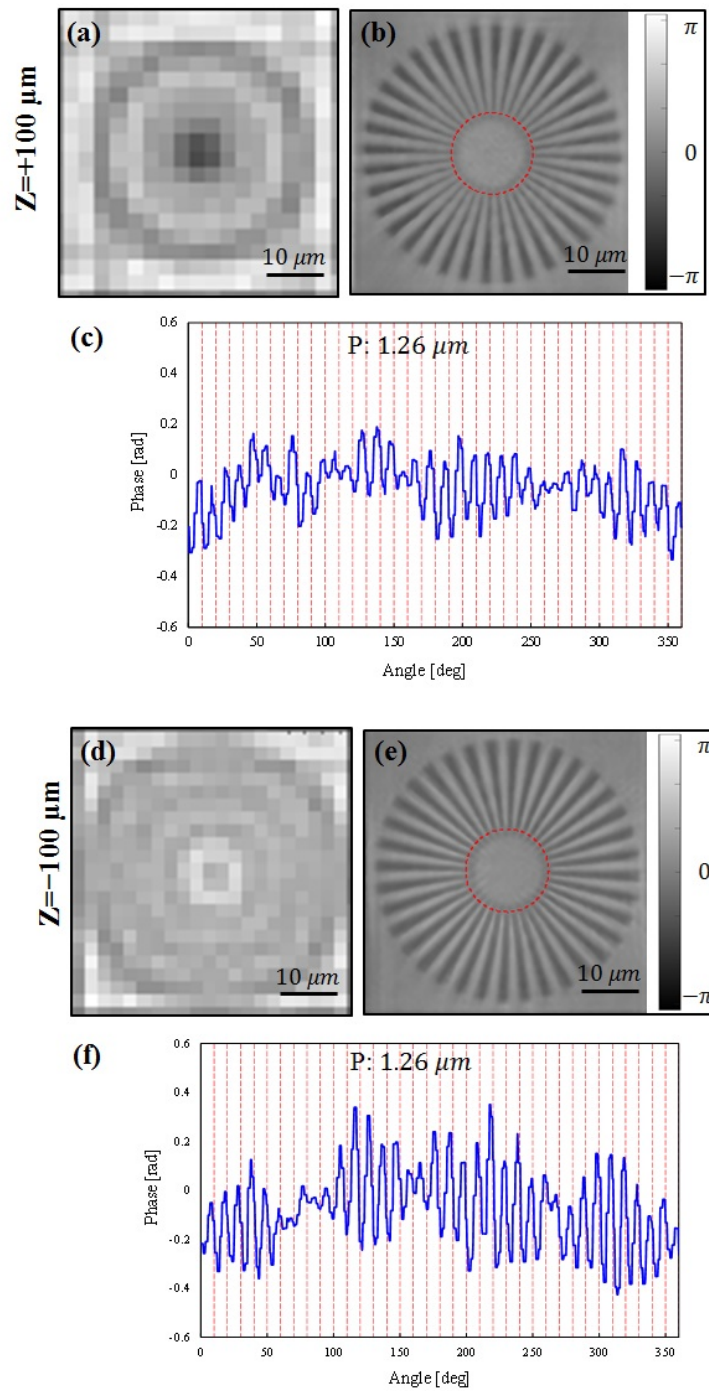


Figure 3.7: Digital refocusing of the EmSight. (a-c) $Z = +100 \mu\text{m}$, and (d-f) $Z = -100 \mu\text{m}$ defocused Siemens star phase target. (a and d) Raw image. (b and e) Digitally refocused FPM phase image. (c and f) Line profile of the smallest resolved lines along a red line indicated in (b) and (e), respectively.

objective lens in the 1:1 imaging configuration. Because the main sample of the EmSight

is mostly transparent live cells, we fabricated a Siemens star phase sample by etching a slide glass using FIB (Focused Ion Beam). The largest and smallest periodicity is $4\ \mu\text{m}$ and $1\ \mu\text{m}$, respectively, and the depth of the etched surface is about $230\ \text{nm}$. The raw intensity image and the FPM reconstructed phase image of the sample are shown in Figure 3.5 (a) and (b), respectively. In Figure 3.5 (c), fully resolved line profile (blue line) and the smallest resolved line profile (red line) are shown. By imaging the sample from 169 different LED directions and combining the low resolution images using Fourier ptychographic algorithm (synthetic NA of 0.42), the resolution of the system is increased by about 4 times, resolving all the spokes of periodicity of $1.26\ \mu\text{m}$.

Next we used a mixture of green fluorescence beads and non-fluorescent beads ($4.5\ \mu\text{m}$ diameter) to check the fluorescence and FPM phase imaging performance. A raw bright field image overlaid with a fluorescence image (green color) is shown in Figure 3.6 (a). We expect EmSight users to use the fluorescence images to identify targets labeled by, or expressing specific fluorophores, and FPM reconstructed higher resolution images to compensate for the diffraction-limited fluorescence image of the targets. For simplicity, we did not apply resolution improving methods to the fluorescence imaging in the current EmSight design, however, we note that the resolution of the fluorescence images may be enhanced by adopting special illumination methods such as patterned illumination or scattering illumination [46] or aberration correcting methods [17] for those applications requiring higher-resolution fluorescence imaging. As shown in Figure 3.6 (a), the fluorescence beads are clearly distinguishable from the non-fluorescent beads by the fluorescence signal. Two beads that are attached to each other (labeled with red arrow) are resolved from the FPM reconstructed intensity (Figure 3.6 (b)) and phase (Figure 3.6 (c)) images, and the fluorescence image (Figure 3.6 (a)) gives us information on which bead is fluorescent amongst them.

A complex field that contains intensity and phase information of the sample can be rendered by the iterative Fourier ptychographic algorithm [39]. In order to verify the quantitative accuracy of the phase information, we converted the reconstructed phase information into the thickness of the bead using Equation (3.1):

$$T = \frac{\lambda}{2\pi} \cdot \frac{\Delta\phi}{\Delta n}, \quad (3.1)$$

where T is the thickness of the bead, λ is the wavelength of the light, $\Delta\phi$ is the phase relative to the background phase, and Δn is the refractive index difference between the sample and the background. In Figure 3.6, the polystyrene beads ($n=1.58$) are immersed in oil ($n=1.515$) and green LEDs (530 nm) are used for illumination. The converted line profile indicated in Figure 3.6 (c) is shown in Figure 3.6 (d). The measured curve closely matched the expected profile of an ideal sphere, which indicates the FPM reconstructed phase information of the EmSight is quantitatively accurate. We note that there are small asymmetries in the phase of some beads in Figure 3.6 (d). These small asymmetries can be attributed to the abrupt phase change of boundary between the bead and surrounding oil.

Digital refocusing is one of the most important features of the FPM and it is especially useful in live cell imaging, where multi-day or multi-week experiments can be vitiated by image defocus caused by system drifts and well plate misalignments. By introducing a quadratic defocus phase term into the support constraint in the spatial frequency domain, we can digitally refocus the defocused raw images during the FPM reconstruction [9]. In order to characterize the refocusing performance of the EmSight, we intentionally image a defocused Siemens star phase target and digitally refocused the image during the FPM reconstruction (see Figure 3.7). For the depth of field (DOF) test, we built the equivalent imaging system on the optics table and used a mechanical stage for making displacement of the sample from the detection system. For the refocusing of the defocused sample, we use the angular spectrum wave propagation method [47, 48]. By the discrete sampling of the camera and the Nyquist sampling theorem, there is a maximum distance that the angular spectrum method can be applied as in Equation (3.2):

$$z \leq \Delta u^{-1} \frac{\sqrt{\lambda^{-2} - u^2 - v^2}}{2u}, \quad z \leq \Delta v^{-1} \frac{\sqrt{\lambda^{-2} - u^2 - v^2}}{2v}, \quad (3.2)$$

where z is the distance of wave propagation, λ is wavelength of light, u and v are spatial frequencies in x and y directions, and Δu and Δv are sampling intervals in x and y

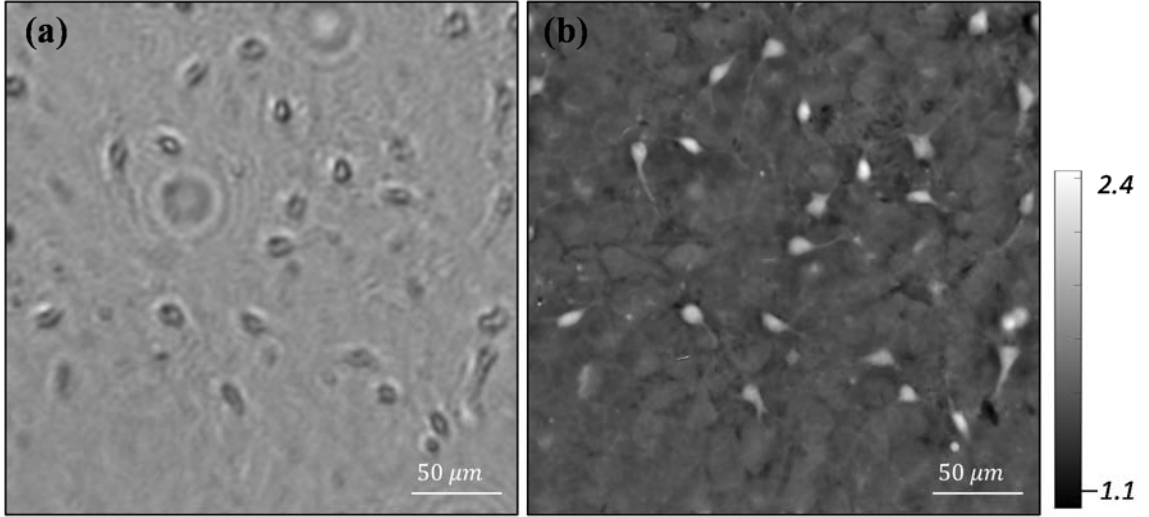


Figure 3.8: Digital image refocusing example. (a) A defocused mouse midbrain culture. (b) Digitally refocused FPM phase image.

directions. In our system, we matched the NA of objective lens with camera pixel size, and we used 128 pixel x 128 pixel for each tile of image reconstruction, and therefore the maximum distance is calculated as Equation (3.3):

$$\begin{aligned}
 z &\leq \Delta u^{-1} \cdot \frac{1}{2} \sqrt{\left(\frac{1}{\lambda \cdot u_{max}}\right)^2 - 2} \\
 &= 128 \times (2.2 \mu m) \cdot \frac{1}{2} \sqrt{\left(\frac{2 \times (2.2 \mu m)}{0.53 \mu m}\right)^2 - 2} \approx 1,150 \mu m. \quad (3.3)
 \end{aligned}$$

However, this is the theoretical maximum distance which the angular spectrum method can be applied without violating the Nyquist sampling theorem in the noise-free condition, and is not representing actual limit which resolution starts to deteriorate. In order to consider actual experimental condition, we experimentally measured DOF by finding the maximum sample displacement where the resolution of the image starts to deteriorate. As shown in Figure 3.7, the EmSight refocused the sample successfully without deteriorating resolution within the defocusing range of $\pm 100 \mu m$, which indicates that the DOF of the EmSight is

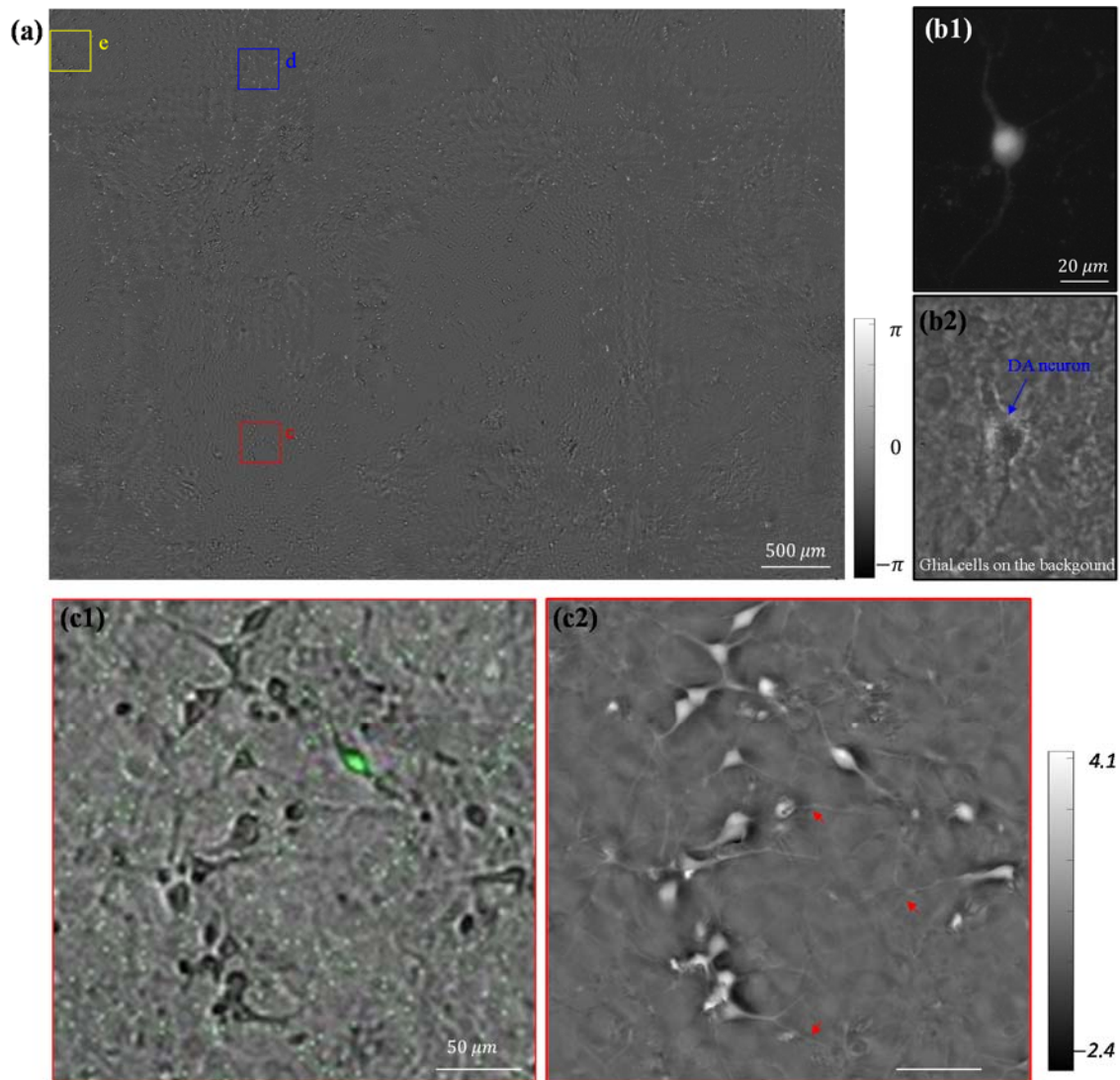


Figure 3.9: Large FOV imaging of the EmSight. The sample is mouse ventral midbrain cultures. (a) Full FOV FPM reconstructed phase image. The size of FOV is $5.7 \text{ mm} \times 4.3 \text{ mm}$. (b) Images of a dopaminergic neuron (DA neuron) from conventional microscope (20X / NA0.4). (b1) Fluorescence image, and (b2) phase contrast image. (c-e) Enlarged images at a distance of 1.8 mm, 2.2 mm, and 3.4 mm away from the center of the FOV, respectively.

about $200 \mu\text{m}$. As an example of digital refocusing on a biological sample, one of the defocused mouse neuron culture images and its refocused FPM reconstruction phase image

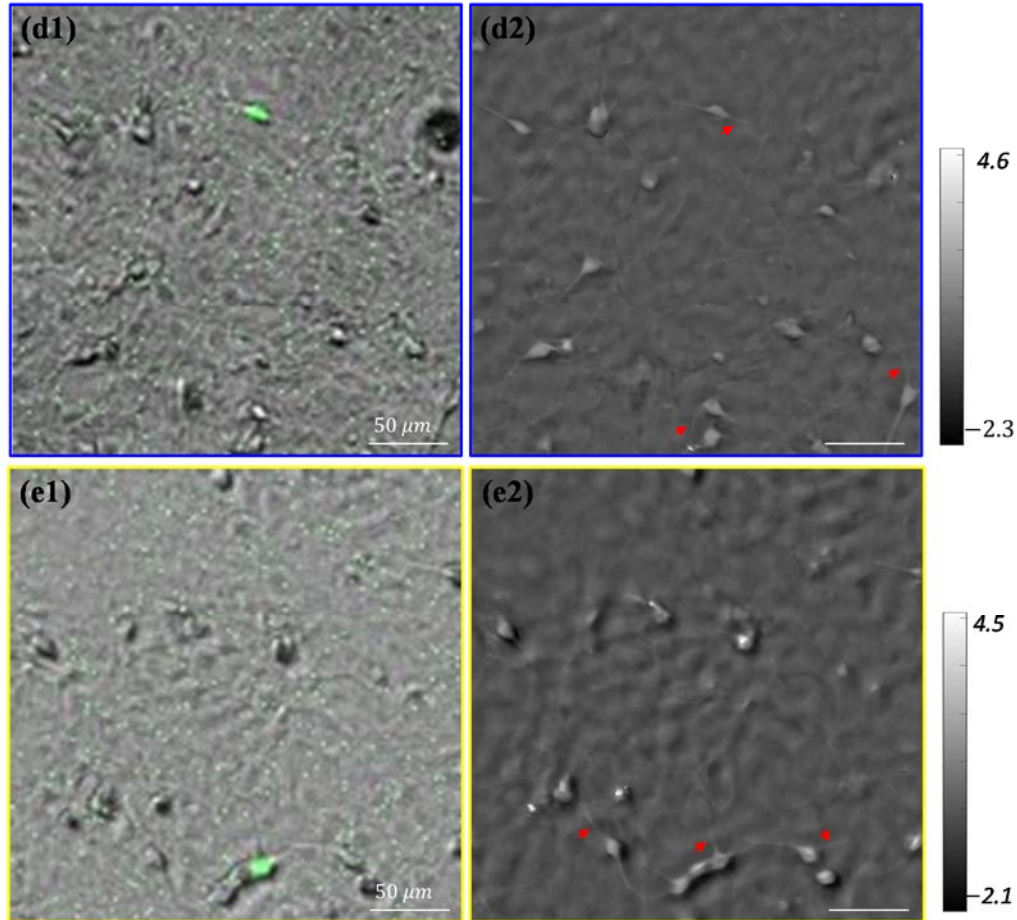
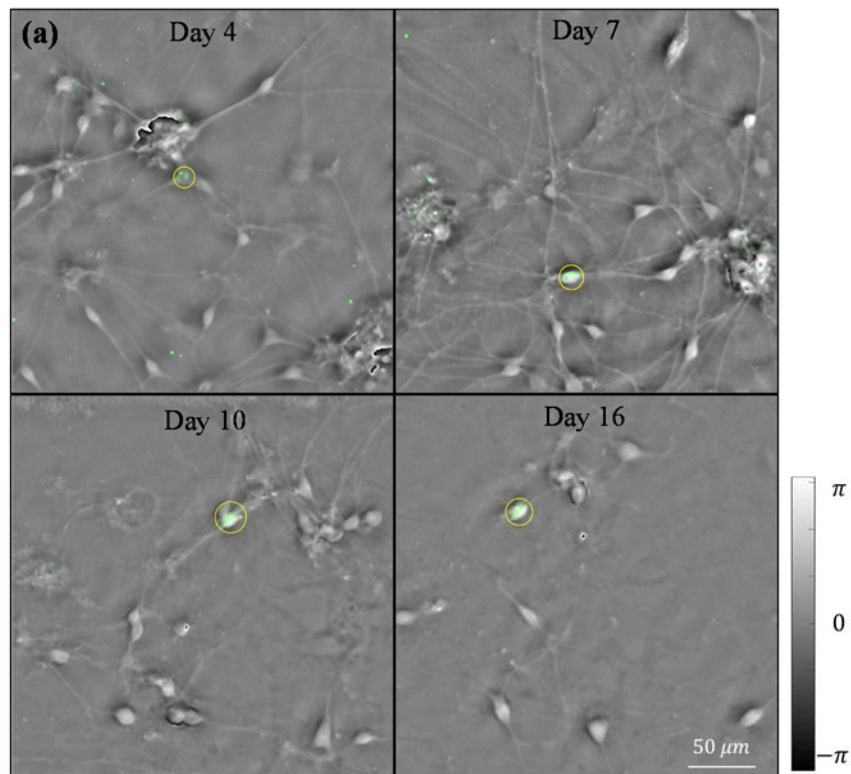


Figure 3.9 (*cont.*): (c1-e1) Raw images overlaid with fluorescence images (Green color). In this GENSAT strain, dopaminergic neurons produce the eGFP signal. (c2-e2) The reconstructed phase images. Neurites of the neuron which are not distinguished in the raw images are clearly visible in the reconstructed phase images (red arrows).

are shown in Figure 3.8. Blurry neurites of the neurons in the defocused image are clearly refocused in the FPM reconstructed image.

We also used the EmSight to image a mouse ventral midbrain culture sample in order to test the FOV of the system and to assess the fluorescence imaging capability of the system. The sample was fixed with paraformaldehyde (PFA) and immersed in phosphate buffered saline (PBS) for the imaging. The full FOV of one imaging unit of the EmSight is $5.7 \text{ mm} \times 4.3 \text{ mm}$, as shown in Figure 3.9 (a). This sample was originally seeded with



(b)

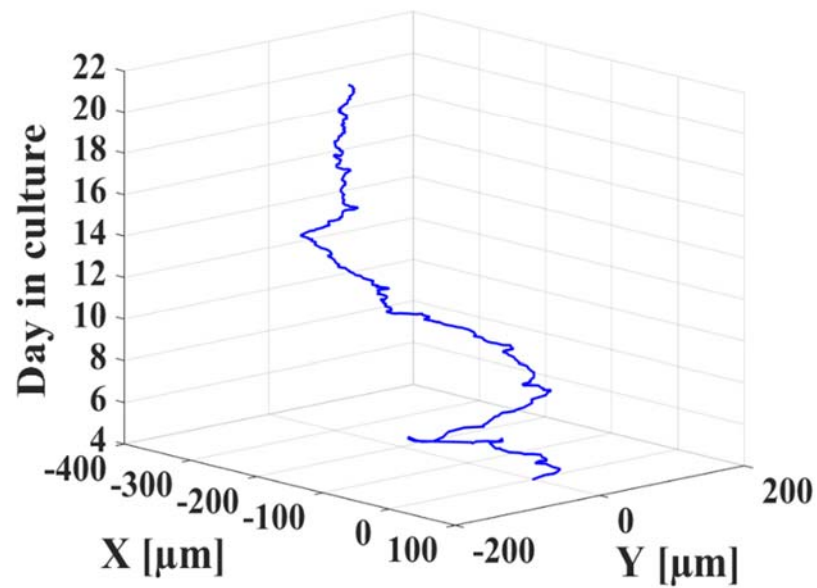


Figure 3.10: Time-lapse imaging of the mouse midbrain culture. (a) FPM phase images overlaid with fluorescence image (Green color) of a tracked dopaminergic neuron. (b) Positional trace of the dopaminergic neuron marked in (a).

dopaminergic (DA) neurons that were engineered to express eGFP. We were able to

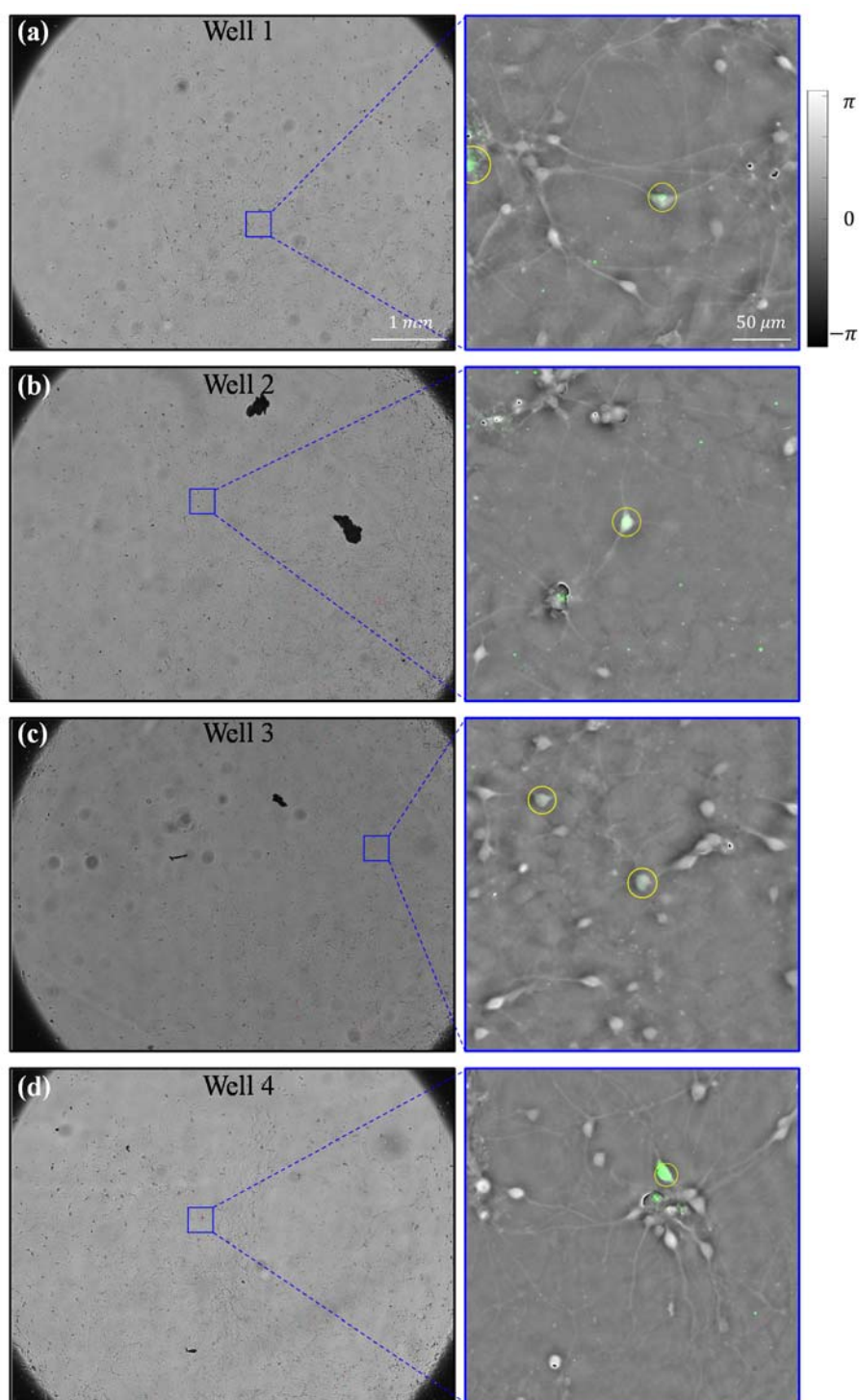


Figure 3.11: 6-well plate imaging of the mouse ventral midbrain culture. (a-f) Full FOV images and FPM phase images overlaid with fluorescence image (Green color) from Well 1 to Well 6, respectively (Culture day 7).

identify 15 DA neurons through the observed eGFP signals within the FOV shown in

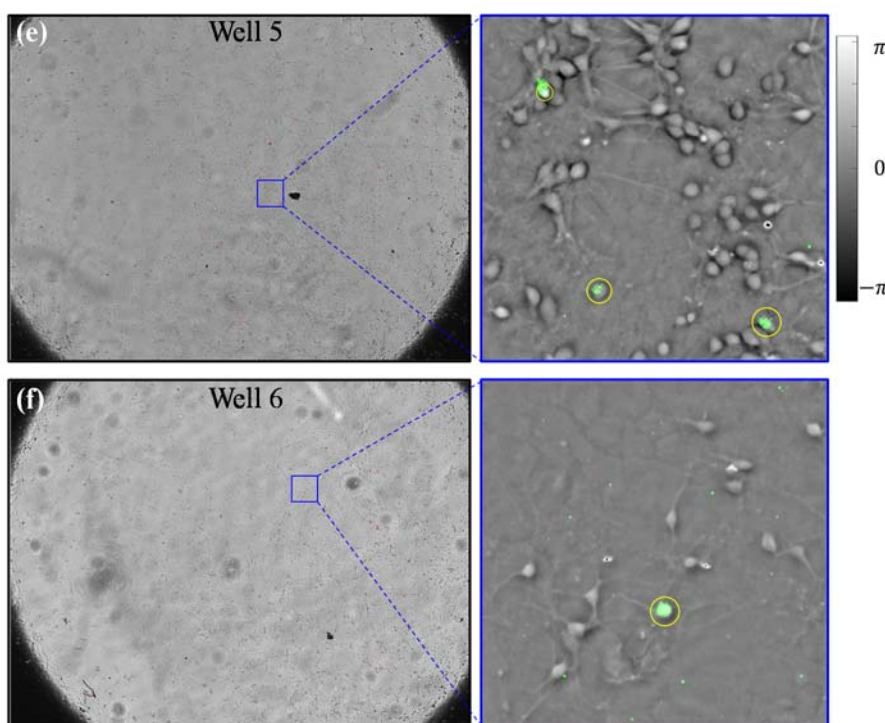


Figure 3.11 (*cont.*)

Figure 3.9 (a). Images from three representative DA neurons are shown in Figure 3.9 (c-e). The eGFP fluorescence signal intensity captured from the EmSight system is strong enough to be used to identify the target DA neurons, as shown in Figure 3.9 (c1-e1). Figure 3.9 (c2-e2) show the FPM reconstructed phase images at distances of 1.8 mm, 2.2 mm, and 3.4 mm from the center of the FOV, respectively. Neurites of the neuron which are not distinguished in the raw images are clearly visible in the reconstructed phase images as indicated in red arrows. For comparison, fluorescence image and Zernike phase contrast image of a dopaminergic neuron (DA neuron) are shown in Figure 3.9 (b) using 20X/NA0.4 objective lenses. We note that the neuron sample in our experiment is a primary mixed culture and the surface of the well plate is covered with glial cells. The unevenness of the background in Figure 3.9 (c2-e2) is the image of the glial cells. These glial cells can be seen in the Zernike Phase contrast image of Figure 3.9 (b2). Also dark halos surrounding some cell bodies in the phase images are attributable to the physical

changes the DH cells made to its immediate environment. The same halos (white in phase contrast) are observed in the phase contrast image as well.

3.5 Live cell culture imaging

To conduct live cell imaging using the EmSight system, we cultured ventral midbrain from the GENSAT tyrosine hydroxylase (TH)-eGFP strain [49], a BAC transgenic mice line driving eGFP from the TH promoter. The cultures were grown based on the procedure we have recently established for the long-term primary culture of mouse ventral midbrain neurons [50, 51]. Each of the neuron-glia ventral midbrain cultures consisted of a glial cell monolayer, DA neurons generating TH-eGFP, and other midbrain neurons. We employed the EmSight system to image and monitor the cultures over a 3-week period.

Our ventral midbrain cultures were obtained from embryonic day 14 mouse embryos which were extracted from timed pregnant mice using a standard method [52]. The glial cells and midbrain neurons were grown in a 6-well plate and the culture medium was exchanged at three-day intervals over the 3-week imaging period. The EmSight system captured images from each well at one hour intervals for the FPM imaging. Fluorescence imaging was conducted once per day for each well. Figure 3.10 (a) shows representative FPM phase images from the time-lapse imaging of a DA neuron and midbrain neurons. The tracked DA neuron is successfully identified using the eGFP fluorescence signal and marked with a yellow circle. By comparing each subsequent image, we choose a cell having minimum position and size change with a target cell of previous time frame as a target cell of current time frame. In our one hour period time-lapse imaging, this tracking method worked well for most of cells. For the time sequences cells were moving fast, we manually corrected the tracking error. We successfully tracked the target cell for the duration of the culture experiment, and Figure 3.10 (b) shows the positional trace of the tracked target cell. Images of the entire field of view and the reconstructed FPM phase images for each of the 6 wells at culture day 7 are shown in Figure 3.11.

The mouse ventral midbrain cultures used in the experiment were mixed primary cultures. During the 21-day culture experiment, actively dividing cells were found from

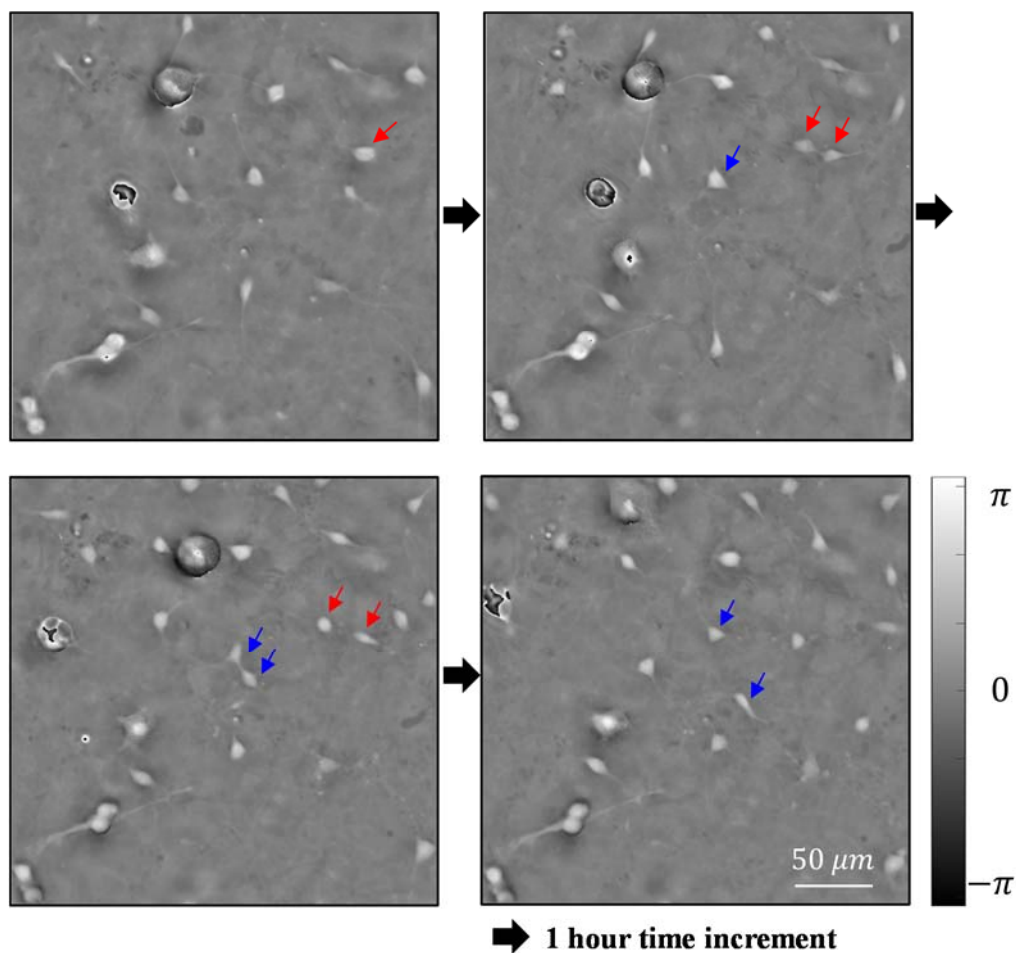


Figure 3.12: Time-lapse imaging of the dividing cells. Two mother cells marked in red and blue arrows divided into daughter cells.

the time-lapse images as shown in Figure 3.12. Two putative mother cells as indicated by the red and blue arrows divided into daughter cells. These cells began dividing on approximately day 14 of culture. Such cell divisions were observed in each of the 6 wells in the plate. We think that these dividing cells may be neural stem cells or progenitor cells.

3.6 Dual channel fluorescence imaging

For biological experiments which require more than one fluorescence channel, current EmSight can accommodate more fluorescence channel by modifying fluorescence imaging parts. In Figure 3.13, an example of dual channel fluorescence version of EmSight is

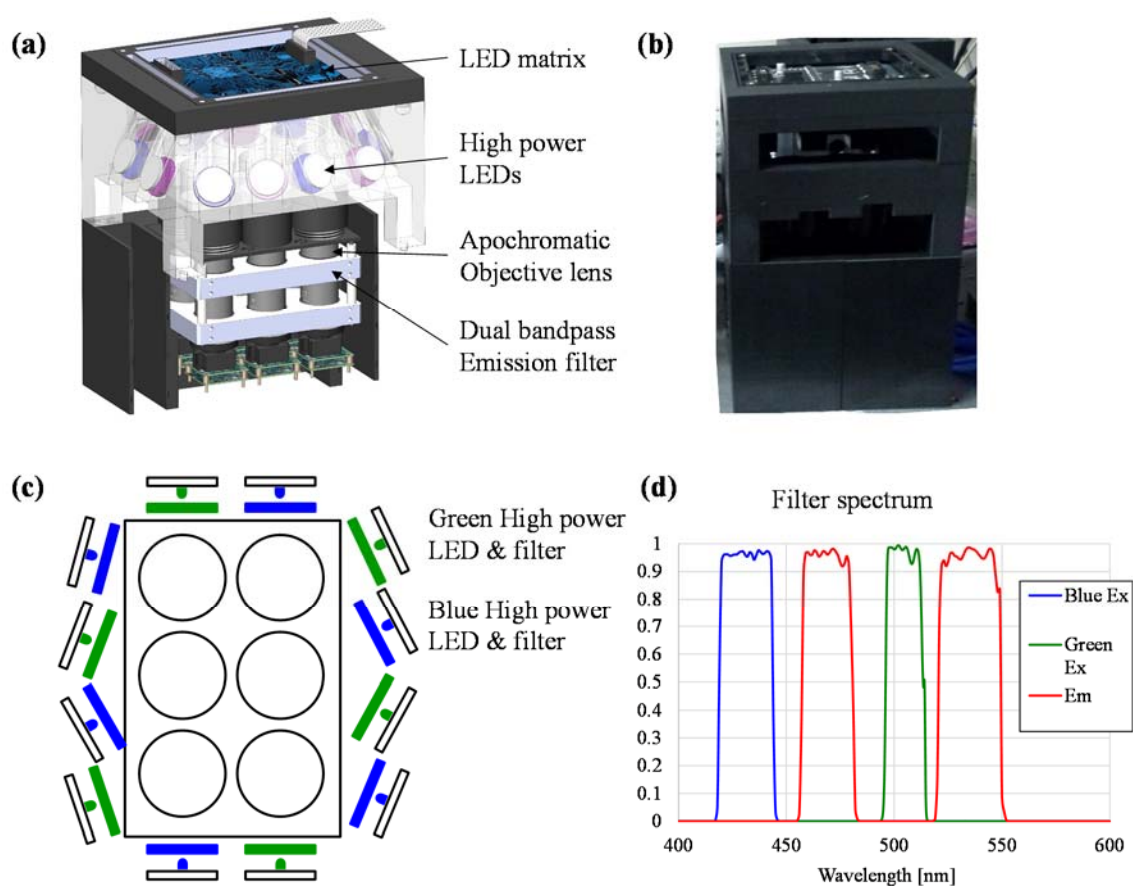


Figure 3.13: EmSight with dual channel fluorescence imaging. (a) Configuration of dual channel fluorescence EmSight. (b) Prototype of dual channel fluorescence EmSight. (c) Positions of dual channel excitation light sources around a 6well plate. (d) Excitation and emission filter spectrum for CFP/YFP dual channel fluorescence imaging.

shown. Several optical parts need to be changed for multi-channel fluorescence imaging. For dual channel fluorescence, two excitation light sources are necessary for each fluorophore. In order to illuminate 6 wells for dual channel excitation, we located 6 blue high power LEDs (420 nm) and 6 green high power LEDs (530 nm) along with matching excitation filters (430 nm / 24 nm, 504 nm / 12 nm) around the well plate as shown in Figure 3.13 (c). Because the fluorescence emissions from two different fluorophores have different spectrum, the emission filters in EmSight need to have dual pass bands for each emission spectrum. The excitation and emission filter combination for CFP/YFP dual

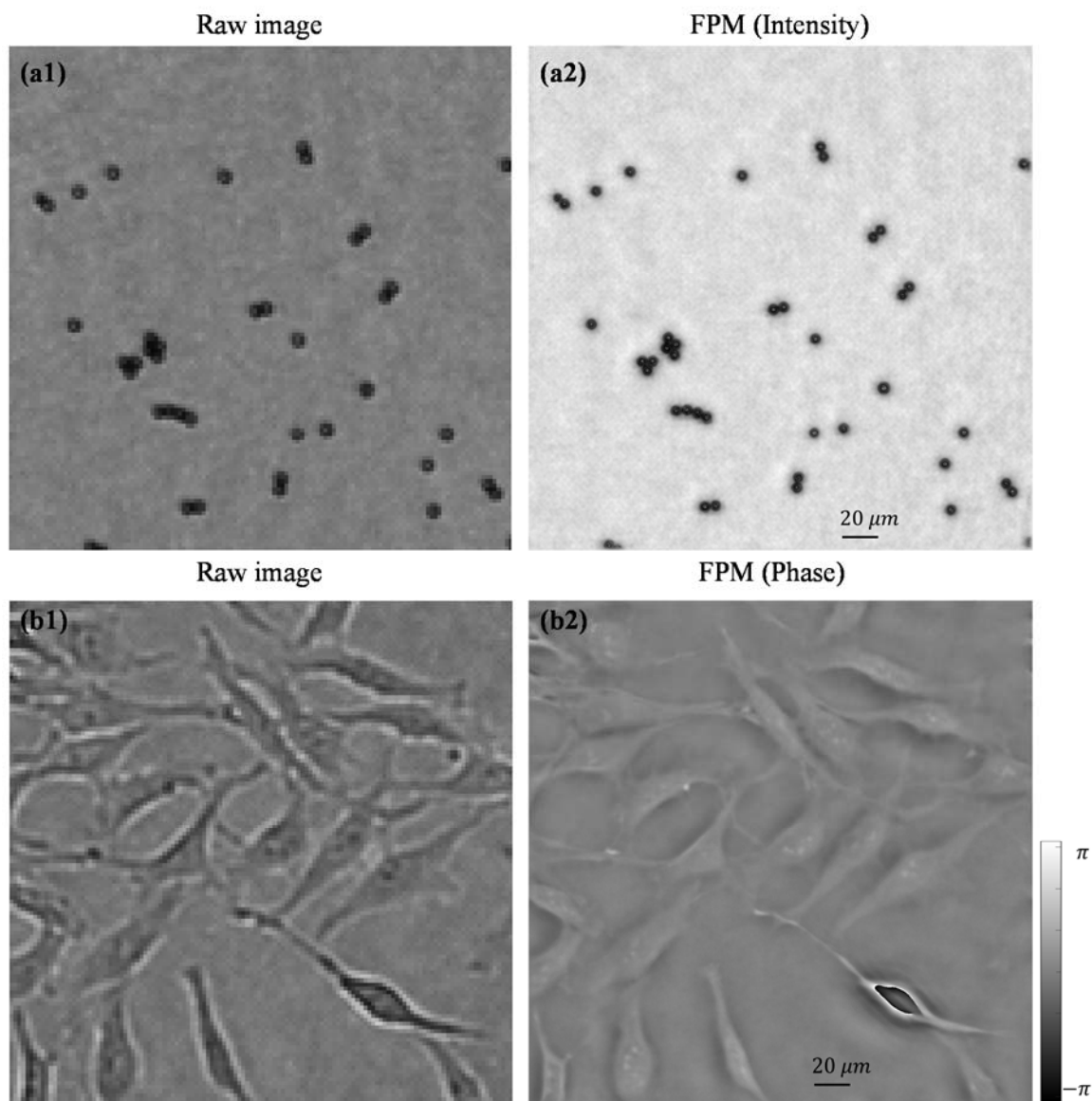


Figure 3.14: FPM imaging of dual channel fluorescence EmSight. (a) Intensity sample: 6 μm beads. (b) Phase sample: HeLa cell line.

channel fluorescence imaging is shown in Figure 3.13 (d). Lastly, the objective lens needs to be changed with the one of which chromatic aberration is corrected because fluorescence images from different emission spectrum should be focused simultaneously. In this dual channel fluorescence EmSight, we used Olympus 2X / NA0.08 Apochromatic objective lenses. The prototype of dual channel fluorescence EmSight is shown in Figure 1.13 (b).

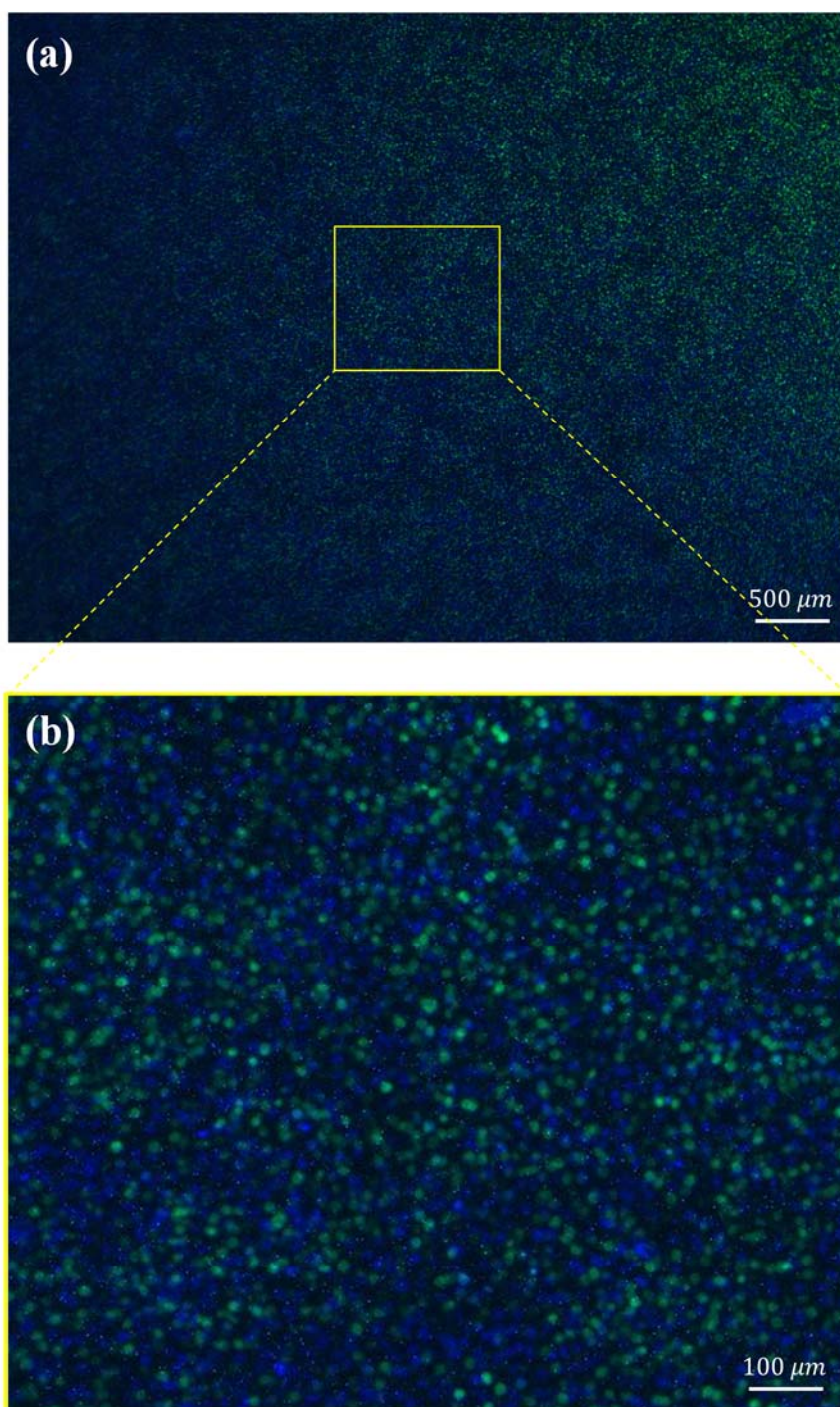


Figure 3.15: Dual channel fluorescence imaging of dual channel fluorescence EmSight. Blue color: 3T3 sender cells (mTurquoise2), Green color: 3T3 receiver cells (Citrine). (a) Full FOV dual channel fluorescence. (b) Enlarged image from a position indicated in (a).

As imaging examples, the FPM reconstruction images from an intensity sample (6 μm

sized bead) and a phase sample (HeLa cell line) are shown in Figure 1.14 and dual channel fluorescence image from sender and receiver 3T3 cells is shown in Figure 1.15.

3.7 Discussion and conclusion

We have successfully developed an incubator embedded cell culture imaging microscope (EmSight) system based on the Fourier ptychographic microscopy (FPM) method. We used two inexpensive low magnification objectives to perform 1:1 imaging of the target culture onto the imaging sensor chip. By using the FPM method, a single imaging unit of the EmSight makes a synthetic NA of 0.42 and the FOV of $5.7 \text{ mm} \times 4.3 \text{ mm}$ within the footprint of $3 \text{ cm} \times 3 \text{ cm}$. This EmSight prototype contained six sets of the imaging units for a 6-well plate cell culture imaging. We think the EmSight system can be a useful imaging solution for parallel culture experiments which have different manipulations for each well, as drug testing. As shown in Figure 3.12, EmSight can also be used for tracking cell lines or stem cell differentiation.

We expect that the present configuration of the EmSight system can be further expanded to 12-well ANSI plates if the imaging sensor board is redesigned for higher density. We note that we captured wells sequentially in our neuron imaging experiment because the time between each imaging sequence (1 hour) was long enough to capture each well one at a time. For a simultaneous imaging from 6 wells, we can upgrade imaging cameras to cameras with high dynamic range and apply the multiple LED illumination method from [53, 54] in order to boost capturing speed for a frame data set.

Recently, live cell imaging via FPM has been reported [53]. In that paper, the authors implemented a high speed FPM imaging system (greater than 1 frame per second) that is capable of tracking fast dynamic movement of cells during in-vitro culture. The system was built on a conventional inverted microscope platform and is designed for examining a single culture. This work is distinct in that the EmSight system is designed to be sufficiently compact to be housed in an incubator, cost-effective and is capable of imaging several wells in a culture well plate over a long timeline (a few weeks). Both the EmSight system and the system in [53] are designed for cell culture experiments. However, they are each

designed to fit the needs of different cell culture experimental formats. EmSight is designed for streaming a lot of culture FPM data associated with multiple cultures from an incubator; while the system in [53] is focused on very fast imaging of a single cell culture.

We conducted a set of 21-day mouse ventral midbrain culture experiments to demonstrate the long-term cell culture imaging capabilities of the EmSight system. With its naturally long DOF of 0.2 mm, defocused images acquired during the culture process can be digitally refocused using the iterative Fourier ptychographic reconstruction algorithm. The fluorescence imaging functionality built in the EmSight enabled the specific identification of DA (eGFP-positive) neurons from mixed primary cultures. From the time-lapse imaging, eGFP positive DA neurons were successfully tracked, *i.e.* the distance and the direction the cell moved was determined.

This type of analysis can be applied to the study of certain brain diseases, such as Parkinson's disease (PD). PD involves a widespread neuronal malfunction, especially pronounced degeneration of DA neurons of the substantia nigra pars compacta (SNc) [55-58]. Tracking of DA neurons in a culture can provide useful insights into the characteristics of DA neurons during degeneration. By the wide FOV imaging functionality combined with fluorescence imaging, EmSight is well suited for identifying and tracking of such a rare event in fully populated cells over long periods of time. We plan to apply improved image processing methods to the time-lapse images in future research. Such methods will enable one to obtain data on neurite length and neurite branching. These are key aspects of neuronal development, degeneration, and repair.

96EYES: HIGH THROUGHPUT 96 WELL PLATE IMAGING SYSTEM FOR FAST DRUG SCREENING

4.1 Introduction

Demands for high throughput imaging systems are growing as the number of assays in biomedical experiments is increasing dramatically, especially for drug discovery [59, 60]. The 96 well plate is one type of experimental platform that biologists are using for testing multiple conditions at the same time. It is important to check the status of assays after the experiment; however, it is time consuming to image every well in the 96 well plate using a conventional microscope because the well plate needs to be mechanically scanned the large area of the well plate and focused again every time the sample moves out-of-focus. The common way to deal with this issue is to measure fluorescence intensity or scattering from each well as a whole using a well plate reader. This method gives us cumulative variations by experimental conditions; however, it cannot give us details about the sample movement or topological changes. There are commercial microscopes which are designed to image 96 well plates, but their throughput is fundamentally limited because they still rely on the single imaging system and need to scan the well plates in order to image them. There has been an approach to make parallel imaging system without having light focusing elements [61]. The system assembled 96 CMOS imaging sensors into the footprint of a 96 well plate and put a 96 well plate directly on top of the 96 sensor surface. Because the images from the 96 wells are captured in a parallel way, the capture speed can be fast; however, due to the lack of a lens the resultant image quality becomes too poor to be used in cellular level experiments.

Fourier ptychography (FP) can be a good solution to solve the image quality problem in the parallel imaging system. There are several advantages that make FP a good fit in the parallel 96 well plate imaging system. First, FP moves optical problems into computational problems, so it does not require well designed objective lenses in order to get high resolution images across a wide FOV. This gives us freedom to choose any compact sized lens elements

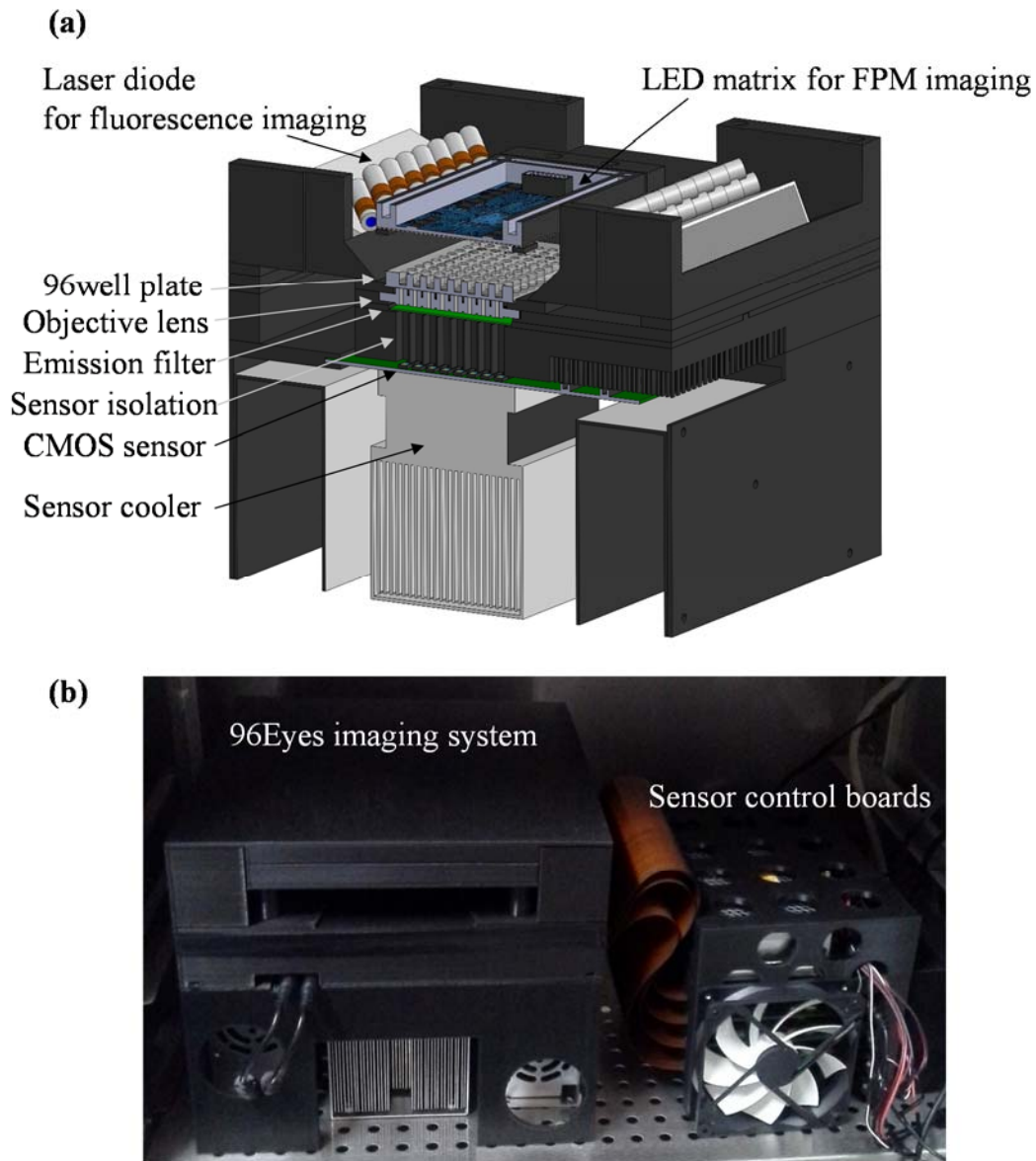


Figure 4.1: 96Eyes system configuration. (a) Cross-section view of 96Eyes. From top to bottom, an LED matrix for FPM varied angle illumination, a 96 well plate, 96 objective lenses, an emission filter, 96 CMOS imaging sensors, and a Peltier cooler configure 96 parallel imaging systems. For the excitation light source for fluorescence imaging, 30 laser diodes (15 laser diodes per each side) are positioned to the side of the LED matrix. (b) Prototype of 96Eyes. The system consists of a main imaging system and additional imaging sensor control boards.

for light focusing purposes. Second, FP's digital refocusing functionality relieves the burden

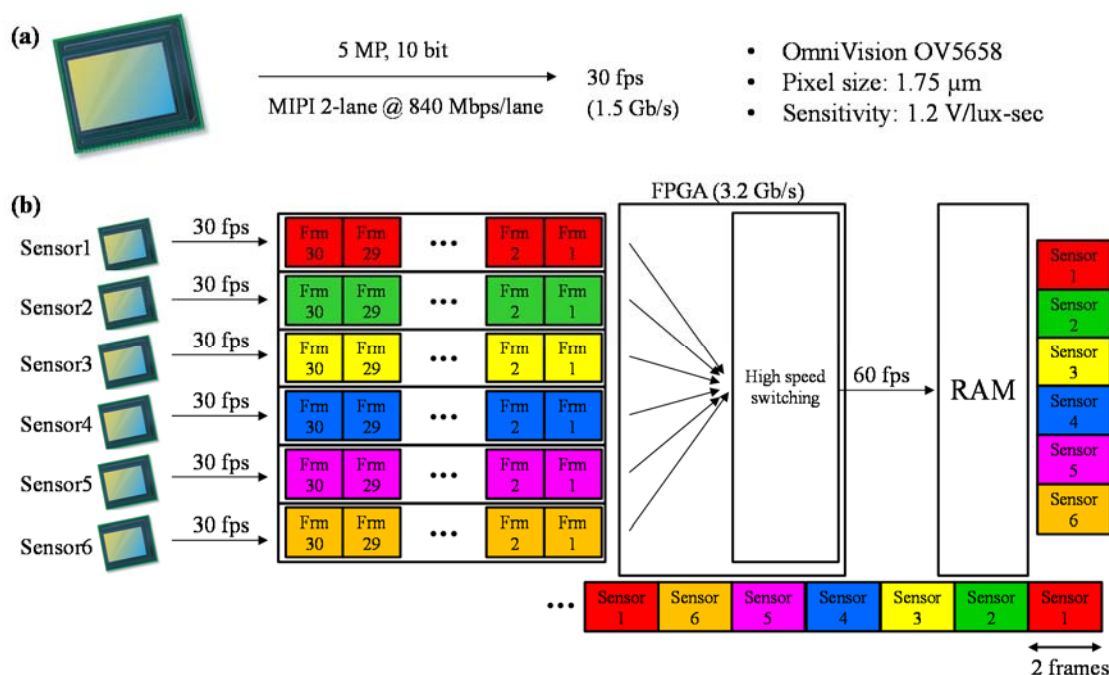


Figure 4.2: Imaging sensor board operation. (a) A single imaging sensor operation. (b) A basic sensor unit operation. A sensor unit is composed of 6 imaging sensors, 1 FPGA, and 1 DDR2 buffer memory.

of focusing 96 wells perfectly at the same time. Third, FP does not require any phase plate or prism in order to get a phase image from transparent biological samples, which enables a simple configuration of the system for phase imaging in the compact sized parallel imaging system.

In this chapter, we introduce a fully parallel 96 well plate imaging system based on the Fourier ptychographic microscopy, which we named as 96Eyes. Basically 96Eyes is 96 compact Fourier ptychographic microscopes assembled in a 96 well plate footprint. Each Fourier ptychographic microscope works independently with other Fourier ptychographic microscopes in the system, and as a result the system throughput increases proportional to the number of parallel microscopes in the imaging system. In Section 4.2, we describe the configuration of the 96Eyes imaging system in detail, and the system characterization is

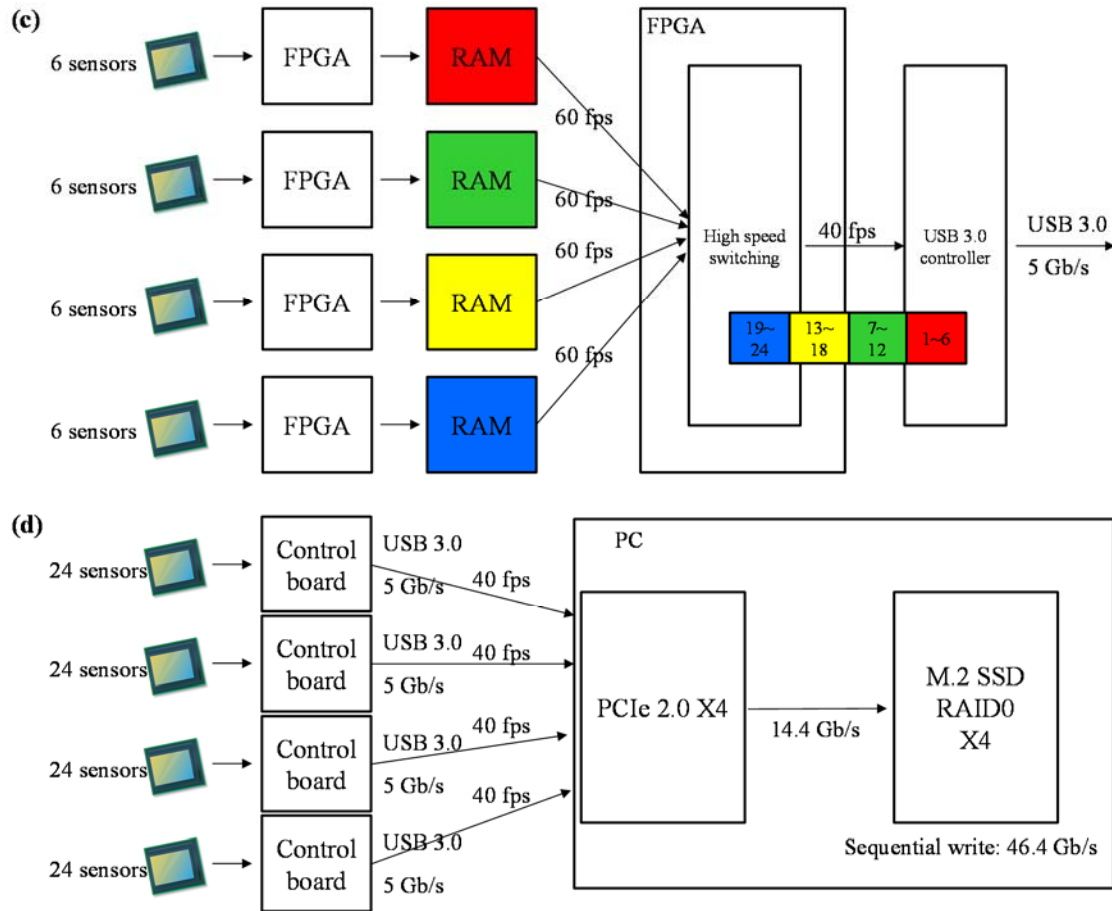


Figure 4.2 (cont.): (c) A sensor control board operation. 4 sensor units, 1 FPGA, and a USB 3.0 controller control the image readout process from 24 imaging sensors. (d) 96Eyes imaging sensor operation. The images from every 24 imaging sensors are serialized by a control board which is assigned to the 24 sensors and transferred to a PC storage driver by USB 3.0 protocol. Images from total 96 imaging sensors are transferred and saved into an SSD storage drive by 4 control boards and 4 USB 3.0 cables.

made using micro beads and biological samples in Section 4.3. We conclude this chapter with a discussion about possible applications and updates for 96Eyes.

4.2 System configuration

Basic configuration of 96Eyes is similar to the configuration of EmSight in Chapter 3. Figure 4.1 (a) shows the cross-section view of 96Eyes for better illustration of inside parts. For the FPM varied angled illumination, an RGB LED matrix (pitch size: 3 mm) is positioned

30 mm above the sample 96 well plate location. 4 mm below the bottom layer of the well plate, custom-made 96 objective lenses (pitch: 9 mm) are located, configuring finite corrected parallel imaging systems. Aligned with the objective lenses, 96 CMOS imaging sensors (pitch: 9 mm) are loaded on top of a Peltier cold plate. The light path from each objective lens and imaging sensor is isolated from the light path of other imaging units by sensor isolation walls in order to prevent unnecessary interference between imaging units. For the fluorescence imaging, laser diodes positioned at both sides of the LED matrix illuminate the whole plate area for excitation, and a plate of emission filter is seated between the objective lens layer and the imaging sensor layer as shown in Figure 4.1 (a). In Figure 4.1 (b), first prototype of 96Eyes is shown. Along with the main imaging system, there are 4 additional imaging sensor control boards connected to the main imaging system by flexible cables.

4.2.1 Imaging sensor board

The imaging sensor board is the main part of 96Eyes that determines the imaging throughput of the system. For fast image capture from 96 imaging sensors, we custom-made the imaging sensor board (Aview Image Technology). Our CMOS imaging sensor is the OmniVision OV5658 5 MP (2592×1944) color imaging sensor, which has a pixel size of $1.75 \mu\text{m}$ and sensitivity of 1200 mV/Lux-sec. Due to the Bayer color filter on the sensor, we only use the Green channel for imaging among RGGB color channels, resulting in the effective pixel size of $1.75 \mu\text{m} \times \sqrt{2} = 2.47 \mu\text{m}$. Data readout sequence of the imaging sensor board is illustrated in Figure 4.2. As shown in Figure 4.2 (a), 5MP of 10 bit raw imaging data from an imaging sensor has data transfer speed of 30 fps using 2 lane Mobile Industry Processor Interface (MIPI) protocol. In one sensor unit, 6 imaging sensors transfer images into an FPGA board in 30 fps each, and the FPGA board serializes the images from 6 sensors and saves the images into DDR2 buffer memory. Due to the different data transfer delays from difference imaging sensor locations, the images from different imaging sensors are asynchronously switched by the FPGA and the resultant serialized image data are saved at about 60 fps into buffer memory, as shown in Figure 4.2 (b). There are 4 such FPGAs and buffer memories on an imaging control board, so images from 24 sensors are being saved

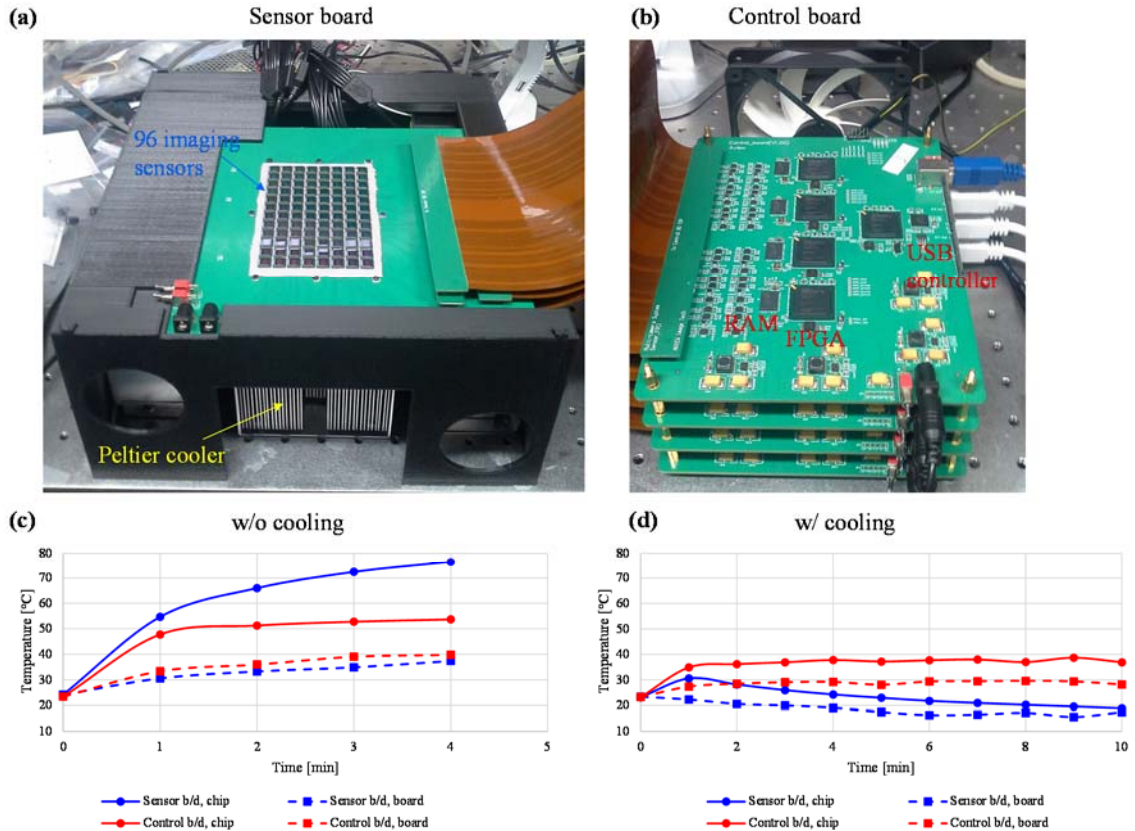


Figure 4.3: Cooling of imaging sensor system. (a) A Peltier cooler is attached on the bottom surface of imaging sensor area in order to cool the heat generated by the 96 CMOS sensors. (b) 4 stacked sensor control boards. A 120 mm fan is used for cooling control boards. (c and d) Temperature change of sensor board and control board without or with coolers, respectively. Temperatures of the solid curves are measured on the chip surface, and temperature of the dotted curves are measure on the PCB board surface.

into 4 buffer memories in parallel, and these saved images are transferred to another FPGA which serializes the images from 4 buffer memories again and sends the serialized images to a universal serial bus (USB) 3.0 controller. Here, due to the maximum theoretical speed of a USB 3.0 protocol (5 Gb/s), the final image transfer speed from 24 sensors is limited by approximately 40 fps (1.6 frames per sensor per second), as shown in Figure 4.2 (c). 96 imaging sensors are connected to 4 control boards like in Figure 4.2 (d), and control boards are connected to a PCIe 2.0 X4 USB adapter card which has 14.4 Gb/s speed. The transferred

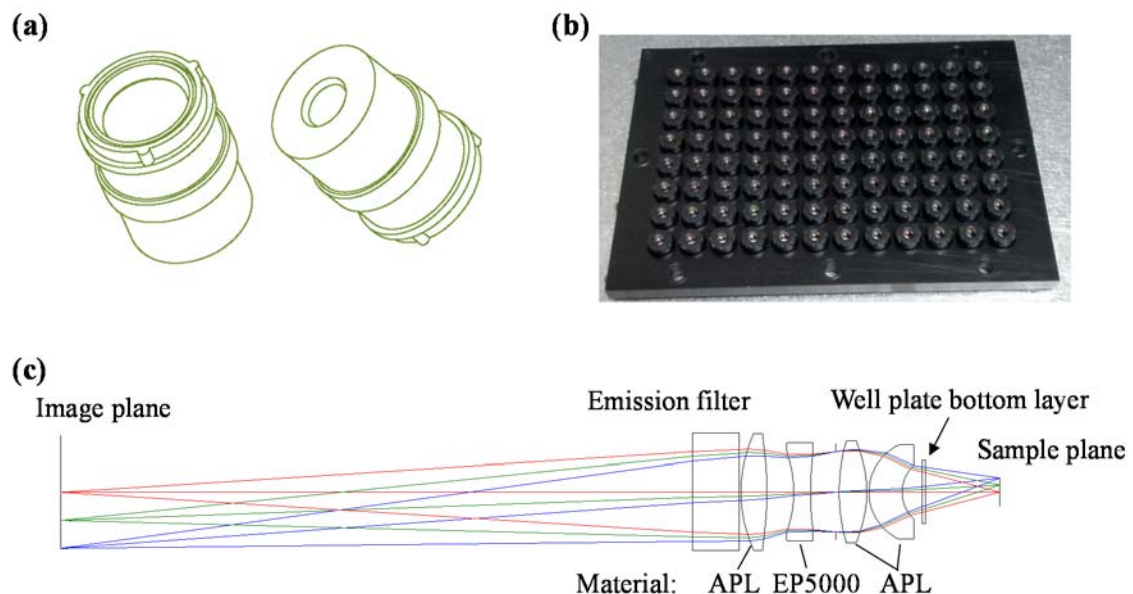


Figure 4.4: Injection molding polymer objective lens. (a) Schematic of custom-made objective lens. (b) 96 objective lenses assembled into a metal plate. (c) Design of the finite corrected objective lens. APL and EP5000 are used in order to correct chromatic aberration, and an emission filter and the well plate bottom layer are included in the design process.

images are saved into a 4X redundant array of independent disks (RAID) 0 configured M.2 SSD drives which have a sequential write speed of 46.4 Gb/s.

Each imaging sensor generates 300 mW of heat during operation, so 29 W of heat in total is emitted from the size of a well plate area. This generated heat not only degrades the quality of images due to the heat generated electron noises, but it can damage the sensor board itself. In order to address this issue, we use a Peltier cooler and attach the cold plate of cooler right below the sensor area, as shown in Figure 4.3 (a). Figure 4.3 (c) and (d) show the temperature change of the board from the start of imaging without and with cooling, respectively. The solid curves indicate the temperature on the chip surface and the dotted curves are for the temperature on the PCB board surface. As expected, the temperature on the imaging sensor surface increases fast and reaches 80 °C after 4 minutes of power on. After using the Peltier cooler, the temperature of the sensor stabilizes around ambient

Table 4.1: Dispersion of the materials used in the objective lens.

		APL5514	EP-5000
Refractive Index @ 25 °C	n_h (404.7 nm)	1.5609	1.6863
	n_g (435.8 nm)	1.5564	1.6714
	n_F (486.1 nm)	1.5509	1.6546
	n_e (546.1 nm)	1.5464	1.6417
	n_d (587.6 nm)	1.5441	1.6355
	n_C (656.3 nm)	1.5412	1.6280
	n_{780} (780.1 nm)	1.5379	1.6196
Abbe number	$V_d = \frac{n_d - 1}{n_F - n_C}$	56.09	23.89

temperature. For the cooling of control boards, we installed a 120 mm cooling fan on the system, and as a result the temperature of chips on the control boards decreased from 55 °C (without cooling) to 38 °C (with cooling).

4.2.2 Injection molding polymer objective lens

The objective lens is another important part of 96Eyes which determines the resolution and FOV of image. We custom-designed the objective lens using the injection molding method (MaxEmil Photonics Corporation). The schematic design and prototype of the objective lens are shown in Figure 4.4. The lens has a barrel diameter of 8 mm, and it is loaded onto a metal plate with pitch size of 9 mm. The lens is composed of four lens elements inside, as shown in Figure 4.4 (c). Two different materials are used in the design in order to minimize the chromatic aberration. The refractive index and Abbe number of two materials

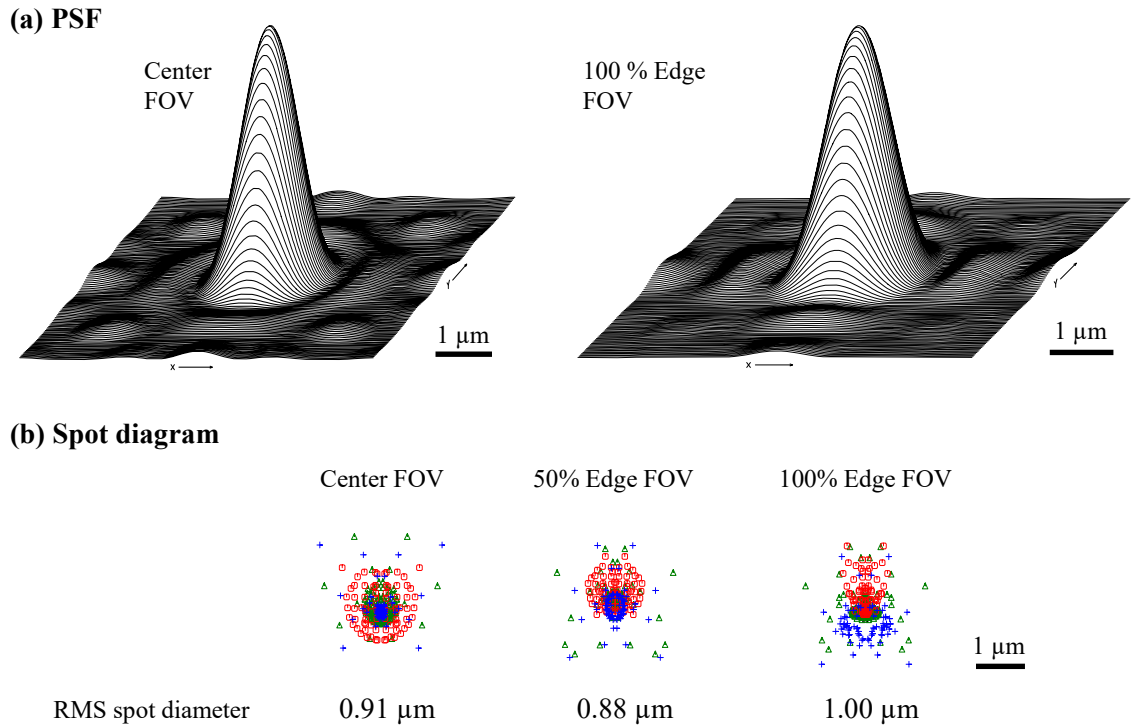


Figure 4.5: CODE V ray tracing simulation result. (a) Point spread function of the objective lens. (b) Spot diagram of the objective lens from different field locations.

are listed in Table 4.1. In the lens design, we made the lens finite corrected, mainly due to the simplicity of design and alignment of 96 lenses. We included all possible parts between the sample and detector in the design process in order to minimize the aberration related to this additional part. This includes an emission filter and the well plate bottom layer. The design is done for the light bandwidth of $530 \text{ nm} \pm 15 \text{ nm}$, and CODE V ray tracing software is used for the simulation. The simulation result of 4X / NA0.23 objective lens which has working distance of 4 mm and FOV of $\varnothing 1.6 \text{ mm}$ is shown in Figure 4.5. The designed diffraction limited resolution is $1 \mu\text{m}$ across the FOV, however, the actual resolution is poorer than this and needs to be measured due to the manufacturing and alignment errors.

4.2.3 LED matrix operation for FPM illumination

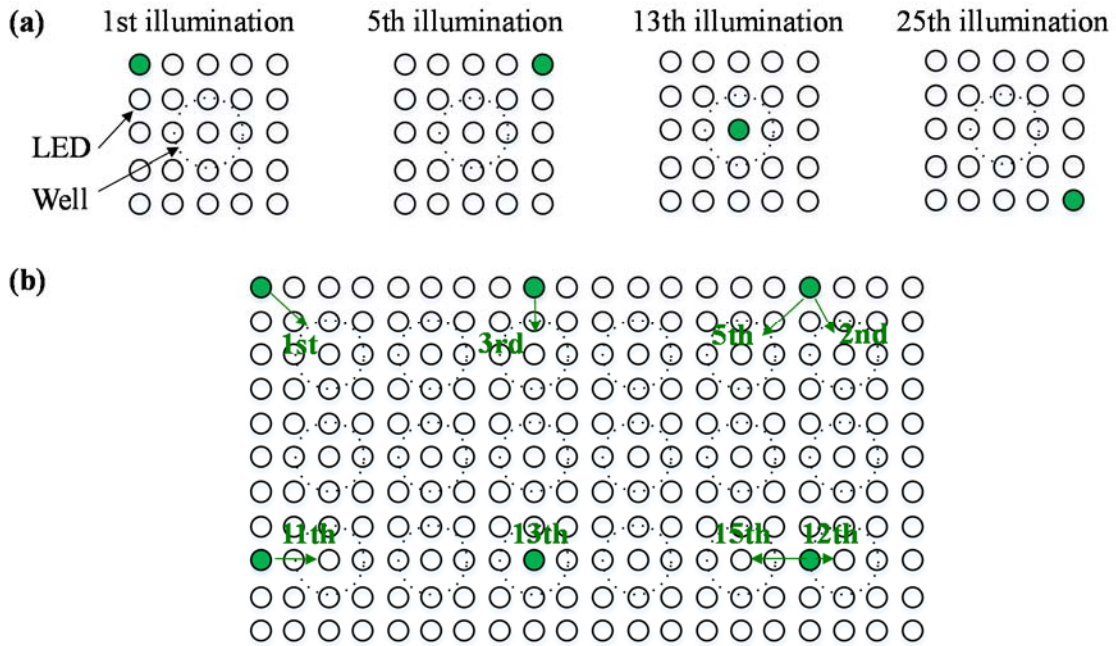


Figure 4.6: LED matrix operation for FPM illumination. (a) A single imaging system captured a well from 25 different illumination directions. Here, 1st, 5th, 13th, and 25th illumination conditions are illustrated for example. The 13th illumination makes the direct plane illumination to the sample. (b) In order to coherently illuminate multiple wells, every 8th LEDs are turned on simultaneously during the image capture process. Based on the relative location of a well to the nearest turned-on LED, each well experience different illumination condition under the same LED pattern. The numbers on the diagram indicate the illumination condition each well experience in this LED pattern.

In 96Eyes, each sample is captured from 25 different illumination angles for the FPM image acquisition. Figure 4.6 (a) shows four different illumination conditions among the 25 illuminations. When light is on the 1st illumination condition, the sample is illuminated from the most upper left corner of light source which has illumination NA of 0.25. The 13th illumination condition makes a direct plane wave illumination on the sample. For the best coherent illumination condition, it is required to turn on a single LED from the matrix and capture images from the single coherent light source. However, it takes too much time to scan all the LED matrix by turning on single LED at a time. In order to make the data acquisition process faster, every 8th LED is turned on simultaneously for the 96Eyes illumination as shown in Figure 4.6 (b). We determined the space between LEDs which are

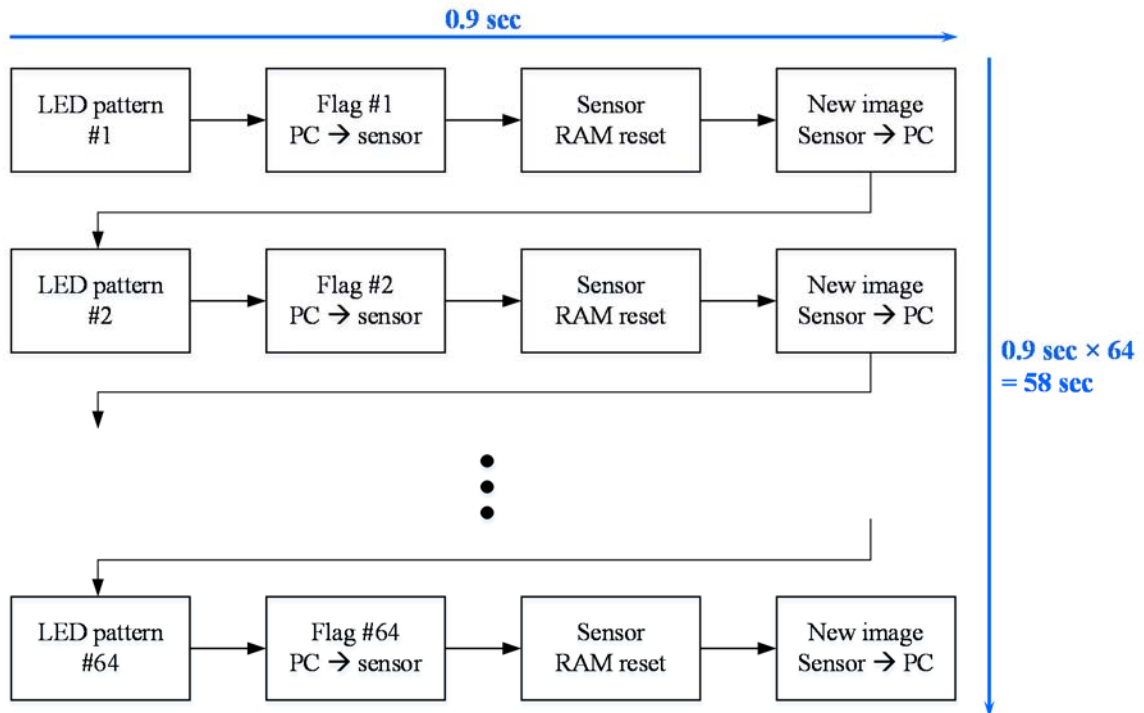


Figure 4.7: FPM image acquisition process. When an LED pattern is made on the LED matrix, a main computer send a flag signal to the image control boards, which indicates a new LED pattern is displayed on the matrix. In order to send new images captured under the new LED pattern, the buffer memory in the control boards is reset upon arrival of flag signal. New images saved on the buffer memory are transferred and saved to PC along with flag information. This entire process takes 0.9 seconds. After finishing data save, the LED matrix changes into a next pattern and whole process repeats until all images from 64 LED patterns are saved. Total image capture time for 64 LED patterns is 58 seconds.

turned on at the same time as 8 based on the measured minimum distance between LEDs which does not make illumination interference on any imaging locations. Because multiple LEDs turn on at the same time, each well experiences different illumination condition under the same LED pattern. In Figure 4.6 (b), illumination conditions that each wells are under exposure are labeled as numbers for one type of LED pattern.

The entire image acquisition process is illustrated in Figure 4.7. A main computer sets and turns on pattern 1 on the LED matrix, and then sends a flag signal to the imaging sensor

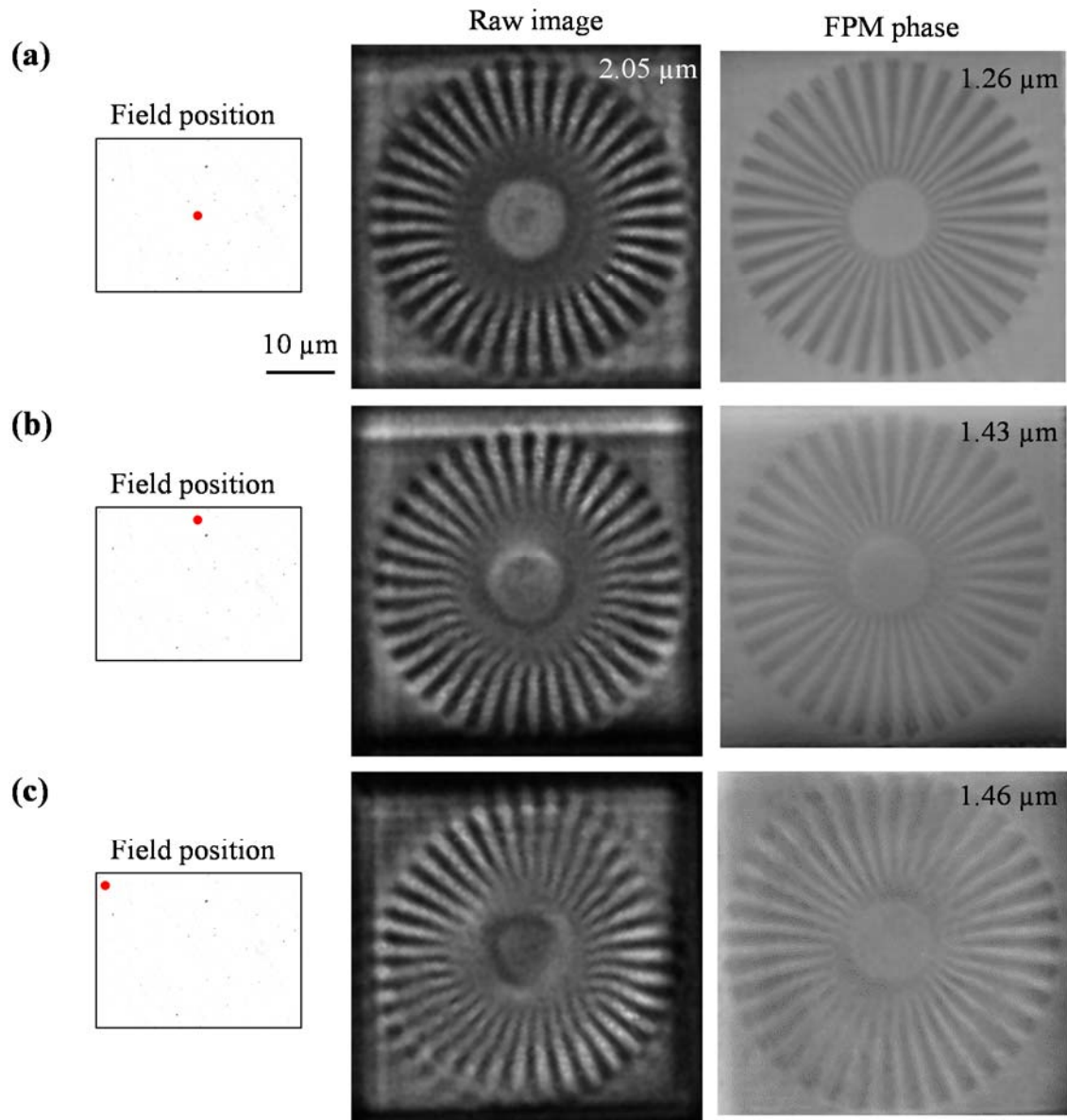


Figure 4.8: FPM resolution test of 96Eyes. The sample is a Siemens star phase sample of maximum line pitch of $4 \mu\text{m}$ and minimum line pitch of $1 \mu\text{m}$. (a-c) The raw captured images and FPM reconstructed phase images from field positions which are at center, $425 \mu\text{m}$, and $710 \mu\text{m}$ away from center of FOV, respectively.

board. On arrival of the flag signal, the image control board resets the internal buffer memory in order to prevent the images from the previous illumination condition being transferred to the computer in current illumination pattern. After that, new images are saved into the buffer

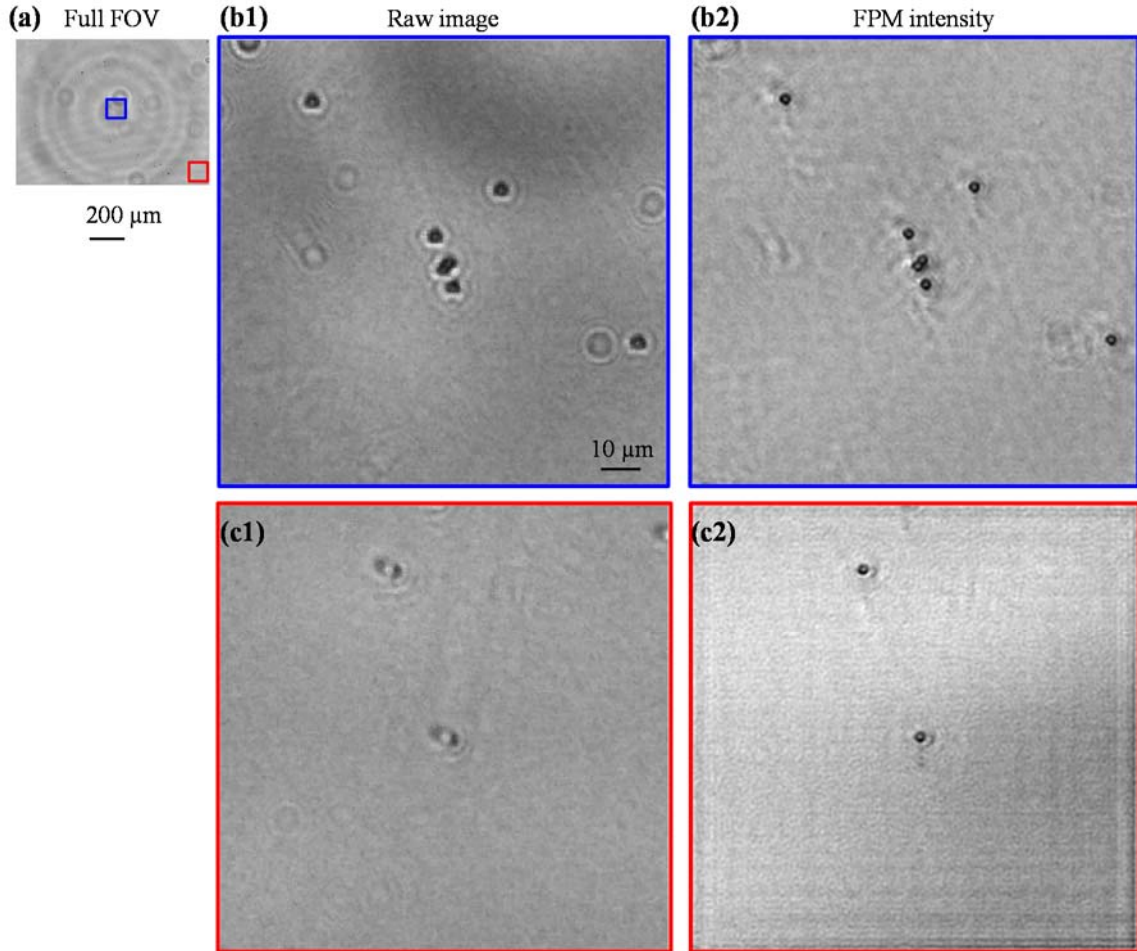


Figure 4.9: FPM intensity imaging test of 96Eyes. The intensity sample is 2 μm sized beads. (a) A full FOV raw image. (b and c) Raw images and FPM reconstructed intensity images from the locations indicated in (a).

memory and transferred to the main computer for saving. All this process takes about 0.9 seconds as determined mainly by the capture speed of the imaging sensor board. After saving all images into the storage drive, the main computer changes LED matrix into pattern 2, and all the image acquisition process repeats. Because we have $8 \times 8 = 64$ different LED patterns, it takes about 58 seconds to capture all raw images which are needed for FPM image reconstruction.

4.3 System characterization

4.3.1 Image resolution of 96Eyes

We characterized the system image resolution using a Siemens star phase sample as shown in Figure 4.8. Considering 4X magnification of the objective lens and the size of imaging sensor, each image from 96Eyes has FOV of $1.1 \text{ mm} \times 0.85 \text{ mm}$. We captured the same sample from the three different field positions (center, top, and top-left corner) in order to check the resolution difference by field location. The result is shown in Figure 4.8. At the center FOV where the optical aberration is best corrected, the raw image has a resolution of

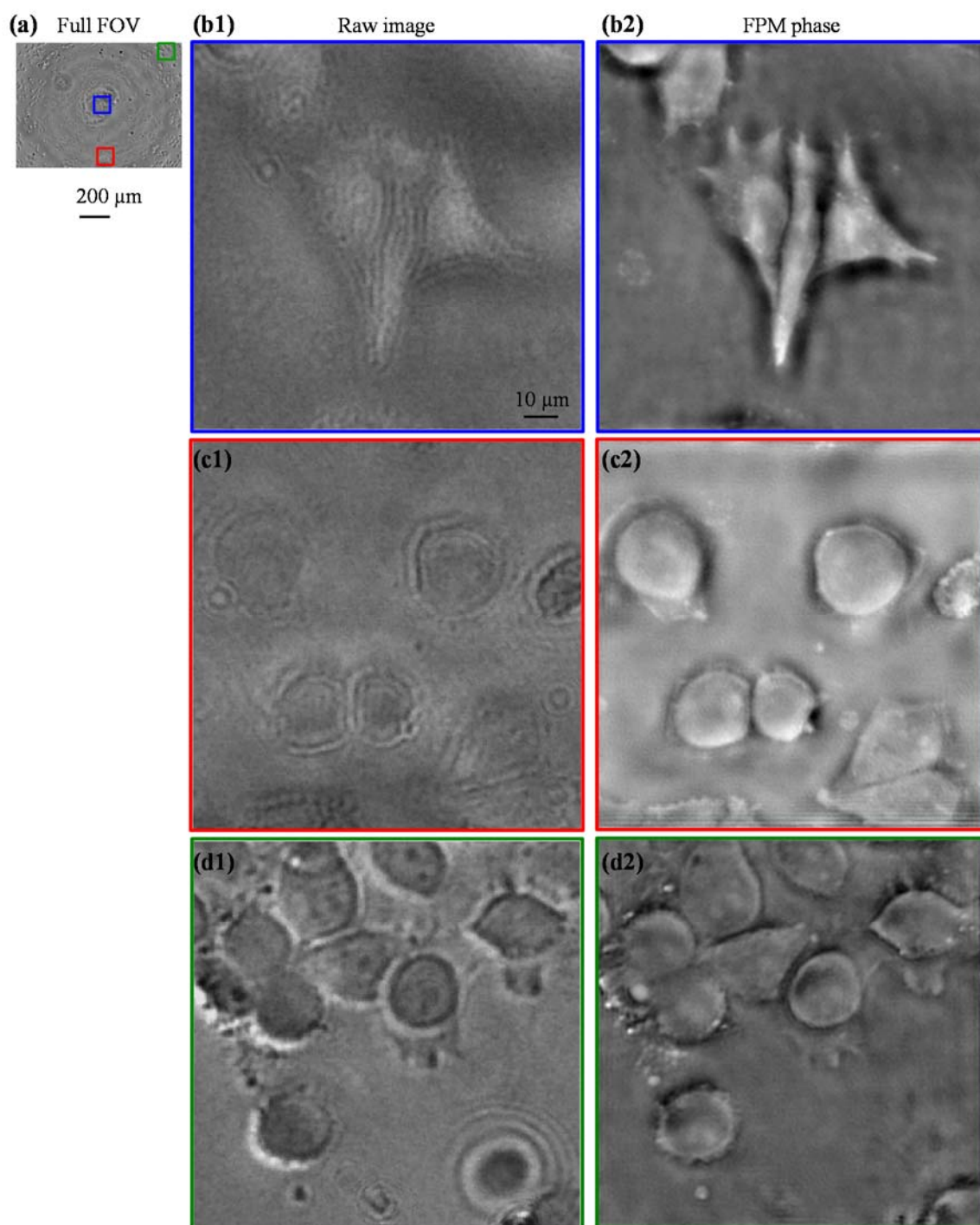


Figure 4.10: FPM phase imaging test of 96Eyes. The phase sample is fixed HeLa cell line. (a) A full FOV raw image. (b-d) Raw images and FPM reconstructed phase images from the locations indicated in (a).

2.05 μm , and the resolution improves to 1.26 μm in the FPM reconstructed phase image

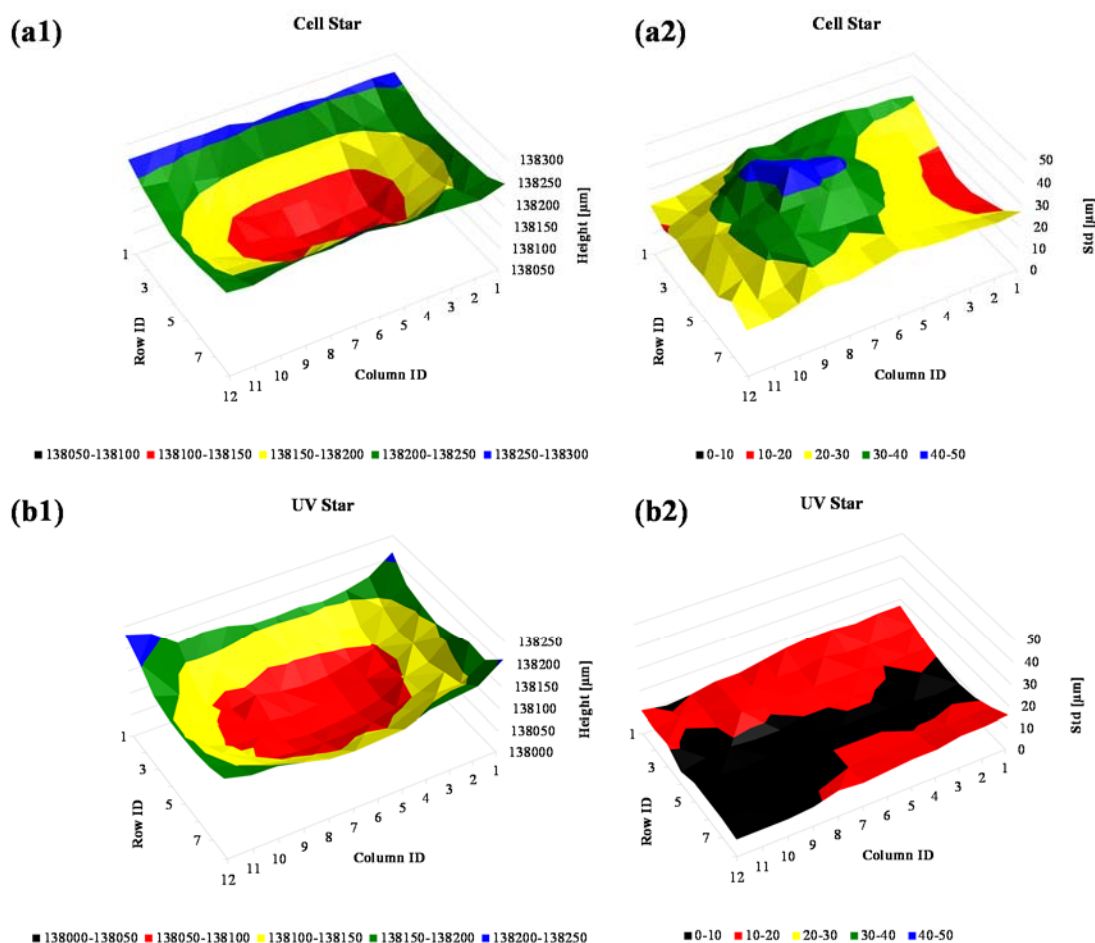


Figure 4.11: 96 well plate bottom height distribution. (a) Average and standard deviation of well bottom heights measured from 19 polystyrene 96 well plates. (b) Average and standard deviation of well bottom heights measured from 16 cyclic olefin copolymer (COC) 96 well plates.

making about twice the resolution enhancement. For the top corner (425 μm away from the center FOV) and top-left corner (710 μm away from the center FOV), the images are experiencing off-axis aberrations and the line spokes become curved. These curved lines are corrected straight during the FPM reconstruction process as shown in Figure 4.8.

We checked the resolution enhancement and the aberration correction of FPM using typical intensity and phase samples. The images using 2 μm sized beads for FPM intensity

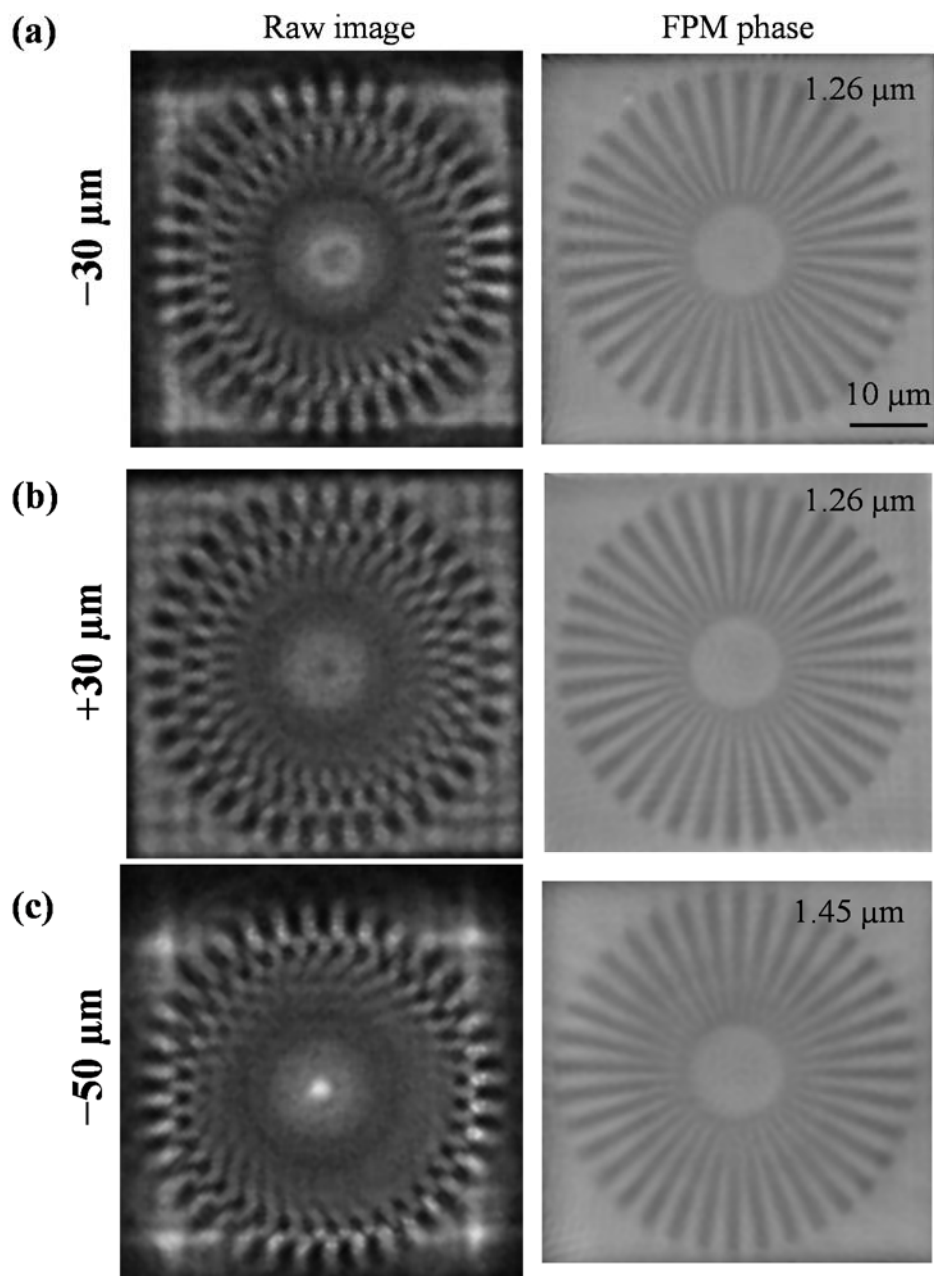


Figure 4.12: Digital refocusing of 96Eyes. The sample is the same Siemens star phase target used in Figure 4.8. (a-c) Raw images and digitally refocused FPM phase images from the sample defocused by $-30\ \mu\text{m}$, $+30\ \mu\text{m}$, and $-50\ \mu\text{m}$, respectively.

imaging tests are shown in Figure 4.9. The $2\ \mu\text{m}$ sized beads which are attached to each other are clearly resolved in the FPM reconstructed intensity image. At the bottom-right corner of

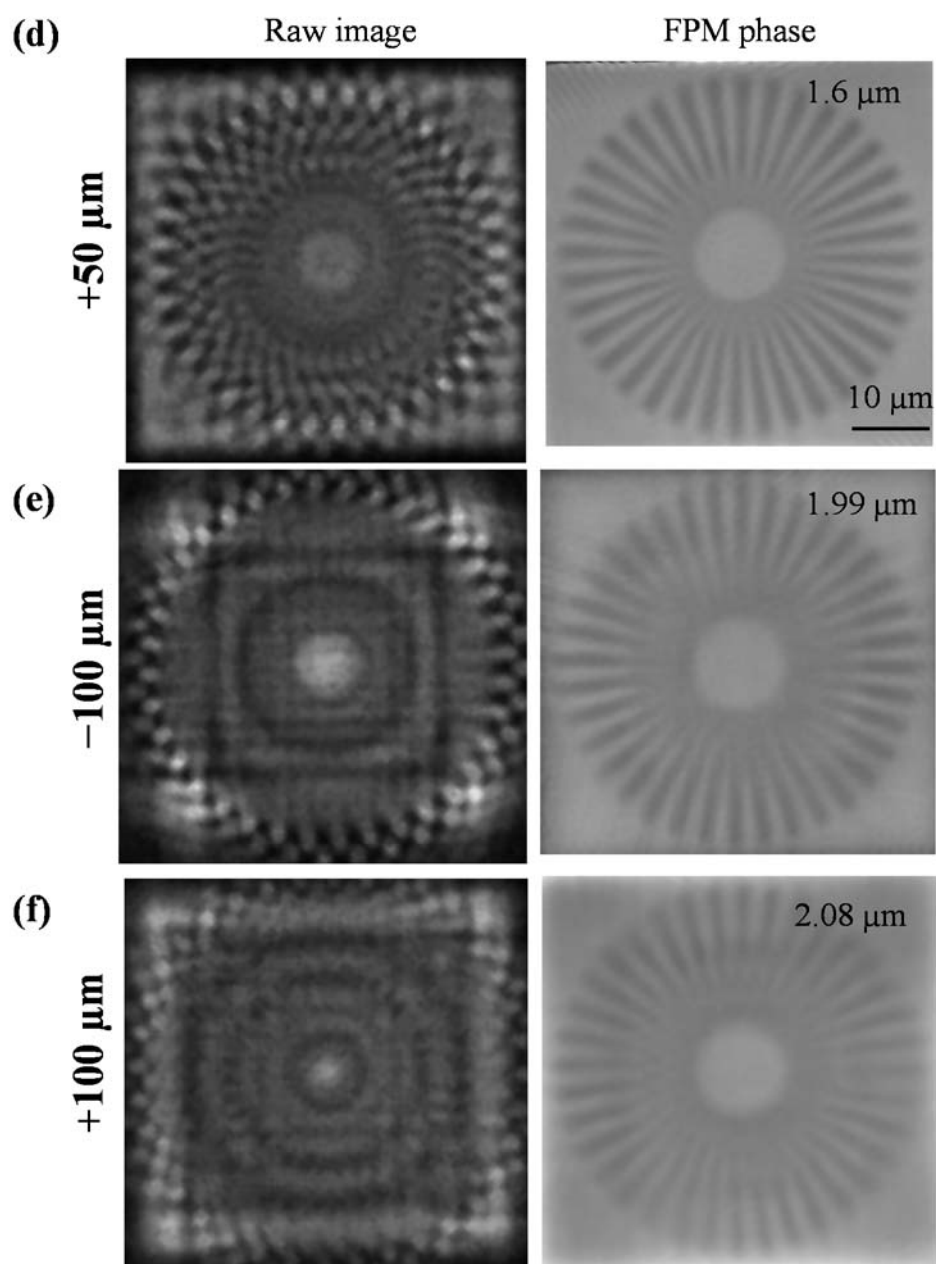


Figure 4.12 (*cont.*): (d-f) Raw images and digitally refocused FPM phase images from the sample defocused by +50 μm , -100 μm , and +100 μm , respectively.

FOV, the beads from the raw image are not distinguishable due to the highly aberrated shape. However, the beads become spherical after FPM aberration correction, as shown in Figure 4.9 (c).

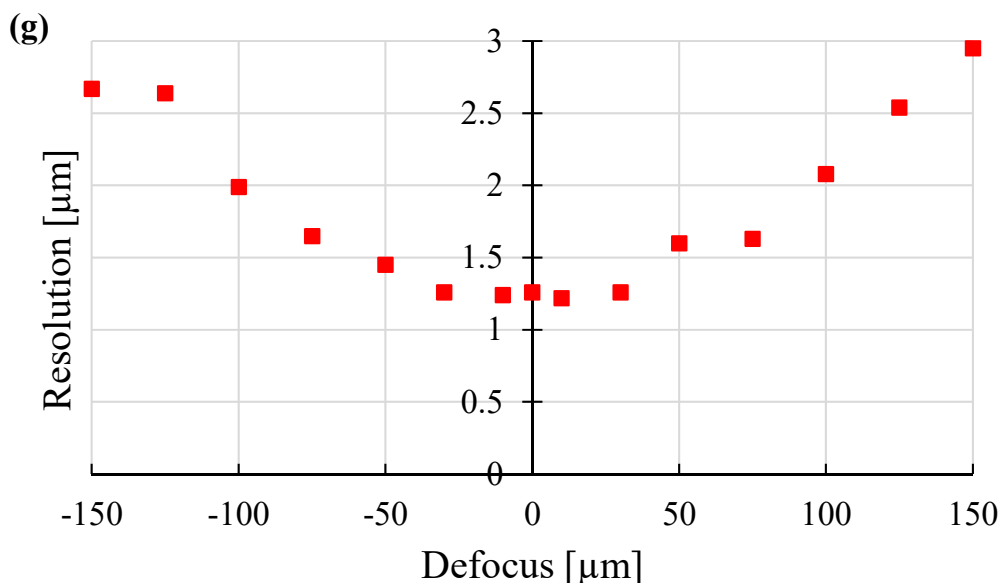


Figure 4.12 (*cont.*): (g) Image resolution of digitally refocused FPM phase image by sample defocus distance.

We imaged fixed HeLa cell line for the test of FPM phase imaging of 96Eyes. As shown in Figure 4.10, spatially varying aberrations are corrected in the FPM reconstructed phase images across full FOV, making sharp cell boundaries, which is necessary for the analysis of cell topology and cell count.

4.3.2 Digital image refocusing of 96Eyes

Digital image refocusing and increasing DOF of imaging system using FP is one of the most critical functionalities in a parallel imaging system like 96Eyes. The bottom layer of commercial 96 well plates is not perfectly flat and has a curvature of about 200 μm . This type of curvature can be corrected by fine tuning each objective positions according to the curvature; however, the manufacturing tolerance of the bottom layers is hard to fix without having mechanically moving focusing parts. In 96Eyes, we digitally refocus the defocused samples and calibrate non-uniform bottom height using computational method. For reference, the bottom layer curvature and standard deviation of the well bottom heights for polystyrene bottomed 96 well plates (Greiner Cell Star) and cyclic olefin copolymer (COC)

bottomed 96 well plates (Greiner UV Star) are shown in Figure 4.11 [62]. 19 polystyrene well plates and 16 COC well plates are measured using IR laser interferometric tomography, and the average and standard deviation of well bottom heights are graphed by well location. As we can see from Figure 4.11 (a1) and (b1), the bottom height distribution is not random, but has a bowl shape curvature. The maximum standard deviations of polystyrene well plates and COC well plates are $46\ \mu\text{m}$ and $17\ \mu\text{m}$. Therefore we need at least $\pm 50\ \mu\text{m}$ of FPM digital refocusing in order to calibrate the bottom height tolerance using computational method without any mechanical moving parts.

In order to check the digital refocusing status of 96Eyes, we defocused the Siemens star phase sample by known distances and digitally refocused the measured images using FPM reconstruction algorithm as shown in Figure 4.12. The FPM algorithm successfully digitally refocused the defocused images without losing the resolution of imaging system within the range of $\pm 30\ \mu\text{m}$ of defocus. When the sample defocuses $\pm 50\ \mu\text{m}$, the resolution becomes about $1.6\ \mu\text{m}$. Even in the $\pm 100\ \mu\text{m}$ defocused sample, the phase information from the sample

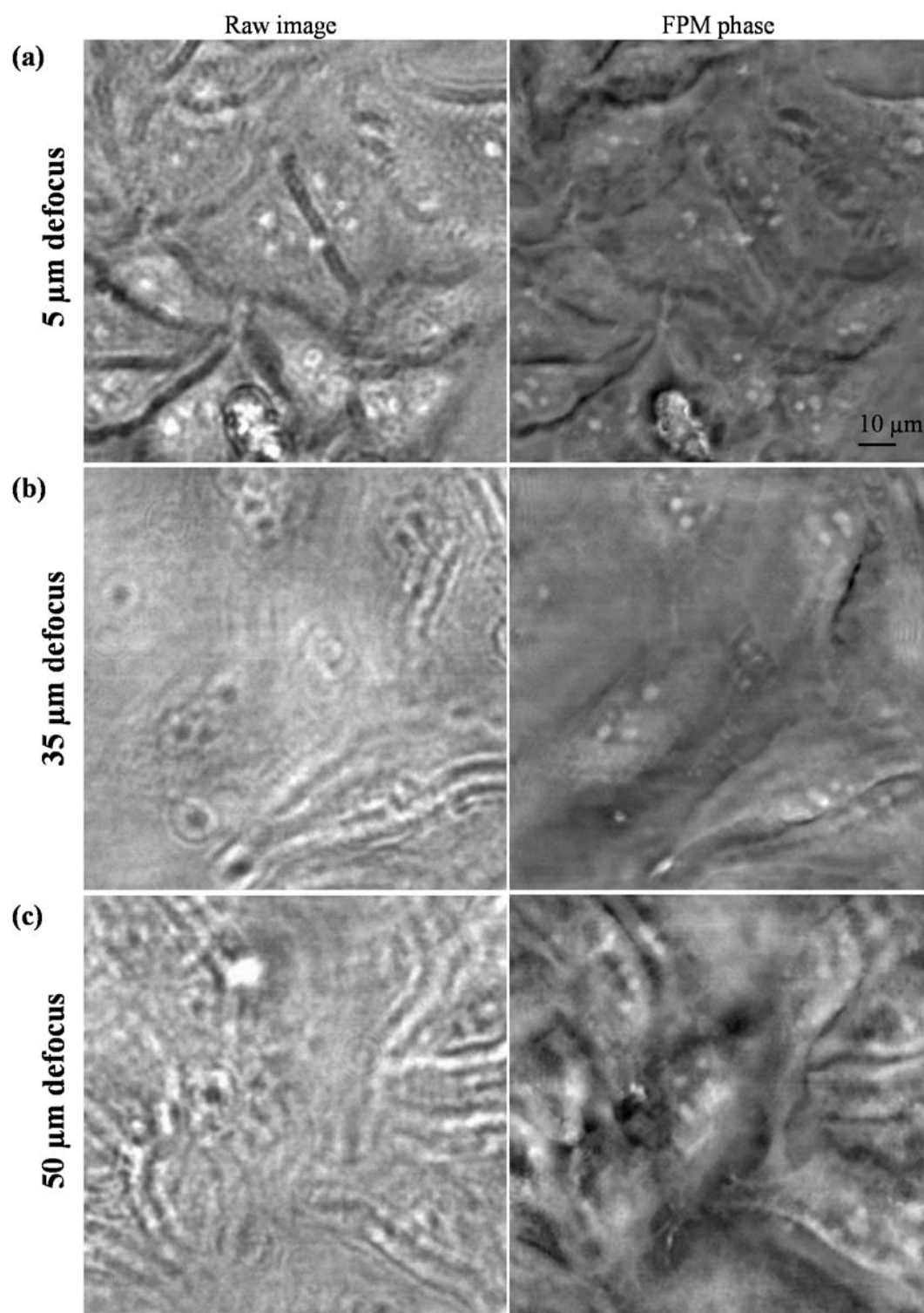


Figure 4.13: Digital refocusing of HeLa sample in 96 well plate. (a-c) Raw images and digitally refocused FPM phase image from differently defocused wells in a 96 well plate.

is retrieved and an image of about 2 μm resolution is reconstructed which is the comparable

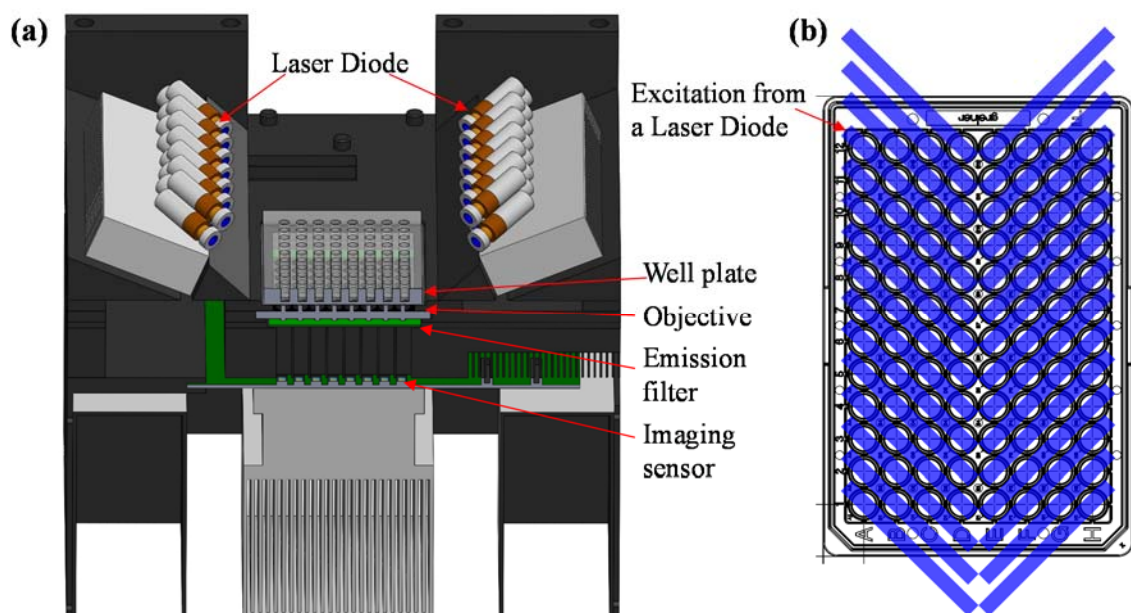


Figure 4.14: 96Eyes fluorescence imaging. (a) Cross-section view of 96Eyes which shows locations of laser diodes excitation light source, and an emission filter layer. (b) Each laser diode shines 4 diagonal wells simultaneously, and 30 laser diodes illuminate whole 96 well plate at the same time.

to the native resolution of raw images. The digitally refocused FPM phase image resolution by different sample defocus distance is plotted in Figure 4.12 (g).

We loaded a new 96 well plate of fixed HeLa cell lines into 96Eyes and imaged the whole well plate in order to test digital refocusing in the well plate imaging environment. The results are shown in Figure 4.13. Every well is in the different defocus condition ranging within $\pm 50 \mu\text{m}$, and FPM digitally refocuses each well into its best focused image plane. The raw images are blurry due to the defocus aberration; however, the FPM reconstructed images have sharp boundaries and small sub cellular elements such as nucleoli are resolved in the reconstructed phase images.

4.3.3 Fluorescence imaging of 96Eyes

As a multi-modal imaging system, 96Eyes can image fluorescence mode along with bright field phase imaging. In Figure 4.14, the parts for fluorescence imaging and well plate

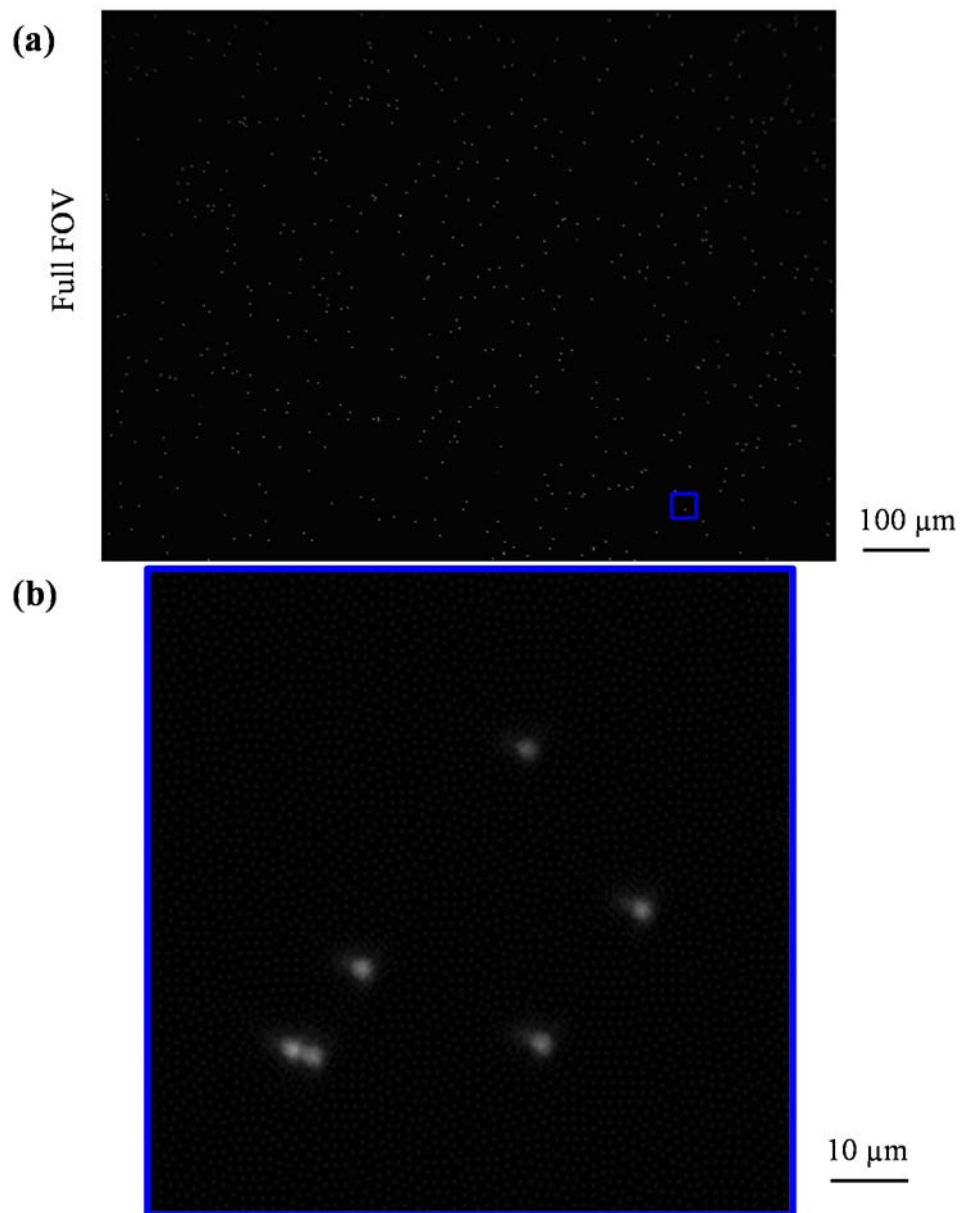


Figure 4.15: 96Eyes fluorescence imaging test using 2 μm fluorescence beads. (a) Full FOV fluorescence image. (b) Enlarged image from the location which is indicated in (a).

excitation method are shown. 15 laser diodes (center wavelength: 465 nm, bandwidth: 3 nm) are positioned at both sides of a well plate (total 30 laser diodes) and illuminate the whole area of well plate as shown in Figure 4.14 (b). Each laser diode has 3W optical power and a

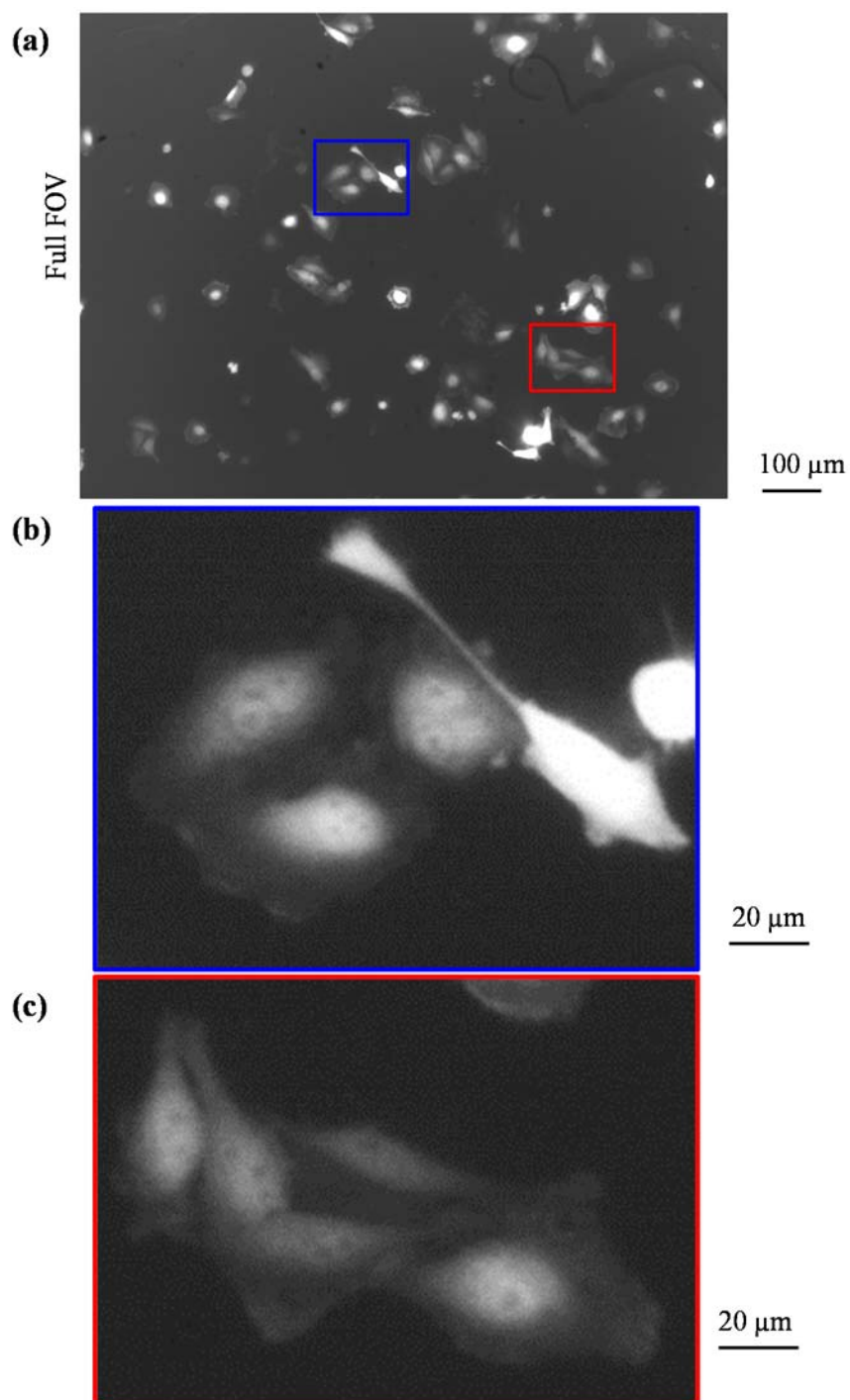


Figure 4.16: 96Eyes fluorescence imaging test using GFP HeLa cell lines. (a) Full FOV fluorescence image. (b and c) Enlarged images from the locations which are indicated in (a).

linear ray type which covers 4 diagonal wells at a time. A plate of emission filter (80 mm ×

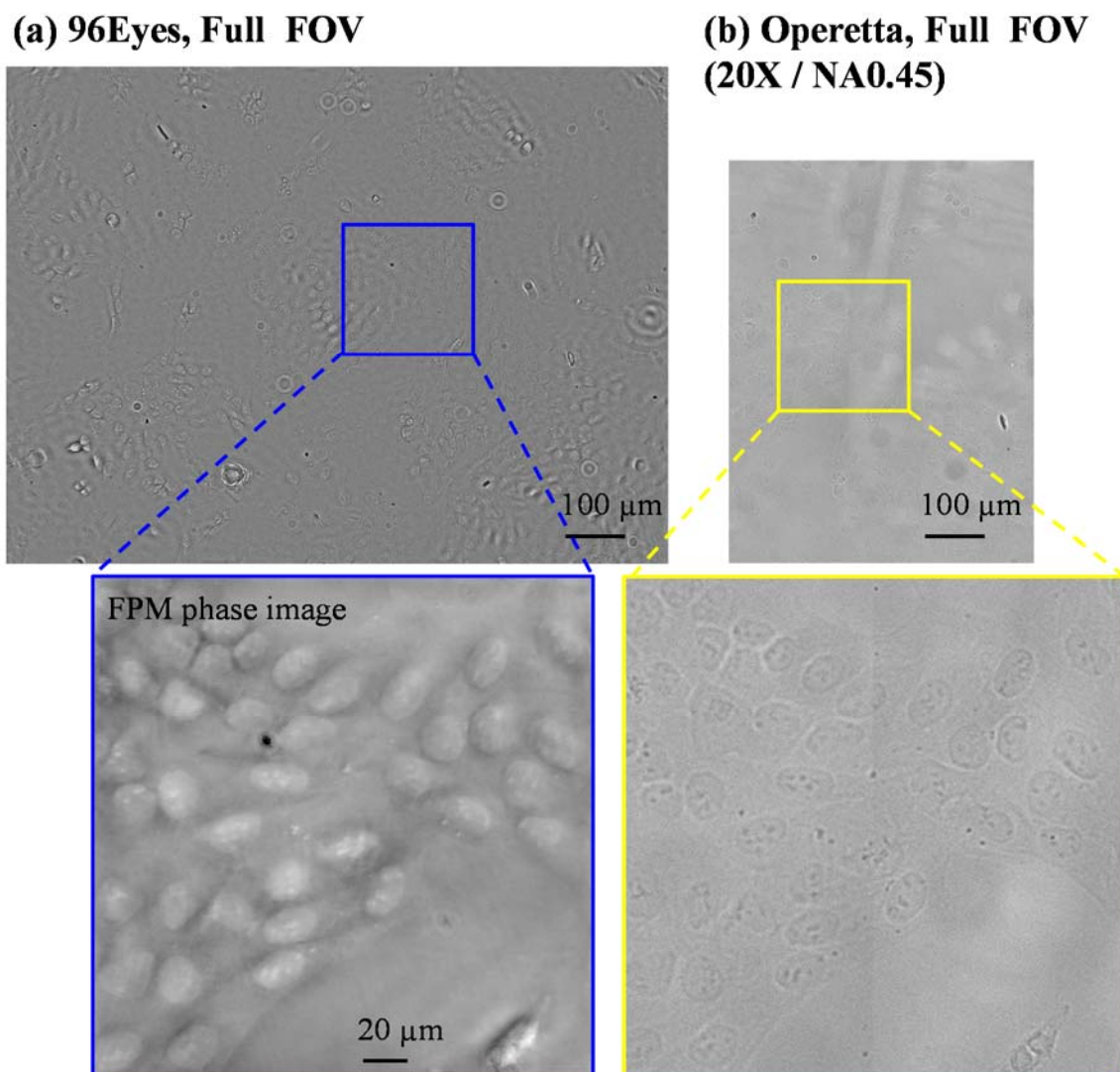


Figure 4.17: Bright field image comparison between 96Eyes and Operetta. (a) 96Eyes full FOV image and an enlarged FPM phase image. (b) Operetta full FOV image and the enlarged images from the same locations as in (a).

120 mm) of center wavelength 535 nm and pass bandwidth of 50 nm is inserted between the objective lens layer and the CMOS sensor layer in order to capture fluorescence images from FITC, GFP, or Alexa 488.

We tested fluorescence characteristics of 96Eyes by imaging 2 μm Green fluorescence beads and GFP HeLa cell lines. The results are shown in Figure 4.15 and Figure 4.16. The

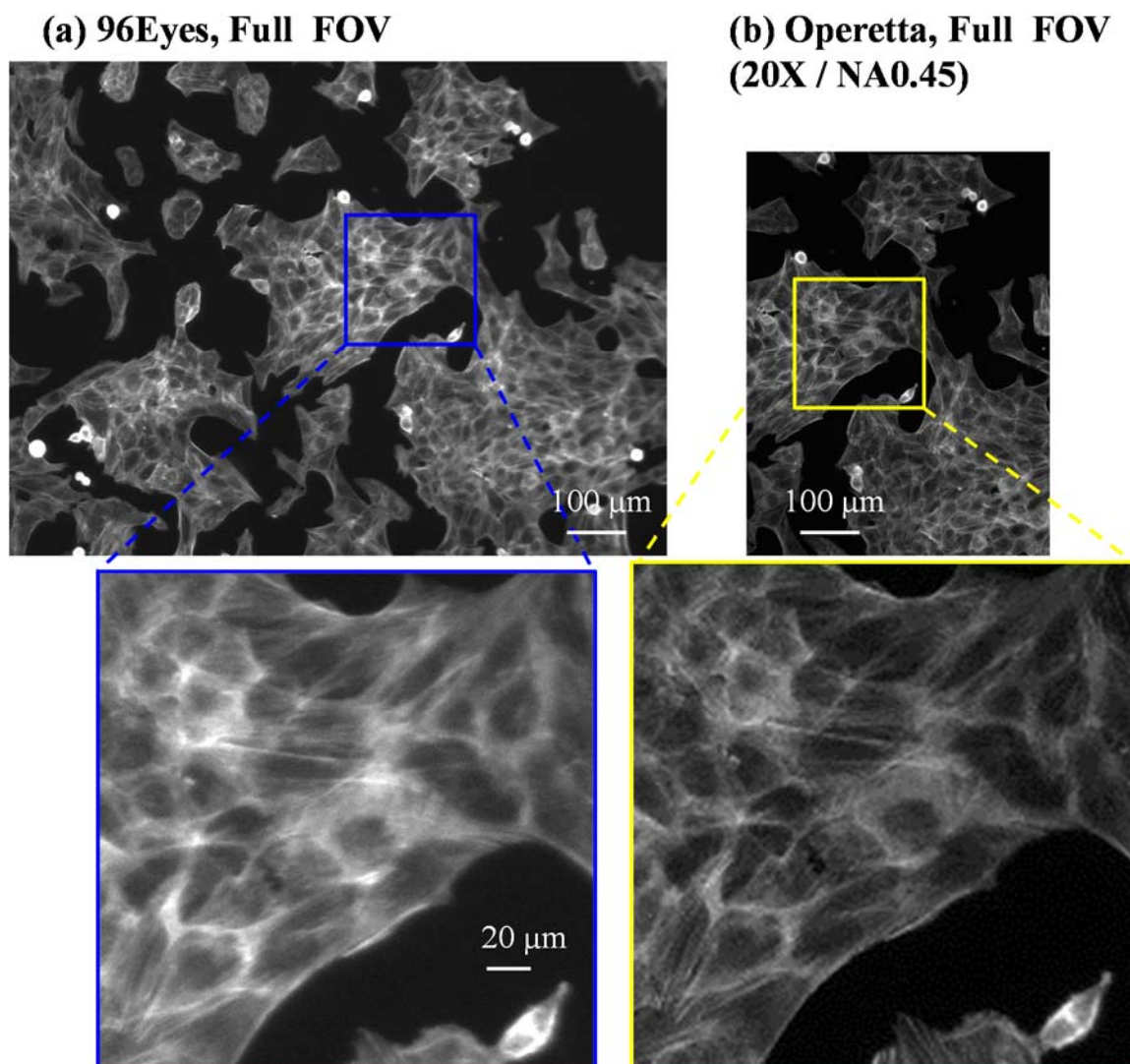


Figure 4.18: Fluorescence image comparison between 96Eyes and Operetta. (a) 96Eyes full FOV image and an enlarged image. (b) Operetta full FOV image and the enlarged images from the same locations as in (a).

beam size of excitation light source is large enough to illuminate the full FOV of sample area and resolution of the fluorescence images is good enough to resolve two closely positioned 2 μm Green fluorescence beads. The light source is also strong enough to generate detectable GFP signal from biological sample with 30 ms of exposure time, which we used for imaging GFP HeLa in Figure 4.16.

4.3.4 Comparison between 96Eyes and commercial well plate imaging systems

For the comparison of imaging result between 96Eyes and other commercial 96 well plate imaging systems, we used a fixed U2OS cell line which is labeled with Alexa 488. Full FOV bright field images from 96Eyes and Operetta imaging system are shown in Figure 4.17. In order to compare the FOV and resolution of images from different imaging systems, we used a 20X / NA0.45 objective lens in Operetta which has comparable effective NA of 96Eyes. As we can see from the full FOV images, the FOV of 96Eyes is about 2.5 times larger than the FOV of Operetta, which gives 2.5 enhancement in SBP. The enlarged images from the same sample location give the comparable imaging resolution from both imaging systems. The full FOV fluorescence images from both systems are shown in Figure 4.18. In the fluorescence imaging mode, 96Eyes has 2 μm of native resolution of the objective lens, so resolution is slightly worse than the fluorescence imaging resolution captured from 20X / NA0.45 objective imaging system.

Comparison between 96Eyes and other commercial well plate imaging systems (IncuCyte [28] and Cytation5 [63]) are listed in Table 4.2 and Table 4.3 for fluorescence imaging and phase imaging, respectively. In this comparison, we matched the resolution of different imaging systems by choosing the objective lenses which have similar NA as the effective NA of 96Eyes in each mode. Based on the FOV, resolution, and capture time from different imaging systems, 96Eyes's imaging throughput is about 200 times higher in fluorescence imaging mode and about 15 times higher in phase imaging mode.

4.4 Discussion and conclusion

We have demonstrated the operation of a fully parallel 96 well plate imaging system (96Eyes) in this chapter. The cost effective CMOS imaging sensors are assembled into a custom built PCB board and the images from the 96 imaging sensors are saved into a storage drive within 1 second. Small sized polymer objective lenses are fabricated using the injection molding method and make 2 μm resolution images across $\text{\O}1.6 \text{ mm}$ FOV. Along with these two imaging parts, a computational imaging technique, Fourier ptychography, is used in 96Eyes in order to correct aberrations related to the polymer objective lens and calibrate the uneven well bottom height using digital refocusing. The 96Eyes imaging system has a FOV

of $1.1 \text{ mm} \times 0.85 \text{ mm}$, and phase and fluorescence imaging resolution of $1.2 \text{ }\mu\text{m}$ and $2.0 \text{ }\mu\text{m}$, respectively. By parallelizing the image acquisition process for 96 wells, 96Eyes has improved the throughput of fluorescence imaging and phase imaging by 200 times and 15 times, respectively, compared to commercial 96 well plate imaging system.

There are several applications which require fluorescence imaging as main imaging modality rather than phase imaging. For those applications, current 96Eyes can accommodate a plate height tuning system into the well plate loading part. Using precise moving stages, such as Piezo electric stages, we can capture the sample plate from a few different heights and choose most focused image among them. Because the current throughput of fluorescence imaging mode is 200 times faster than other commercial imaging systems, capturing samples from a few different heights can still be faster than capturing one well at a time and scanning the whole plate.

The imaging throughput of current 96Eyes is limited by the speed of USB 3.0 protocol. In order to further increase the throughput of the system, the USB 3.0 data interface needs to be replaced with other faster data protocols, such as USB 3.1, or DisplayPort. Maintaining current USB 3.0 interface, simply increasing number of USB cables from a control board can also increase the speed of data transfer. There have been other approaches to use multiple objective lenses and multiple imaging sensors in FPM data acquisition process [64]. In this method, the different objective lens and imaging sensor capture different scattering components from the same sample, reducing total measurement time. Because 96Eyes also has also multiple objectives and imaging sensors, 96Eyes may utilize this method to improve the imaging throughput further.

Table 4.2: Fluorescence imaging throughput comparison.

	96Eyes	IncuCyte	Cytation 5
Resolution	2.0 μm	2.44 μm (10X)	3.0 μm (4X)
FOV (1 image)	1.1 mm x 0.85 mm (0.94 mm ²)	1.7 mm x 1.26 mm (2.14 mm ²)	1.63 mm x 1.53 mm (2.48 mm ²)
Capture time (1 image, 96 wells)	1 sec	8 min	9 min
Throughput (area per time)	55.6 mm ² /min	0.27 mm ² /min	0.28 mm ² /min
Fluorophore	GFP	Green/Red	>15 colors
Size ($H \times W \times D$)	25 cm x 29 cm x 30 cm	32 cm x 45 cm x 47 cm	45 cm x 51 cm x 42 cm

Table 4.3: Phase imaging throughput comparison.

	96Eyes	IncuCyte	Cytation 5
Resolution	1.2 μm	1.22 μm (20X)	1.2 μm (10X)
FOV (1 image)	1.1 mm x 0.85 mm (0.94 mm ²)	0.85 mm x 0.63 mm (0.54 mm ²)	0.65 mm x 0.61 mm (0.40 mm ²)
Capture time (1 image, 96 wells)	1 min	8 min	9 min
Throughput (area per time)	0.94 mm ² /min	0.07 mm ² /min	0.04 mm ² /min

BIBLIOGRAPHY

1. Bahaa E. A. Saleh & Teich MC (1991) *Fundamentals of Photonics* (John Wiley & Sons, Inc.).
2. Hecht E (2002) *Optics* (Addison Wesley, San Francisco) 4th Edition Ed.
3. Born M & Wolf E (1999) *Principles of optics: Electromagnetic theory of propagation, interference and diffraction of light* (Cambridge university press, Cambridge).
4. Mahajan VN (2013) *Optical imaging and aberrations. Part 3: Wavefront analysis* (SPIE press, Washington).
5. Mahajan VN (1998) *Optical imaging and aberrations. Part 1: Ray geometrical optics* (SPIE press, Washington).
6. Mahajan VN (2011) *Optical Imaging and aberrations. Part 2: Wave diffraction optics* (SPIE press, Washington).
7. Goodman JW (1996) *Introduction to Fourier optics* (McGraw-Hill, New York).
8. <http://spectra.arizona.edu/>
9. Zheng G, Horstmeyer R, & Yang C (2013) Wide-field, high-resolution Fourier ptychographic microscopy. *Nat Photonics* 7(9):739-745.
10. Hoppe W (1969) Beugung im inhomogenen primärstrahlwellenfeld. i. prinzipieller phasenmessung von elektronenbeugungsinterferenzen. *Acta Crystallographica Section A: Crystal Physics, Diffraction, Theoretical and General Crystallography* 25(4):495-501.
11. Born M (1926) Quantenmechanik der stossvorgänge. *Zeitschrift für Physik* 38(11-12):803-827.
12. Goodman J (2000) *Statistical Optics* (John Wiley & Sons).
13. Fienup JR (1982) Phase retrieval algorithms: a comparison. *Applied Optics* 21(15):2758-2769.
14. Fienup JR (1978) Reconstruction of an object from the modulus of its Fourier transform. *Optics Letters* 3(1):27-29.
15. Ou X, Horstmeyer R, Zheng G, & Yang C (2015) High numerical aperture Fourier ptychography: principle, implementation and characterization. *Opt Express* 23(3):3472-3491.
16. Zheng G, Ou X, Horstmeyer R, & Yang C (2013) Characterization of spatially varying aberrations for wide field-of-view microscopy. *Opt Express* 21(13):15131-15143.
17. Chung J, Kim J, Ou X, Horstmeyer R, & Yang C (2016) Wide field-of-view fluorescence image deconvolution with aberration-estimation from Fourier ptychography. *Biomed Opt Express* 7(2):352-368.
18. Ou X, Zheng G, & Yang C (2014) Embedded pupil function recovery for Fourier ptychographic microscopy. *Opt Express* 22(5):4960-4972.
19. Zuo C, Sun J, & Chen Q (2016) Adaptive step-size strategy for noise-robust Fourier ptychographic microscopy. *Opt Express* 24(18):20724-20744.
20. Angelini TE, *et al.* (2011) Glass-like dynamics of collective cell migration. *Proc Natl Acad Sci U S A* 108(12):4714-4719.
21. Dey-Guha I, *et al.* (2011) Asymmetric cancer cell division regulated by AKT. *Proc Natl Acad Sci U S A* 108(31):12845-12850.

22. Costa MR, *et al.* (2011) Continuous live imaging of adult neural stem cell division and lineage progression in vitro. *Development* 138(6):1057-1068.
23. Matsui T, *et al.* (2012) Neural stem cells directly differentiated from partially reprogrammed fibroblasts rapidly acquire gliogenic competency. *Stem Cells* 30(6):1109-1119.
24. Lin S, Fonteno S, Weng JH, & Talbot P (2010) Comparison of the toxicity of smoke from conventional and harm reduction cigarettes using human embryonic stem cells. *Toxicol Sci* 118(1):202-212.
25. Srinivasan R, *et al.* (2012) Pharmacological chaperoning of nicotinic acetylcholine receptors reduces the endoplasmic reticulum stress response. *Mol Pharmacol* 81(6):759-769.
26. http://www.zeiss.com/microscopy/en_us/products/microscope-components/incubation.html
27. <http://www.nikoninstruments.com/Products/Live-Cell-Screening-Systems/BioStation-CT>
28. <http://www.essenbioscience.com/essen-products/incucyte/>
29. Lohmann AW, Dorsch RG, Mendlovic D, Zalevsky Z, & Ferreira C (1996) Space-bandwidth product of optical signals and systems. *J. Opt. Soc. Am. A* 13(3):470-473.
30. Zheng G, Ou X, & Yang C (2013) 0.5 gigapixel microscopy using a flatbed scanner. *Biomed Opt Express* 5(1):1-8.
31. Zheng G, Lee SA, Antebi Y, Elowitz MB, & Yang C (2011) The ePetri dish, an on-chip cell imaging platform based on subpixel perspective sweeping microscopy (SPSM). *Proc Natl Acad Sci U S A* 108(41):16889-16894.
32. Jung JH, Han C, Lee SA, Kim J, & Yang C (2014) Microfluidic-integrated laser-controlled microactuators with on-chip microscopy imaging functionality. *Lab Chip* 14(19):3781-3789.
33. Han C, Pang S, Bower DV, Yiu P, & Yang C (2013) Wide field-of-view on-chip Talbot fluorescence microscopy for longitudinal cell culture monitoring from within the incubator. *Anal Chem* 85(4):2356-2360.
34. Bishara W, Su TW, Coskun AF, & Ozcan A (2010) Lensfree on-chip microscopy over a wide field-of-view using pixel super-resolution. *Optics Express* 18(11):11181-11191.
35. Bishara W, *et al.* (2011) Holographic pixel super-resolution in portable lensless on-chip microscopy using a fiber-optic array. *Lab Chip* 11(7):1276-1279.
36. Greenbaum A, Sikora U, & Ozcan A (2012) Field-portable wide-field microscopy of dense samples using multi-height pixel super-resolution based lensfree imaging. *Lab Chip* 12(7):1242-1245.
37. Coskun AF, Sencan I, Su TW, & Ozcan A (2011) Wide-field lensless fluorescent microscopy using a tapered fiber-optic faceplate on a chip. *Analyst* 136(17):3512-3518.
38. Coskun AF, Sencan I, Su TW, & Ozcan A (2010) Lensless wide-field fluorescent imaging on a chip using compressive decoding of sparse objects. *Opt Express* 18(10):10510-10523.
39. Ou X, Horstmeyer R, Yang C, & Zheng G (2013) Quantitative phase imaging via Fourier ptychographic microscopy. *Opt Lett* 38(22):4845-4848.
40. Horstmeyer R & Yang C (2014) A phase space model of Fourier ptychographic microscopy. *Opt Express* 22(1):338-358.

41. Chung J, Ou X, Kulkarni RP, & Yang C (2015) Counting White Blood Cells from a Blood Smear Using Fourier Ptychographic Microscopy. *PLoS One* 10(7):e0133489.
42. Williams A, *et al.* (2014) Fourier ptychographic microscopy for filtration-based circulating tumor cell enumeration and analysis. *Journal of Biomedical Optics* 19(6):066007.
43. Horstmeyer R, Ou X, Zheng G, Willems P, & Yang C (2015) Digital pathology with Fourier ptychography. *Computerized Medical Imaging and Graphics* 42:38-43.
44. Dong S, Guo K, Nanda P, Shiradkar R, & Zheng G (2014) FPscope: a field-portable high-resolution microscope using a cellphone lens. *Biomed Opt Express* 5(10):3305-3310.
45. Horstmeyer R, Heintzmann R, Popescu G, Waller L, & Yang C (2016) Standardizing the resolution claims for coherent microscopy. *Nature Photonics* 10(2):68-71.
46. Dong S, Nanda P, Shiradkar R, Guo K, & Zheng G (2014) High-resolution fluorescence imaging via pattern-illuminated Fourier ptychography. *Opt Express* 22(17):20856-20870.
47. Matsushima K & Shimobaba T (2009) Band-Limited Angular Spectrum Method for Numerical Simulation of Free-Space Propagation in Far and Near Fields. *Optics Express* 17(22):19662-19673.
48. Kreis TM, Adms M, & Jüptner WPO (1997) Methods of Digital Holography: A comparison. *SPIE Proc.* 3098:224-233.
49. Gong S, *et al.* (2003) A gene expression atlas of the central nervous system based on bacterial artificial chromosomes. *Nature* 425:917-925.
50. Henley BM, *et al.* (2013) Transcriptional regulation by nicotine in dopaminergic neurons. *Biochem Pharmacol* 86(8):1074-1083.
51. Srinivasan R, *et al.* (Smoking-relevant nicotine concentration attenuates the unfolded protein response in dopaminergic neurons. *The Journal of Neuroscience (In press)*.
52. Pruszek J, Just L, Isacson O, & Nikkhah G (2009) Isolation and Culture of Ventral Mesencephalic Precursor Cells and Dopaminergic Neurons from Rodent Brains. *Current Protocols in Stem Cell Biology*. Chapter 2(Unit 2D.5).
53. Tian L, *et al.* (2015) Computational illumination for high-speed in vitro Fourier ptychographic microscopy. *Optica* 2(10):904-911.
54. Tian L, Li X, Ramchandran K, & Waller L (2014) Multiplexed coded illumination for Fourier Ptychography with an LED array microscope. *Biomed Opt Express* 5(7):2376-2389.
55. Hirsch E, Graybiel AM, & Agid YA (1988) Melanized dopaminergic neurons are differentially susceptible to degeneration in Parkinson's disease. *Nature* 334:345-348.
56. German DC, Manaye K, Smith WK, Woodward DJ, & Saper CB (1989) Midbrain dopaminergic cell loss in parkinson's disease: Computer visualization. *Annals of Neurology* 26(4):507-514.
57. Goto S, Hirano A, & Matsumoto S (1989) Subdivisional involvement of nigrostriatal loop in idiopathic Parkinson's disease and striatonigral degeneration. *Annals of Neurology* 26(6):766-770.
58. Rinne JO, Rummukainen J, Paljärvi L, & Rinne UK (1989) Dementia in Parkinson's disease is related to neuronal loss in the medial substantia nigra. *Annals of Neurology* 26(1):47-50.
59. Xu H, *et al.* (2013) Predictability of Peripheral Lymphocyte Reduction of Novel S1P1 Agonists by In Vitro GPCR Signaling Profile. *Journal of Biomolecular Screening* 18(9):997-1007.

60. Oo ML, *et al.* (2007) Immunosuppressive and Anti-angiogenic Sphingosine 1-Phosphate Receptor-1 Agonists Induce Ubiquitylation and Proteasomal Degradation of the Receptor. *Journal of Biological Chemistry* 282(12):9082-9089.
61. Haguet V, *et al.* (2013) Time-lapse screening by parallelized lensfree imaging. in *International Conference on Miniaturized Systems for Chemistry and Life Sciences* (Freiburg, Germany).
62. https://www.gbo.com/en_US.html
63. <https://www.biotek.com/>
64. Konda P, Taylor J, & Harvey AR (2015) Multi-aperture Fourier Ptychography imaging in the near field. in *Imaging and Applied Optics* (Arlington, Virginia, USA).